

VIBRATIONAL RESPONSE OF ADSORBATES TO FEMTOSECOND METAL  
SUBSTRATE HEATING

Joseph P. Culver

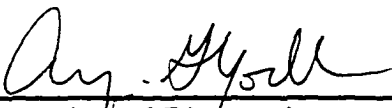
A DISSERTATION

in

PHYSICS AND ASTRONOMY

Presented to the Faculties of the University of Pennsylvania in Partial Fulfillment of  
the Requirements for the Degree of Doctor of Philosophy

1997

  
\_\_\_\_\_  
Supervisor of Dissertation

  
\_\_\_\_\_  
Graduate Group Chairperson

**UMI Number: 9727209**

---

**UMI Microform 9727209**  
**Copyright 1997, by UMI Company. All rights reserved.**

**This microform edition is protected against unauthorized  
copying under Title 17, United States Code.**

---

**UMI**  
**300 North Zeeb Road**  
**Ann Arbor, MI 48103**

COPYRIGHT

Joseph Parkin Culver

1997

## DEDICATION

To my family

## ACKNOWLEDGMENTS

There are many people in both the Physics and Chemistry Departments at the University of Pennsylvania to whom I am indebted with respect to completing this thesis. First I would like to acknowledge my advisors Professors Arjun Yodh and Robin M. Hochstrasser for their patience and guidance. Arjun's enthusiasm about scientific research is contagious and his encouragement and focus helped me greatly in these research endeavors. Arjun has an ability to distill complex experimental schemes, explanations and results in to simple concise views. I hope to have at least partially learned this skill. Robin's deep insights into physical chemistry and ultrafast phenomena along with his dry sense of humor strongly shape the ways and means of his research group. I am very grateful to have spent my graduate studies in such a rich, stimulating environment. His wisdom about various aspects of scientific life provided a valuable and much appreciated learning experience.

The research in our labs always involved the combined efforts between several Post Doctoral researchers and Graduate Students. I would first like to thank Jeff Owrutsky, who as a Post-Doc, taught me the fundamentals and showed me the spirit of experimental research. In the same vein I would like to thank Mohsen Yeganeh for introducing me to the idiosyncrasies of UHV chambers and nonlinear optics, and reintroducing me to the sonic joys of Van Halen.

I am very grateful to have worked with Min Li. Min and I were the graduate

students who together carried out the majority of work on these experiments. Min's diligence and patience towards research were critical to the success of these experiments. Together we sorted out many technical difficulties. I am glad to have shared the many days of laser tuning, data collection and analysis with her.

I greatly appreciated working with the members of Arjuns graduate group. They were often valuable sources of ideas, solutions, companionship and the odd oscilloscope. I would like to thank Jining Qi, Ming Kao, David Boas, Maureen Oleary, Peter Kaplan, Tony Dinsmore, William Angerer and every one else in the group. I would particularly like thank Ritu Verma for inheriting the ultrafast surface lab.

I would also like to acknowledge the many Post Docs and students in Robin's group. They are too numerous to name them all individually however I would like to specifically thank the RLBL lunch attendees for their camaraderie both scientifically and personally. In particular I would like to thank Charles M. Philips, Nick Pugliano and Sandrasegaram Gnanakaran for their friendship while I completed my thesis work.

Finally, I would like to thank my family for providing the context in which these scientific studies have their meaning. In particular, the person to whom I am most indebted is my wife Mary. Her understanding and support have been essential throughout these years of graduates studies.

## ABSTRACT

### VIBRATIONAL RESPONSE OF ADSORBATES TO FEMTOSECOND METAL SUBSTRATE HEATING

Joseph P. Culver

Arjun G. Yodh

This thesis discusses the use of IR spectroscopy to probe the vibrations of adsorbate molecules following impulsive excitation of electrons in underlying metal substrates by femtosecond visible light pulses. In these experiments the dominant spectral changes observed result from temperature dependent shifts of the oscillator complex frequency. Using the Liouville equation, a general description of the optical response is developed and discussed in the context of an impulsive change in frequency. As low frequency adsorbate-like modes become excited via coupling to substrate electrons and phonons, the high frequency modes are observed to experience frequency shifts. These couplings are described in terms of a Brownian oscillator model. Time-resolved measurements of the stretch mode absorption for CO on copper indicate that couplings of a low frequency vibration to both substrate reservoirs are significant. The coupling rates were determined separately as a result of the dramatic differences in the electronic and phonon temperature profiles.

The effects of excitation pulse fluence on vibrational energy transfer between the CO low frequency frustrated translation and metal substrate electrons are examined.

A temperature dependent coupling rate is extracted from our data using a dynamical charge transfer model.

## Contents

<b>1</b>	<b>Introduction</b>	<b>1</b>
<b>2</b>	<b>Dynamics of the Metal Adsorbate Chemisorbtive Bond</b>	<b>7</b>
2.1	Models of metal surface chemisorption. . . . .	8
2.2	Adsorbate Vibrations Coupling to Metal Substrate Electron-Hole Pairs	13
2.3	Time Dependent Dephasing of Adsorbate Vibrations . . . . .	22
2.4	General Theory of a Quantum Harmonic Oscillator Coupled to Two Temperature Reservoirs. . . . .	33
<b>3</b>	<b>Substrate Response To Ultrashort Visible Excitation</b>	<b>38</b>
<b>4</b>	<b>Femtosecond Infrared Spectroscopy</b>	<b>44</b>
4.1	Modulation of the complex frequency in a two level system . . . . .	45
4.2	Model of an Impulsive Complex Frequency Shift . . . . .	51
4.2.1	Desorption . . . . .	61
<b>5</b>	<b>Experimental Description</b>	<b>63</b>

5.1	Basic plan of experiments . . . . .	63
5.2	Vacuum system . . . . .	64
5.3	Laser system . . . . .	69
<b>6</b>	<b>Results and Discussion</b>	<b>75</b>
6.1	CW IR Spectra . . . . .	75
6.2	Transient IR measurements . . . . .	79
6.3	Fluence Dependence . . . . .	89
6.4	Desorption Threshold . . . . .	92
6.5	Fitting Results . . . . .	94
6.6	Discussion . . . . .	98
<b>7</b>	<b>Free Induction Decay</b>	<b>100</b>
7.1	Experimental . . . . .	101
7.2	Theory . . . . .	105
7.2.1	Frequency Domain . . . . .	108
7.2.2	Time Domain . . . . .	108
7.3	Results . . . . .	109
7.3.1	Frequency domain . . . . .	109
7.3.2	Time Domain . . . . .	112
7.4	Conclusion . . . . .	113

<b>8 Conclusion</b>	<b>116</b>
<b>9 Appendices</b>	<b>118</b>
9.1 IR Reflection Absorption Spectroscopy . . . . .	118
9.1.1 CW Basics . . . . .	118
9.1.2 Static and Time Variant Substrate Reflectivity . . . . .	121
9.2 Integrating inhomogenous first order differentials equations . . . . .	125
9.3 Substrate temperatures: c program . . . . .	128
9.4 Fitting routine: c program . . . . .	134
<b>10 Bibliography</b>	<b>148</b>

## List of Figures

2.1	Chemisorption of CO on Cu(111) . . . . .	9
2.2	Dynamical charge transfer . . . . .	15
2.3	Temperature dependence of $\gamma_e$ . . . . .	21
2.4	Schematic of a stochastic Brownian oscillator . . . . .	25
2.5	Anharmonic coupling between two vibrational modes . . . . .	27
2.6	Energy flow between levels of a harmonic oscillator. . . . .	34
3.1	Representative electron and phonon temperatures . . . . .	42
4.1	Schematic of two time-resolved IR probe methods. . . . .	47
4.2	Time ordering of the integrals for the impulsive perturbation model . . . . .	53
4.3	A comparison of the gated CW and short pulse probe methods . . . . .	56
4.4	Simulation of impulsive linebroadening . . . . .	58
4.5	Simulation of a small impulsive frequency shift . . . . .	59
4.6	Simulation of a large impulsive frequency shift . . . . .	60
5.1	FTIR setup . . . . .	67

5.2	CO on Cu LEED pattern . . . . .	70
5.3	Schematic of the laser apparatus with quasi-CW IR probe . . . . .	71
6.1	Temperature dependence of the CO stretch absorption . . . . .	76
6.2	Difference spectra of the CO stretch . . . . .	80
6.3	Transient fractional difference reflectivity of CO on Cu(111). . . . .	82
6.4	Transient fractional difference reflectivity of bare Cu(111) . . . . .	84
6.5	Schematic of the fitting procedure . . . . .	87
6.6	Transient temperatures of the CO on Cu(111) system . . . . .	88
6.7	Transient CO response at four frequencies . . . . .	90
6.8	Transient CO response at five different fluences . . . . .	91
6.9	CO coverage dependence of the SHG signal from Cu(111) . . . . .	93
6.10	Time evolution of $\gamma_e$ . . . . .	97
7.1	Schematic of the FID apparatus . . . . .	102
7.2	Free induction decay of CO on Cu(111) . . . . .	104
7.3	SFG spectra of CO on Cu(111) . . . . .	105
9.1	3 layer reflection model . . . . .	119
9.2	Modulus and argument of G . . . . .	122

## List of Tables

2.1	Vibrational Modes of CO on the 100 and 111 faces of Cu . . . . .	11
6.1	Summary of Results . . . . .	92
7.1	Second order susceptibility of CO on Cu(111) . . . . .	110

## Chapter 1

### Introduction

With the complexity of the bonds and geometry that occur at the adsorbate-substrate interface there is great interest in the bond specificity inherent in infrared vibrational studies [1, 2]. Frequency domain measurements of resonance shifts, linewidth changes, and absorption strengths provide information about the nature of adsorbate vibrational modes including; local electronic structure (binding sites, surface contamination, coadsorption), reactions (diffusion, desorption), intermode coupling and energy exchange. However the dephasing and energy relaxation rates, which are central to vibrational dynamics must be inferred and can be model dependent.

Recent developments in the generation of femtosecond visible and IR pulses are now facilitating the application of transient spectroscopy techniques to adsorbate studies[2, 3, 4]. Transient spectroscopy enables more direct insight into these processes, and provides a variety of possible measurement schemes of ground and excited state dynamics. The goal of the experiments that constitute this thesis, is to eluci-

date metal adsorbate vibrational dynamics and explore energy transfer processes of the adsorbate-substrate system, providing a basis upon which more complex surface chemistry processes can be understood.

In this thesis I discuss IR pulsed surface probes and excitation of metal adsorbate complex with ultrafast visible pulses. Femtosecond optical excitation of surfaces creates a unique environment for molecular adsorbates that can initiate surface chemistry[5]. Recent experiments along these lines have shown, for example, that nonequilibrium substrate conditions can play a central role in laser induced desorption [6, 7, 8, 9, 10, 11, 12]. The use of ultrafast vibrational spectroscopy to resolve the specific states of molecules is particularly attractive for detailed descriptions of molecular environments before and after a femtosecond photo-induced reaction.

State-resolved measurements of adsorbate vibrational energy relaxation [13, 14, 15, 16, 17] and final state analysis of femtosecond desorption products [7, 8, 10, 11] are two classes of experiments that are used to elucidate the nature of energy transfer in adsorbate systems. Most measurements that have focused on vibrational energy relaxation of molecules on surfaces have relied on the use of resonant IR pump pulses to create nonequilibrium populations in specific adsorbate bonds [16, 17, 18, 19, 20]. In these experiments energy flows from the excited adsorbate to the unperturbed substrate reservoirs. An alternate approach to measuring adsorbate-substrate couplings, is to deposit energy into the substrate and monitor energy flow

into and out of the adsorbate [8, 21, 14, 22]. Our measurements employ the latter method to study adsorbate vibrational dynamics. In particular we have studied the vibrational response of CO on Cu(111) following a femtosecond visible excitation pulse.

### **Adsorbate Substrate Energy Transfer**

Generally adsorbate vibrations couple to both the electronic and phonon degrees of freedom of a metal substrate. Theoretical and experimental studies have provided convincing evidence that a dynamical charge transfer mechanism is responsible for the coupling of adsorbate vibrations to substrate electron-hole pairs, [17, 23, 24]. On the other hand anharmonic couplings to phonons account for energy transfer between adsorbate and substrate vibrations[25, 26, 27]. Chapters 2-4 will discuss theory and measurement methodologies relevant to studies of energy transfer within the metal substrate/adsorbate complex.

Direct measurements of low frequency ( $10\text{-}500\text{ cm}^{-1}$ ) adsorbate vibrational dynamics are difficult primarily because there exist few ultrafast laser probes in the relevant spectral region. The couplings and dynamics of these adsorbate modes are however of great interest, particularly because these modes are highly excited prior to desorption, diffusion and other surface reactions. Current femtosecond infrared probes using nonlinear crystals for infrared generation are capable of frequencies as

low as  $1000\text{ cm}^{-1}$ [28]. However in the field of surface vibrational dynamics only the modes with  $\nu > 1800\text{cm}^{-1}$  have been measured. However the populations of low frequency modes can be monitored *indirectly* via the effects they induce on the higher frequency modes. In the cases presented in this thesis, the excitation of a low frequency modes modifies the vibrational dynamics of a higher frequency mode which in turn is accessible to current ultrafast IR probes. Section 2.3 discusses time-dependent dephasing of high frequency modes due to anharmonic coupling to lower frequency modes. Our goal is to measure the coupling rates between low frequency adsorbate vibrations and the substrate electron and phonon reservoirs.

Chapter 3 describes the metal substrate response to the ultrafast visible heating pulse. A two-temperature model [29] will be reviewed and discussed in context of measurements of adsorbate/substrate energy transfer. The model enables us to compute the bulk electron temperature and the bulk phonon temperature following the absorption of energy from the visible pulse. The resulting temperature reservoirs will subsequently be coupled to the adsorbate, using the theory developed in Chapter 2.

Chapter 4 reviews the basics of IR spectroscopy on metal surfaces, and then develops a description for the frequency-dependent temporal response of an adsorbate, that accounts for variations in adsorbate complex frequency and population. The formalism enables us to predict the response of the adsorbate to various excitations and to compare experimental methods.

## Measurements of Adsorbate Vibrational Dynamics

In order to link the coupling rates obtained from low temperature measurements to highly excited non-equilibrium processes such as desorption, the basic temperature dependencies of the energy transfer process must be understood. To this end we conducted time resolved infrared (IR) spectroscopic studies of  $(\sqrt{3} \times \sqrt{3})R30^\circ$  CO molecularly adsorbed on Cu(111) just following visible excitation pulses of differing fluences. Observations of the CO vibrational response were obtained *in situ* on a state specific basis, employing laser pulse excitations near the femtosecond desorption threshold. The transient vibrational dynamics of the low frequency frustrated lateral translation modes were measured.

Experimental details are described in Chapter 5 and the results and implications of our measurements are discussed in Chapter 6. In particular we find that at low levels of visible-pulse excitation the spectral variation of the CO stretch vibration is produced via the heating of the frustrated translational mode of the adsorbate. The molecular temperature is determined and, interestingly, is found to be greater than the bulk electron and phonon temperatures over certain timescales. The theory developed in Chapters 2-4 are used interpret these observations. The model explicitly introduces the temperature-dependent coupling rate derived from the dynamical charge transfer model for electron-hole pair coupling to adsorbate vibrations and is then used to measure these rates for the first time.

Measurements of vibrational energy and coherence relaxation are essential for a comprehensive description of surface adsorbate systems. A thorough characterization of the vibrational dynamics requires measurement of both population and coherence relaxation rates. In Chapter 7 I present the first measurement of a vibrational coherent transient for an adsorbate on a metal surface. We determined the vibrational dephasing rate ( $T_2$ ) for CO on Cu(111) by obtaining the free induction decay signal. A short IR pulse (380 fs) was used to generate a vibrational coherence and its temporal evolution is measured by upconverting the decaying surface polarization with a delayed pulse.

In addition to the FID measurement, we measured the frequency domain surface sum frequency generation (SFG) spectrum for CO on Cu(111). The spectra, especially at low coverage, display an interference which was analyzed to determine the relative amplitude and phase of the resonant and nonresonant parts of the second-order susceptibility. The total dephasing time and linewidth obtained in the time and frequency domains, respectively, are self-consistent. The values also agree with the surface Fourier-transform infrared (FTIR) studies discussed in Chapter 6.

## Chapter 2

### Dynamics of the Metal Adsorbate Chemisorbtive Bond

Adsorbate vibrations couple to both the electronic and phonon degrees of freedom of a metal substrate. Theoretical and experimental studies provide convincing evidence that a dynamical charge transfer mechanism is responsible for the coupling of adsorbate vibrations with substrate electron-hole pairs, [17, 23, 24]. On the other hand anharmonic couplings to phonons also account for energy transfer between adsorbate and substrate vibrations[25, 26, 27]. In this Chapter we will discuss the theory and measurement methodologies relevant to studies of energy transfer within the metal substrate/adsorbate complex. In particular, intermode anharmonic couplings will be considered as a means of assessing the dynamics of low frequency adsorbate modes.

When an adsorbate is brought in contact with a metal surface, a bond develops through a combination of electron-electron repulsion, polarization of the substrate and partial charge transfer between the substrate and adsorbate[30]. As the adsorbate vibrates these interactions are modulated and the substrate electrons involved in the

bond relax to minimize the system energy. Specifically for CO on metals the partial charges in the  $5\sigma$  and  $2\pi^*$  orbitals are affected by vibrationally induced electronic transitions. The partial charges in the adsorbate orbitals are not constant but are instead modulated by the CO vibrational dynamics; this basic phenomena is called dynamical charge transfer. The dynamical charge transfer process is the main source of energy transfer between adsorbate vibrations and substrate electron-hole pairs. To make the discussion of the energy transfer theory more transparent I will first review the pertinent details of the electronic and vibrational structure of CO chemisorbed on Cu(111).

## **2.1 Models of metal surface chemisorption.**

The main challenge of chemisorption theory is to combine solid state theories, in a suitable way to include the substrate band structure, and molecular orbital theories appropriate to adsorbate electrons. The most developed theories of CO chemisorption on metals are cluster models based on the Blyholder model. The Blyholder model obtains the electronic structure of the adsorbate/substrate complex from a linear combination of the CO molecular orbitals and the Cu d and sp electrons[30, 31]. Alternately the system can be approached from a solid state physics view point by using delocalized extended wave functions for the substrate and treating the adsorbate as a defect[32]. A comparison of these two approaches can be found in several reviews [32].

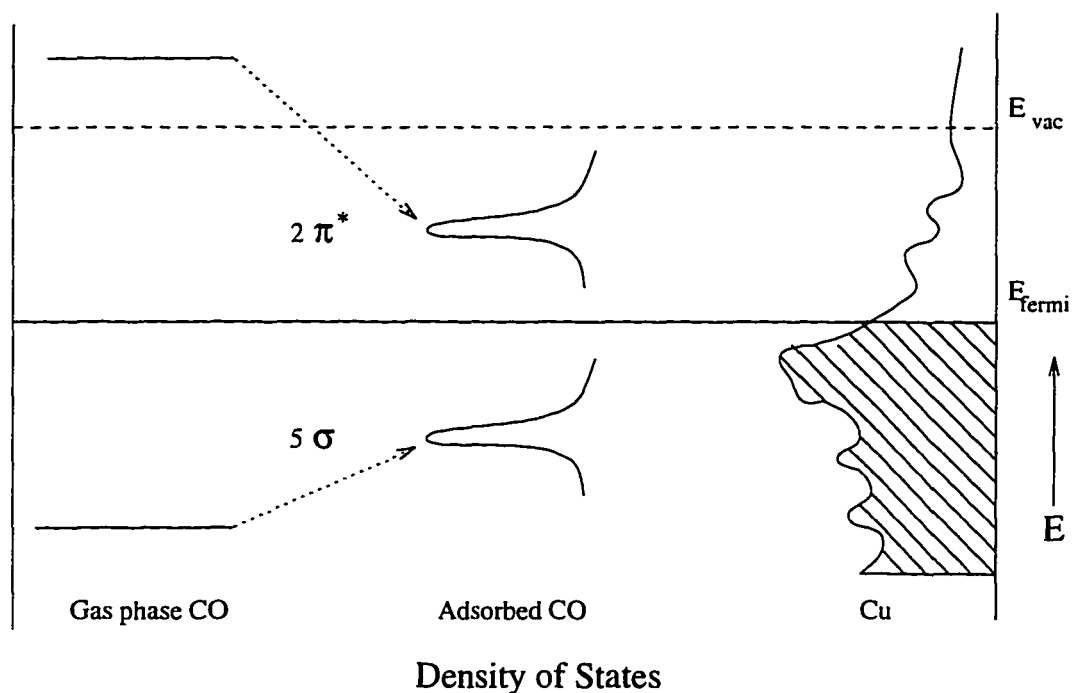


Figure 2.1: The chemisorption of CO on Cu(111). The  $5\sigma$  and  $2\pi^*$  CO orbitals mix with the Cu valence band electrons as described in the text.

Recently density functional calculations have been used to treat both the substrate and adsorbate with extended wave functions and with promising initial results [27].

The CO orbitals involved with the bond are the lowest unoccupied molecular orbital (LUMO),  $2\pi^*$ , and the highest occupied molecular orbital (HUMO),  $5\sigma$ . Gas phase CO has orbital energies of 3 eV for  $2\pi^*$  and -14 eV for  $5\sigma$ . Theory and experiments show that when CO is brought in contact with a metal surface the substrate electrons mix with the  $2\pi^*$  and  $5\sigma$  orbitals shifting them towards the Fermi level (see Fig. 2.1). The  $5\sigma$  orbital donates a fraction of charge to the substrate. The  $2\pi^*$  state becomes partially filled and broadens through back donation from the substrate. The

shifted positions of these orbitals have been measured using inverse photoemission and recently two photon photoemission (TPPE). For CO on Cu(111) the  $2\pi^*$  orbital has been measured using TPPE to lie 1 eV below the vacuum with a width of 10-600 meV[33]. The  $5\sigma$  has been measured using inverse photoemission to be at -10 eV [34].

Terminally bound CO has 4 vibrational modes, as depicted in Table (2.1). Both the frustrated rotation and the frustrated translation are two fold degenerate. The frequencies are listed for experimental values and two representative theories. IRAS and EELS studies yield the frequencies of the C-O stretch [35, 36], the Cu-CO stretch [36, 37], and the frustrated rotation (FR) [36, 37]. Inelastic helium scattering studies determined the frustrated translation (FT) frequency for CO on Cu(100)( $\omega_{ft} = 34\text{cm}^{-1}$ )[38].

Direct measurements of  $\omega_{ft}$  for CO on the (111) face of Cu have not been made. Generally  $\omega_{ft}$  can be inferred from the temperature dependence of the CO stretch mode IR absorption. However as discussed in Chapter (6), the temperature range of the current measurements can only place an upper limit of  $110\text{ cm}^{-1}$  on  $\omega_{ft}$ . IR studies of CO on several other metal surfaces give the following frequencies Ni(111)  $\omega_{ft}=60\text{ cm}^{-1}$ , Pt(111)  $\omega_{ft} =60\text{ cm}^{-1}$  Ru(100)  $\omega_{ft}= 105\text{ cm}^{-1}$ . For an estimate of the lower limit of  $\omega_{ft}$  for CO on Cu(111) we use the Cu(100) result which is the lowest measured frequency of  $\omega_{ft}$  on a metal surface. For an upper limit we use the Ni(111) and Pt(111) values of  $60\text{ cm}^{-1}$ .

					O ↓ C □	O C ↓ □	O→ C→ □	O→ C← □
		face	Temp	Method	C-O	M-CO	FT	FR
$\omega \text{ cm}^{-1}$	exp	111	95K	IRAS[36]	2074	-	-	-
				IRAS[37]	-	330	-	281
				see text	-	-	30-60	-
	theory	100	0K	IRAS[37]	2084.6	345	-	285
				HAS[38]	-	-	34	-
theory	100	0K	M.O.[24]	2140	398	45	353	
			D.F.[27]	2179	372	15	357	

Table 2.1: Vibrational Modes of CO on the 100 and 111 faces of Cu.

The  $2\pi^*$  orbital is an antibonding orbital, whereas the  $5\sigma$  bond is neutral to bonding in character. As the  $2\pi^*$  becomes partially filled the CO bond is weakened and hence the decrease in the stretch mode frequency upon absorption. In addition to the chemical shift there is a frequency shift due to dipole-dipole coupling of the CO oscillators. When two coadsorbed CO molecules separated by distance  $r$  oscillate, their transition dipoles ( $\bar{\mu}_{01}$ ) interact with energy  $\sim \bar{\mu}_{01} \bullet \bar{\mu}_{01}/r^3$ . On a partially covered surface with many CO molecules a band of frequencies is generated as a result of this interaction. We are interested primarily in IR probes which sample only the  $q=0$  section of a vibrational band. For oscillators perpendicular to the surface the central absorption frequency shifts towards higher energy. Isotope mixtures can be used to vary nearest neighbor distances (and hence dipole-dipole interaction) while maintaining a constant coverage and chemical shift. From such isotope studies a

bandwidth of  $35 \text{ cm}^{-1}$  is measured for  $(\sqrt{3} \times \sqrt{3})R30^\circ$  CO on Cu(111)[39]. Subtracting this contribution from the observed absorption, the net chemical shift is  $\sim 100 \text{ cm}^{-1}$ , or  $\sim 5 \%$  of the vibrational energy.

The molecular-orbital models use clusters,  $\text{Cu}_n\text{CO}$ , ranging in size from  $n=1$  to  $n=34$  [30]. The electrons are treated self-consistently within the Hartree Fock approximation. Three contributions to the chemisorbed bond are found. A repulsive component arises from the overlap of the substrate and adsorbate orbitals, and attractive components come from polarization of the substrate and charge exchange with the  $5\sigma$  and  $2\pi^*$  orbitals as mentioned. As can be seen from Table (2.1) the molecular orbital calculations give reasonable agreement with the experimental frequencies. They also can explain a variety of other chemisorption properties including, the magnitude of  $2p$  and  $5\sigma$  shifts, the enhanced CO dipole moment (resulting from the  $2\pi^*$  partial occupation), and adsorbate-substrate bond lengths[30]. The limitations of these models are the self-consistent field (SCF) Hartree Fock treatment of the electrons which neglects correlation effects accounted for by other electron treatments, and the finite size of the clusters. Also the molecular orbital basis set lacks completeness making the convergence of results with cluster size difficult to establish.

Recently Rappe et al have studied the CO Cu(100) system using a density functional theory with slabs[27]. The main advantages of this approach are the more accurate treatment of the electrons and the modeling of the system as a semi-infinite

solid. By using a unit cell which repeats in two dimensions parallel to the surface the continuum nature of the substrate phonons and electron bands are intrinsic to the model. A local density approximation for the electrons is used which is superior to the Hartree Fock approximation.

The density functional predictions for the mode frequencies are similar to the MO values. However, the density functional theory brings out a very important issue concerning the frustrated translation. In the density functional theory the normal modes are computed using a constant force model. The calculations indicate that while the C-O stretch, M-CO stretch and the frustrated rotation are all well defined modes, the frustrated translation is not a normal mode of the system. Instead, since the frustrated translation frequency is in the middle of the substrate phonon spectrum, a frustrated translation resonance arises from a collection of substrate phonon modes which involve translations of the CO unit lateral to the Cu surface. The other modes above the phonon spectrum and remain discrete modes.

## **2.2 Adsorbate Vibrations Coupling to Metal Substrate Electron-Hole Pairs**

It would be natural to guess that adsorbate vibrations couple more strongly to substrate phonons than to substrate electrons. The energy separations between electronic states for an isolated molecule, or even a large cluster are usually much larger than

any vibrational quanta in the system. This transition energy mismatch suppresses vibrational electronic energy exchange. However in semi-infinite solids the continuous density of electronic states facilitates transitions between electronic states separated by energies comparable to vibrational quanta.

Early IR measurements of the CO stretch mode indicated an energy relaxation time of 1-2 ps [23]. This value is several orders of magnitude faster than theories predicted for coupling to phonons. Since the Cu phonon spectrum cuts off at  $\sim 250 \text{ cm}^{-1}$ , and the stretch frequency is  $\sim 2000 \text{ cm}^{-1}$  the coupling would involve an 8 phonon process.

In 1980 Persson and Persson developed a description of electron-hole pair interactions with adsorbate vibrations that utilized e-h pairs separated by one adsorbate vibrational quanta [23]. The theory involves the flow of charge between the substrate and a partially filled adsorbate electronic state (Fig. 2.2). As discussed earlier, when the adsorbate is brought in contact with the metal, the normally unoccupied CO  $2\pi^*$  electronic state mixes with the substrate electrons to form hybrid states.

Motion along each vibrational coordinate of the CO alters the occupancy of the  $2\pi^*$  state since the mixing depends upon the particular positions of the adsorbate nuclei. Since the electronic and vibrational degrees of freedom are not completely separable the dynamical charge transfer causes an exchange of energy between the adsorbate vibrations and the substrate electrons. An expression for the coupling rate

## Dynamical Charge Transfer

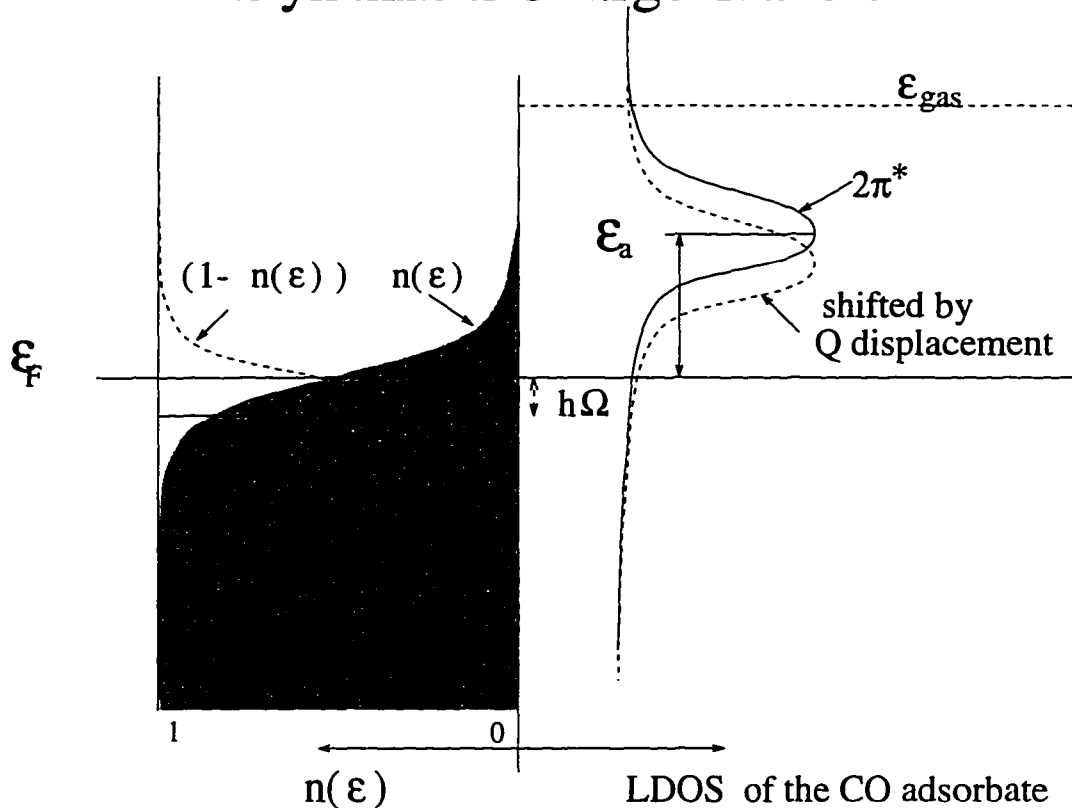


Figure 2.2: The dynamical charge transfer process is illustrated by the electronic density of states for the CO/Cu(111) system. Mixing with the substrate electrons causes the  $2\pi^*$  level to lower and broaden in energy from the gas phase value. Since the amount of mixing depends on the positions of the adsorbate nuclei, movement along a vibrational coordinate  $Q$ , will change the  $2\pi^*$  local density of states (LDOS) and cause charge to flow between the CO and Cu(111) substrate. The relevant energies for this process are the energy of the vibration  $\hbar\Omega$ , the thermal spread of the Fermi function ( $kT_e$ ), and the energy  $\epsilon_a$  of the  $2\pi^*$  LDOS.

between an adsorbate vibration and the substrate electrons ( $\gamma_e$ ) can be derived using the Andersson-Newns Hamiltonian description for the adsorbate hybridization and Fermi's golden rule. We will derive the results herein focusing on the coupling of the substrate electron hole pairs to a low frequency adsorbate vibration with coordinate  $Q$ .

We use the following Hamiltonian which employs a limited electronic basis set,

$$H = \varepsilon'_a(Q)a^\dagger a + \sum_k \varepsilon_k a_k^\dagger a_k + \sum_k (V_{ak}(Q)a^\dagger a_k + h.c.) + \hbar\Omega b^\dagger b. \quad (2.1)$$

where  $\hbar\Omega b^\dagger b$  is the energy of mode  $Q$ . All of the electron states are defined in terms of a ground state  $|0\rangle$ . The substrate electrons are described by extended wave functions ( $|k\rangle = a_k^\dagger|0\rangle$ ) with energies  $\varepsilon_k$  and the adsorbate electronic state is described by an unoccupied molecular orbital ( $|a\rangle = a^\dagger|0\rangle$ ) with energy  $\varepsilon'_a(Q)$  for a fixed displacement  $Q$ . The substrate  $|k\rangle$  states mix with the adsorbate state  $|a\rangle$  through the exchange terms  $V_{ak}(Q)$ . Here,  $\varepsilon'_a(Q)$  is shifted from its gas phase value ( $\varepsilon_{gas}$ ) as a result of all adsorbate/substrate interactions except the  $V_{ak}$  exchange terms.

We now expand the energies  $\varepsilon'_a(Q)$  and  $V_{ak}(Q)$  to first order in  $Q$ ;

$$\varepsilon'_a(Q) = \varepsilon'_a(0) + Q \frac{\partial \varepsilon'_a}{\partial Q}, \quad (2.2)$$

$$V_{ak}(Q) = V_{ak}(0) + Q \frac{\partial V_{ak}}{\partial Q}. \quad (2.3)$$

A perturbation term  $H'$  that couples the electronic ( $|\alpha\rangle$ ), and vibrational ( $|n\rangle$ )

states is defined using the first order terms of the  $\varepsilon'_a(Q)$ , and  $V_{ak}(Q)$  expansions;

$$H' = Q \left( \frac{\partial \varepsilon'_a}{\partial Q} a^\dagger a + \sum_k \left[ \frac{\partial V_{ak}}{\partial Q} a^\dagger a_k + h.c. \right] \right). \quad (2.4)$$

Zerth order hybrid electronic states  $|\alpha\rangle = d_a^\alpha |a\rangle + \sum_k d_k^\alpha |k\rangle = c_\alpha |0\rangle$  with energies  $\varepsilon_\alpha$  are defined by the following zerth order electronic Hamiltonian;

$$\sum_\alpha \varepsilon_\alpha c_\alpha^\dagger c_\alpha = \varepsilon'_a(0) a^\dagger a + \sum_k \varepsilon_k a_k^\dagger a_k + \sum_k (V_{ak}(0) a^\dagger a_k + h.c.). \quad (2.5)$$

Using these new definitions the total Hamiltonian is expressed;

$$H = \sum_\alpha \varepsilon_\alpha c_\alpha^\dagger c_\alpha + \hbar \Omega b^\dagger b + H'. \quad (2.6)$$

In general both  $\frac{\partial \varepsilon'_a}{\partial Q}$  and  $\frac{\partial V_{ak}}{\partial Q}$  will contribute to the coupling. A complete treatment which includes both terms has been carried out by Head-Gordon and Tully [24]. The analysis can be simplified by neglecting the  $\frac{\partial V_{ak}}{\partial Q}$  term and writing  $H'$ ;

$$H' = \Delta_{aa} a^\dagger a (b^\dagger + b) \quad (2.7)$$

where  $\Delta_{aa} = \frac{\partial \varepsilon'_a}{\partial Q} \sqrt{\frac{2\hbar}{\Omega}} = \frac{\partial \varepsilon'_a}{\partial Q} Q_0$ , with  $Q_0$  being the average zero temperature mass weighted coordinate displacement. The derivative terms are important to the value of the magnitude of zero temperature rate but not important to the temperature dependence of the rate (see Ref. [24]). By dropping the  $\frac{\partial V_{ak}}{\partial Q}$  term we will not be able to calculate a reliable zero temperature rate but we will be able to examine the temperature dependence of the rate.

The zero temperature development of Persson [23] is extended to non-zero temperatures by accounting for the occupied and unoccupied density of electronic states with the Fermi-Dirac distribution,  $n(\varepsilon) = 1/(1 - e^{(\varepsilon - \varepsilon_F)/kT})$ . The mixed  $|\alpha\rangle$  states are assumed to be populated as if they are bulk metal electronic states. The energy transfer process of interest involves a transition from vibrational state  $n=1$  to  $n=0$  and the simultaneous scattering of an electron from an occupied hybrid state  $|\alpha\rangle$  to an unoccupied hybrid state  $|\beta\rangle$ , with  $\varepsilon_\beta - \varepsilon_\alpha = \hbar\Omega$ . Fermi's golden rule yields the following expression for the coupling rate:

$$\gamma_e = \frac{2\pi}{\hbar} \sum_{\alpha\beta} |\langle \alpha, n=1 | H' | \beta, n=0 \rangle|^2 n(\varepsilon_\alpha) (1 - n(\varepsilon_\beta)) \delta(\varepsilon_\beta - \varepsilon_\alpha - \hbar\Omega), \quad (2.8)$$

The wave functions  $|\alpha, n\rangle$  represent the product of a hybrid state  $|\alpha\rangle$ , and a Q mode vibrational state  $|n\rangle$ . To evaluate the perturbation terms we need to write them in the hybridized electronic state basis using transformed expressions of the  $a_g$  operators,

$$a_g = \sum_{\lambda} \langle \lambda | a_g \rangle c_{\lambda}. \quad (2.9)$$

Writing the perturbation term as,

$$H' = (b^\dagger + b) \sum_{\lambda\gamma} (\Delta_{aa} \langle a | \lambda \rangle \langle \gamma | a \rangle c_{\lambda}^\dagger c_{\gamma} + h.c.), \quad (2.10)$$

the matrix elements in the rate expression become,

$$\langle \beta n=0 | H' | \alpha n=1 \rangle = \sum_{\lambda\gamma} \Delta_{aa} \langle a | \lambda \rangle \langle \gamma | a \rangle \langle \beta | c_{\lambda}^\dagger c_{\gamma} | \alpha \rangle \quad (2.11)$$

$$= \Delta_{aa} \langle a | \beta \rangle \langle \alpha | a \rangle \quad (2.12)$$

Also note that:

$$\delta(\varepsilon_\beta - \varepsilon_\alpha - \hbar\Omega) = \int_{-\infty}^{\infty} \partial\varepsilon \delta(\varepsilon - \varepsilon_\alpha) \delta(\varepsilon_\beta - \varepsilon - \hbar\Omega) \quad (2.13)$$

The coupling rate can then be expressed;

$$\gamma_e = \frac{2\pi}{\hbar} \Delta_{aa}^2 \int_{-\infty}^{\infty} \partial\varepsilon \left[ \sum_{\alpha} | \langle \alpha | a \rangle |^2 \delta(\varepsilon - \varepsilon_\alpha) \right] \quad (2.14)$$

$$x \left[ \sum_{\beta} | \langle a | \beta \rangle |^2 \delta(\varepsilon_\beta - \varepsilon - \hbar\Omega) \right] n(\varepsilon) (1 - n(\varepsilon + \hbar\Omega)) \quad (2.15)$$

The sums and delta functions can be identified as the local density of states for the adsorbate orbitals.

$$\left[ \sum_{\alpha} | \langle \alpha | a \rangle |^2 \delta(\varepsilon - \varepsilon_\alpha) \right] = \rho_a(\varepsilon) \quad (2.16)$$

Finally the coupling rate  $\gamma_e$  is rewritten in terms  $\rho_a(\varepsilon)$ ,

$$\gamma_e = \frac{2\pi}{\hbar} |\Delta_{aa}|^2 \int_{-\infty}^{\infty} d\varepsilon \rho_a(\varepsilon) \rho_a(\varepsilon + \hbar\Omega) n(\varepsilon) (1 - n(\varepsilon + \hbar\Omega)). \quad (2.17)$$

For  $T=0$  the Fermi distributions  $n(\varepsilon)$ , can be replaced with step functions and equation (2.17) reduces to the Persson result (Ref. [23]):

$$\gamma_e^0 = \frac{2\pi}{\hbar} |\Delta_{aa}|^2 \int_{\varepsilon_F - \hbar\Omega}^{\varepsilon_F} d\varepsilon \rho_a(\varepsilon) \rho_a(\varepsilon + \hbar\Omega). \quad (2.18)$$

However, when  $kT_e$  is comparable to, or larger than  $\hbar\Omega$ , equation (2.17) must be used.

A temperature dependence is thus introduced through the temperature dependence of the Fermi distribution. This effect can be considered in two regimes as

depicted in Fig. 2.3. For temperatures much less than the energy of the  $2\pi^*$  level  $\varepsilon_a$ ,  $\rho_a(\varepsilon)$  is essentially constant over the interval of integration in equation (2.17)[23, 24]. The coupling rate is then expressed in terms of  $\gamma_e^0$  and a temperature factor, i.e.

$$\gamma_e(T_e) = \frac{\gamma_e^0}{1 - e^{-\hbar\Omega/kT_e}} \quad (2.19)$$

For temperatures approaching  $\varepsilon_a/10$  or greater, the shape of the  $2\pi^*$  LDOS must also be included. We model  $\rho_a(\varepsilon)$  as a Lorentzian with line center 3.35 eV above  $\varepsilon_F$ , and line width  $\sim 0.6$  eV[33]. Equation (2.17) was numerically integrated and is depicted in Fig.2.3. A sharp increase in the coupling strength occurs as the substrate electrons achieve thermal energies sufficient to make near resonant transitions. For temperatures higher than  $\varepsilon_a$  the resonant effect saturates and the coupling becomes less sensitive to temperature again. Similar resonance enhanced couplings have been predicted by Brandbyge et al using a path integral technique to evaluate an electronic friction within a Langevin formalism[40]. The resulting electron temperature dependent adsorbate/substrate coupling was used to explain femtosecond laser desorption experiments.

Both molecular orbital techniques [24, 41] and density functional calculations[42] have been applied to the problem of determining the hybridization of adsorbate electronic state and the derivative of the system energy with respect to the different vibrational coordinates. With a molecular orbital calculation for copper clusters, Head-Gordon et al [24] arrive at a temperature dependent coupling rate similar to

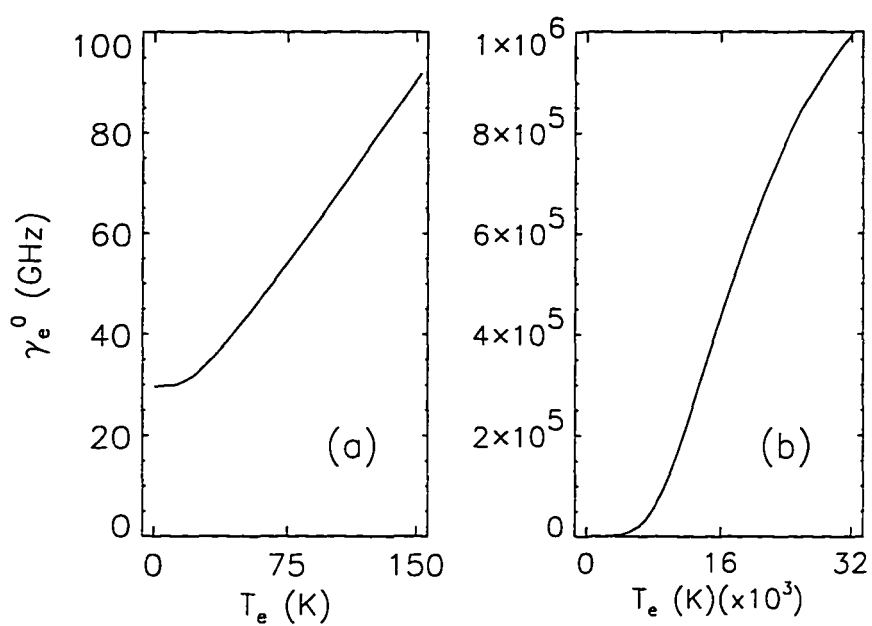


Figure 2.3: Temperature dependence of  $\gamma_e$  predicted by the dynamical charge transfer model using the values  $\gamma_e^0 = 30$  GHz and  $\hbar\Omega = 45$   $\text{cm}^{-1}$ . (a) For  $T_e \ll \epsilon_a$ , (b) For  $T_e \sim \epsilon_a$ .

equation (2.19). Their calculations go further than those presented here and provide an ab initio prediction for the zero temperature rate  $\gamma_e^0$ . They extend the analysis using molecular dynamics calculations with electronic friction to predict both  $\gamma_e$  and  $\gamma_i$  at nonzero temperatures. These calculations predict temperature dependent couplings to both the electron and the phonon reservoirs. A comparison between their predictions and our findings will be presented in Chapter (6).

### 2.3 Time Dependent Dephasing of Adsorbate Vibrations

Direct measurements of low frequency ( $10\text{-}500\text{ cm}^{-1}$ ) adsorbate vibrational dynamics are hindered by the lack of ultrafast laser probes in the relevant spectral region. However the couplings and dynamics of these adsorbate modes are of great interest, particularly because excitations of these modes are involved in desorption, diffusion and other surface reactions. Current femtosecond infrared probes using nonlinear crystals for infrared generation are capable of frequencies as low as  $1000\text{ cm}^{-1}$ [28]. Presently within the area of surface vibrational dynamics only the dynamics of modes with  $\nu > 1800\text{cm}^{-1}$  have been measured.

Static spectroscopic techniques on the other hand can cover the entire Far IR range from a few wavenumbers through to the visible. IRAS and electron energy loss techniques can access modes with  $\nu > 200\text{cm}^{-1}$ . The lowest energy modes in the range below  $200\text{ cm}^{-1}$  can be studied with inelastic helium scattering. However the

conversion of these techniques to ultrafast timescales does not seem likely. The most promising spectroscopic technique which might permit direct studies of modes with energies ( $<100\text{ cm}^{-1}$ ) is femtosecond terahertz spectroscopy[43]. While the technique has been applied to semiconductor studies, this technique has not yet been successfully applied to surface vibrations[44]. The challenges of working with ultrafast terahertz spectroscopy include generating enough light, focusing, and detection[43].

Though femtosecond probes are not currently available for direct measurements, the populations of low frequency modes can be monitored *indirectly* via the effects they have on higher frequency modes. In this case, the excitation of low frequency modes modifies the vibrational dynamics of some higher frequency mode which may in turn be accessible to current ultrafast IR probes. This section discusses time-dependent dephasing of high frequency modes due to anharmonic coupling to lower frequency modes. The goal is to measure the coupling rates discussed in the previous section between low frequency adsorbate vibrations and the substrate electron and phonon reservoirs.

The temperature dependence of vibrational bands in polyatomic molecules is generally understood to arise from anharmonic couplings between high frequency modes and thermally populated lower frequency modes [45]. The molecular nuclear motions are coupled to each other and also to the modes of a bath. The details of these bath modes depends on the molecule's environment (see Fig. 2.4). This situation permits

any particular vibrational frequency to be modulated by the bath fluctuations and hence yield line-shifting and line-broadening phenomena. To shift a high frequency transition in this way it is necessary to have a low frequency mode, whose occupation number is significant. The magnitude of the temperature shift or broadening will depend on the size of the anharmonic coupling between the high and low frequency modes. The theory that describes this situation is termed exchange theory[45, 46]. In the present context the dynamics are regarded in terms of Brownian oscillator models[46, 47].

The simplest type of vibrational dynamics consists of an oscillator, representing say a diatomic molecule, coupled to a temperature reservoir. In this case the temperature-dependent spectral shifts are caused by the changes in molecular potential that arise because of coupling to the motions of molecules in the bath [45]. When some modes of the bath are efficiently anharmonically coupled to the oscillator, the spectral properties of the oscillator may be described by its coupling to these modes only.

Fig. 2.4 depicts the situation in which a high frequency vibration  $\rho$  is strongly anharmonically coupled to a particular low frequency mode  $Q$ . Both  $\rho$  and  $Q$  are coupled directly to a temperature reservoir. Since  $Q$  has a much lower frequency it will be thermally populated to a much larger degree than  $\rho$ . Through the anharmonic coupling of these two modes the stochastic modulations of  $Q$  by the bath modes

Dephasing of a high frequency vibration by  
a thermally populated low frequency vibration

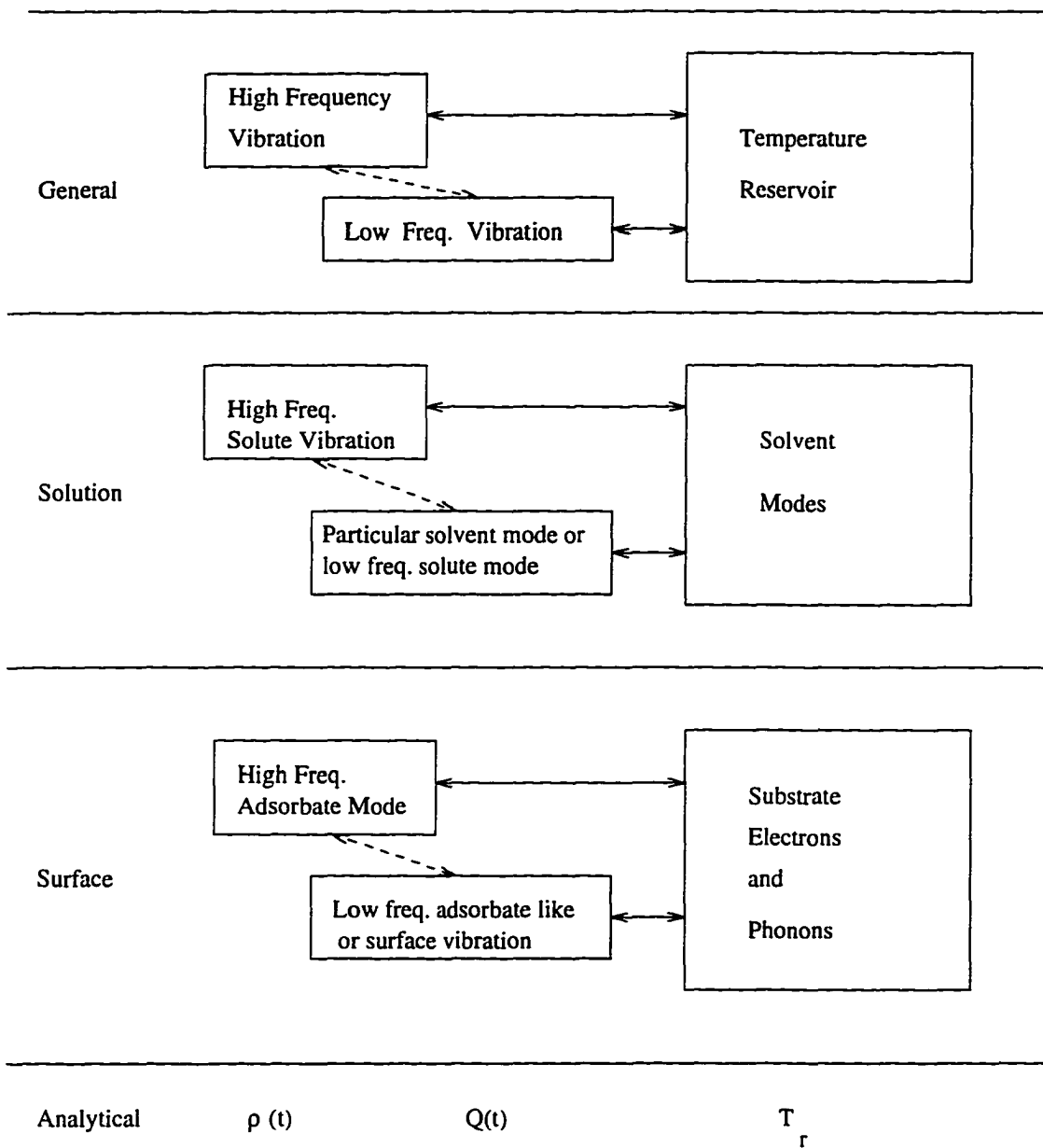


Figure 2.4: Schematic of stochastic Brownian oscillator. Solid lines represent energy transfer. Dashed lines represent an adiabatic anharmonic coupling.

will in turn modulate the frequency of  $\rho$ . In the case of a molecule in solution the temperature bath would be the solvent and a high frequency solute mode would be dephased through a particular solute mode or perhaps a group of solvent modes. In the case of an adsorbate the temperature reservoirs are the substrate electronic and the phonon degrees of freedom and a high frequency adsorbate vibration will be dephased through an anharmonic coupling to a low frequency adsorbate mode or surface phonon. The following discussion will provide a semi-classical treatment of the system. The substrate baths and the  $Q$  mode will be considered classically and the stretch mode will be treated as a quantum harmonic oscillator with density matrix  $\rho$ .

The anharmonic coupling between the CO stretch and the  $Q$  modes causes the CO stretch frequency and thus the density matrix elements of  $\rho$  to be modulated. This coupling can be depicted by the potential wells for the low frequency  $Q$  coordinate motion, Fig. 2.5. If there were no anharmonic coupling the curvature of the  $\nu = 0$  and  $\nu = 1$  levels would be the same and the stretch frequency, determined by the distance between the two potential surfaces, would then be independent of the  $Q$  position. However when the modes are coupled, the  $\nu = 0$  and  $\nu = 1$  levels have different curvatures. The anharmonic coupling usually causes the frequency  $\Omega$  to be lower when the CO stretch is excited than if it is not. Conversely the farther the  $Q$  mode is from the equilibrium position the lower the CO stretch frequency.

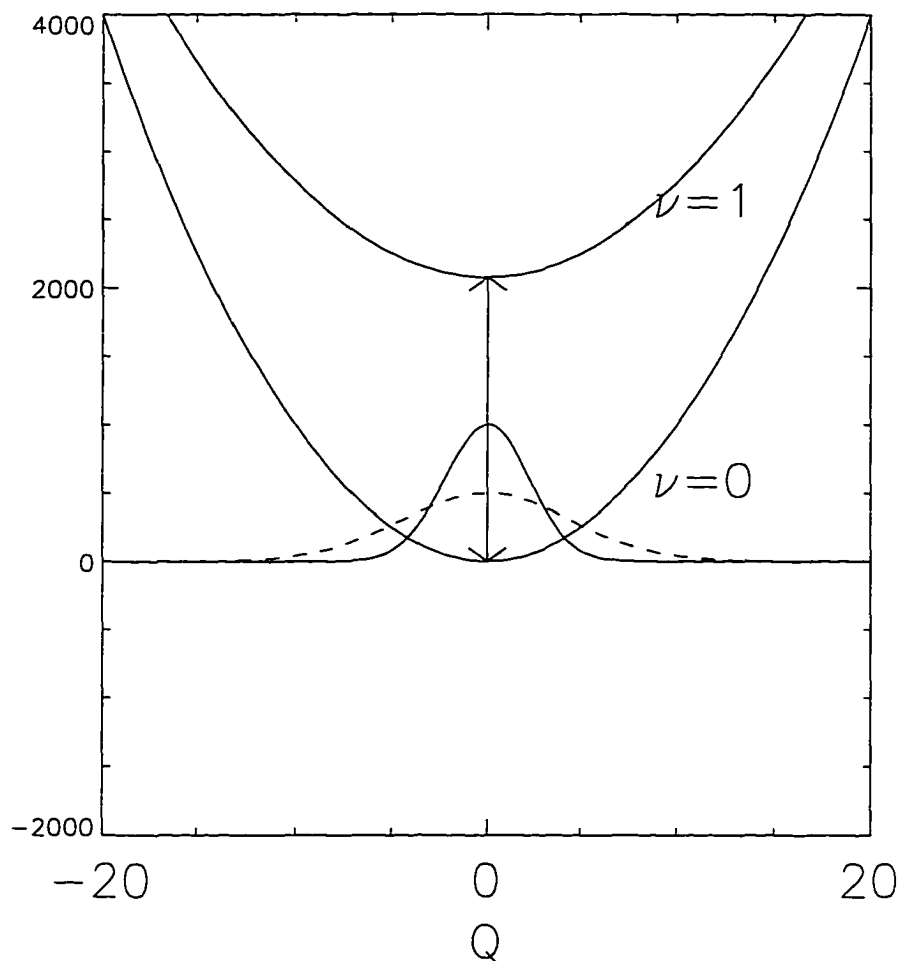


Figure 2.5: Anharmonic coupling between the CO stretch and a low frequency oscillator  $Q$  will modulate the frequencies of both modes. The frequency  $\Omega$  of the coordinate  $Q$  oscillator is determined by the width of the potential wells. The frequency  $\omega(Q)$  of the CO stretch mode is determined by the separation of the two potential surfaces. As  $\langle Q^2 \rangle$  increases the average stretch frequency decrease. Using a stochastic Brownian oscillator model the temperature dependence of the frequency shift can be obtained explicitly (see text).

We start by writing an equation for  $\rho$ . In anticipation of probing the CO with an electric field at frequency  $\omega_L$  we define the stretch detuning frequency,  $\Delta_{01}(Q) = \omega_{01}(Q) + \omega_L$  that can be written in terms of the low frequency mode displacement  $Q$ :

$$\Delta_{01}(Q) = \Delta_{01} + (\zeta/\hbar)Q^2 \quad (2.20)$$

Here  $\zeta = \frac{1}{2}(\Omega_0^2 - \Omega_1^2)$  is a measure of the anharmonic coupling;  $\Omega_v$  is the Brownian oscillator frequency in state  $v$  of the CO stretch. The pure case density matrix,  $\sigma$ , for the CO stretch now contains a stochastic frequency:

$$\dot{\sigma}_{01} = -\{i\Delta_{01} + \gamma_0 + i\frac{\zeta}{\hbar}Q^2(t)\}\sigma_{01} \quad , \quad (2.21)$$

where  $\gamma_0$  is the phase relaxation time of the CO-stretch resulting from other mechanisms. The time evolution of  $\sigma_{01}$  can be obtained by integration (see appendix 9.2) that yields;

$$\sigma_{01}(t) = \sigma_{01}(0)e^{\{-i[\Delta_{01}t + \frac{\zeta}{\hbar} \int_0^t dt_1 Q^2(t_1)] - \gamma_0 t\}} \quad (2.22)$$

We now need to take the ensemble average to obtain  $\rho_{01}$  where  $\rho_{01} = \langle \sigma_{01} \rangle$ . Such a stochastic equation can be solved using a cummulant expansion (Ref. [46]) which gives;

$$\rho_{01}(t) = \rho_{01}(0)e^{\{-i[\Delta_{01}t + \frac{\zeta}{\hbar} \int_0^t dt_1 \langle Q^2(t_1) \rangle] - \gamma_0 t - \frac{\zeta^2}{\hbar^2} \int_0^t dt_1 \int_0^{t_1} dt_2 \langle (Q^2(t_1)Q^2(t_1-t_2)) \rangle\}} \quad . \quad (2.23)$$

or alternatively,

$$\rho_{01} = \rho_{01}(0)e^{-\{\int_0^t dt_1 i[\Delta_{01} + \delta_s(t_1)] + \gamma_0 + \gamma_s(t_1)\}} \quad (2.24)$$

where  $\delta_s(t_1) = \frac{1}{\hbar} \langle Q^2(t_1) \rangle$  and  $\gamma_s(t_1) = \frac{1}{\hbar^2} \int_0^{t_1} dt_2 \langle \langle Q^2(t_1) Q^2(t_1 - t_2) \rangle \rangle$ . The propagator for the density matrix, from which the response to an IR probe field can be calculated, can be readily obtained by differentiating  $\rho_{01}(t)$ ;

$$\dot{\rho}_{01} = -\{i[\Delta_{01} + \delta_s(t)] + \gamma_0 + \gamma_s(t)\} \rho_{01} \quad (2.25)$$

The interaction with the IR probe field will be discussed later in Chapter 4.

From equation (2.25) it is seen that the mean value  $\langle Q^2(t) \rangle$  determines the shift of the stretching mode and the cummulant average  $\langle \langle Q^2(t) Q^2(t - t_1) \rangle \rangle$  determines the temperature dependent dephasing (width) of the transition. These averages of  $Q$  are obtained from the equation of motion for  $Q$ . The  $Q$  mode is considered to be a Brownian oscillator satisfying a Langevin equation:

$$\ddot{Q} + \eta_i \dot{Q} + \Omega^2 Q = \frac{F(t)}{\sqrt{\mu}} \quad (2.26)$$

having frequencies  $\Omega$ , reduced mass  $\mu$  and damping rate  $\eta$ . Here  $F(t)$  is a stochastically fluctuating force that has no memory:

$$\langle F(t_1) F(t_2) \rangle = 2\eta\mu k_b T(t_1) \delta(t_1 - t_2) \quad (2.27)$$

where  $T(t)$  is the temperature of the bath. Note that the anharmonic coupling is not included in the equation of motion for  $Q$ . This approximation can be made since the interactions with the reservoir, through  $\eta$  and  $F(t)$ , are much stronger than the perturbation due to the anharmonic coupling to the stretch mode.

The shift and width parameters that are obtained depend on the value of  $\Omega/\eta$ , but for the present purpose we assume the oscillator is strongly overdamped since it is then straight-forward to obtain the needed results in terms of the relaxation time of the Brownian oscillator,  $\beta = \Omega^2/\eta$ . The Langevin equation becomes;

$$\dot{Q} + \beta Q = \frac{F(t)}{\eta\sqrt{\mu}} \quad (2.28)$$

which integrates to (see appendix 9.2);

$$Q(t) = \int_{-\infty}^t dt' \frac{F(t')}{\eta\sqrt{\mu}} e^{-\beta(t-t')}. \quad (2.29)$$

The time dependence of the mean squared displacement of Q can now be simply obtained:

$$\langle Q^2(t) \rangle = \int_{-\infty}^t dt' \int_{-\infty}^t dt'' \frac{\langle F(t')F(t'') \rangle}{\eta^2\mu} e^{-\beta(t-t'+t-t'')} \quad (2.30)$$

$$= \frac{2k_b}{\eta} \int_{-\infty}^t dt' T(t') e^{-2\beta(t-t')} \quad (2.31)$$

Note that  $\langle Q^2(t) \rangle$  follows the reservoir temperature T(t) with rate  $2\beta$ . For a quantum harmonic oscillator the mean squared displacement is proportional to the oscillator population. In the next section we will derive a similar energy transfer rate equation treating the Q mode as a quantum harmonic oscillator. It will be shown that the Brownian oscillator response time is related to the energy transfer rate described earlier section 2.2 by  $\gamma = 2\beta$ .

The cummulant average in the width term,  $\gamma(t)$ , can be analyzed assuming that

$Q(t)$  is a stochastic Gaussian variable. In this case we have;

$$\langle\langle Q^2(t)Q^2(t') \rangle\rangle = \langle Q^2(t)Q^2(t') \rangle - \langle Q^2(t) \rangle \langle Q^2(t') \rangle \quad (2.32)$$

$$\langle\langle Q^2(t)Q^2(t') \rangle\rangle = 2 * \langle Q(t)Q(t') \rangle^2 \quad (2.33)$$

To evaluate this we note that,

$$\langle Q(t)Q(t_1) \rangle = \int_{-\infty}^t dt' \int_{-\infty}^{t_1} dt'' \frac{\langle F(t')F(t'') \rangle}{\eta\sqrt{\mu}} e^{-\beta(t-t'+t_1-t'')} \quad (2.34)$$

$$= e^{-\beta(t-t_1)} \frac{2k_b}{\eta} \int_{-\infty}^{t_1} dt'' T(t'') e^{-2\beta(t_1-t'')} \quad (2.35)$$

$$= e^{-\beta(t-t_1)} \langle Q^2(t_1) \rangle \quad (2.36)$$

Defining  $\delta\omega = \frac{\zeta}{\Omega}$  and noting that,  $\frac{\zeta}{\hbar} \frac{2k_b}{\eta} = \delta\omega \left(\frac{k_b}{\hbar\Omega}\right) 2\beta$ , the explicit forms for  $\delta_s(t)$  and  $\gamma_s(t)$  can be written;

$$\delta_s(t) = \delta\omega \left(\frac{k_b}{\hbar\Omega}\right) 2\beta \int_{-\infty}^t dt' T(t') e^{-2\beta(t-t')} \quad (2.37)$$

$$\gamma_s(t) = 2 \int_0^t dt_1 [\delta_s(t_1)]^2 e^{-2\beta(t-t_1)} \quad (2.38)$$

Note that the time dependence of the width will lag the behind the square of the frequency shift  $\delta_s(t)^2$  at rate  $\beta$ . However this analysis has neglected the stretch mode dipole-dipole coupling effects. Including the dipole-dipole coupling effects is beyond the scope of this discussion. However these effects are important, especially when comparing the magnitudes of  $\delta_s(t)$  and  $\gamma_s(t)$ . A more complete development of the static long time dephasing that includes dipole-dipole interactions has be discussed by Persson et al[48]. When the dispersion of the stretch mode is accounted for, the

coupling time,  $\beta$ , in equation 2.38 is replaced by  $W$  such that:

$$\frac{1}{W} = \sum_{q'} \frac{\beta}{\beta^2 + (\Omega_q - \Omega_{q'})^2} \quad (2.39)$$

The dispersion of the stretch mode is represented by the wave vectors  $q$  and  $q'$  where  $\Omega_q$  is the frequency of the  $q=0$  band and  $q'$  sums over all modes. For the case that  $W \gg \beta$  equation 2.38 can be integrated to obtain:

$$\gamma_s(t) = \frac{1}{W} [\delta_s(t_1)]^2 \quad (2.40)$$

Thus we arrive at two equations for the time dependence of the linewidth (Eq. 2.37) and the center frequency (Eq. 2.40) of the stretch mode absorption. If the time evolution of the temperature reservoirs is known then  $\delta_s(t)$  and  $\gamma_s(t)$  can be computed given the three following parameters;  $\frac{\delta\omega}{\hbar\Omega}$  the ratio of the anharmonic coupling and  $\hbar\Omega$ ,  $\beta$  the Brownian oscillator response time and  $W$  as defined in Eq. 2.39. Since the energy transfer time  $\beta$  between the bath and mode  $Q$  is the parameter we are interested in measuring, we need to establish the values of the other two parameters. This can be done by considering the case of a constant bath temperature.

In the long time limit ( $\beta t \gg 1$ ) and small  $\frac{1}{T} \frac{dT(t)}{dt}$ , these parameters become:

$$\delta_s(T) = \delta\Omega(k_B T / \hbar\Omega) \quad (2.41)$$

$$\gamma_s(T) = (\delta_s(T))^2 / W \quad (2.42)$$

These two equations can be used to describe the line shifting and broadening of spectra obtained from the CW techniques. By first performing static spectroscopy

the values of  $\frac{\delta\omega}{\hbar\Omega}$  and  $W$  can be obtained leaving the Brownian oscillator response time to be determined using transient measurements as mentioned above.

## 2.4 General Theory of a Quantum Harmonic Oscillator Coupled to Two Temperature Reservoirs.

In section 2.2 Fermi's golden ruled was used to calculate the relaxation rate of a quantum harmonic oscillator in the first excited state coupled to substrate electrons. In section 2.3 we used the Langevin equation to couple a classical harmonic oscillator to a temperature reservoir. This section will establish a connection between the coupling rate of section 2.2 and the Brownian oscillator response time  $\beta$  of section 2.3. To make the connection we show that the single level relaxation rate also describes the energy transfer between a thermally excited harmonic oscillator and a bath.

In the case of a metal adsorbate system there are two reservoirs (i.e. bulk electron and phonon) whose temperatures vary in different ways before equilibrating (Chapter 3). When an oscillator with average energy  $U_{osc}$ , characterized by a temperature  $T_{osc}$  (in the Bose-Einstein sense), is placed in contact with a thermal reservoir at temperature  $T_R$ , energy is exchanged until the oscillator acquires the reservoir temperature  $T_R$ . For a harmonic oscillator the time evolution of this process can be calculated explicitly and, with some reasonable assumptions has a very simple form. The calculation depends only on the oscillator frequency, the average occupation of

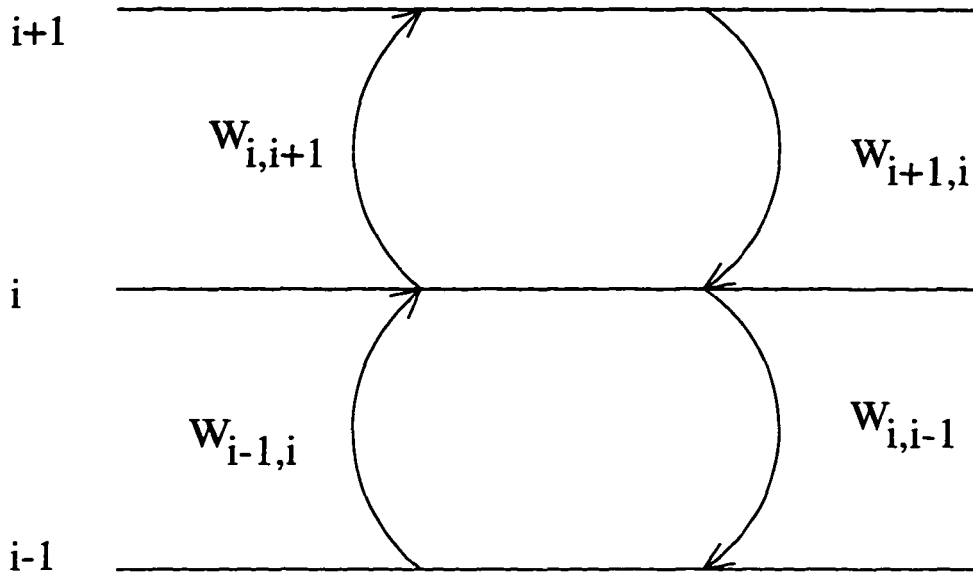


Figure 2.6: Energy flow between levels of a harmonic oscillator.

elementary excitations in the reservoir at the oscillator frequency, and the rate  $\gamma$  associated with the population relaxation between the lowest two oscillator energy levels in the presence of the reservoir. This rate, in our specific case, will be the rates  $\gamma_e$  or  $\gamma_l$  discussed earlier in the Chapter (Eqs. 2.17 and 2.19). For this model,  $\gamma$  is temperature-independent and the elementary *excitations* in the temperature reservoirs are bosons. By considering the energy flow or population transfer in and out of the  $i^{\text{th}}$  level of a harmonic oscillator (Fig. 2.6) we can write the rate of change in occupation probability of the  $i^{\text{th}}$  level,  $p_i$  as follows:

$$\dot{p}_i = p_{i-1}W_{i-1,i} - p_i(W_{i,i+1} + W_{i,i-1}) + p_{i+1}W_{i+1,i} . \quad (2.43)$$

Here  $W_{i,j}$  is the rate of population transfer from the  $i$  level to the  $j$  level. We can simply calculate the rate change of the average occupation number  $\bar{n} = \sum i p_i$ , using  $\dot{\bar{n}} = \sum i \dot{p}_i$ . For a harmonic oscillator with a linear coupling to a bath at temperature  $T_r$ ,

$$W_{i,i+1} = n_r \gamma(i+1) \quad (2.44)$$

$$W_{i+1,i} = (n_r + 1) \gamma(i+1), \quad (2.45)$$

where  $n_r = \bar{n}(T_r)$ , is the average occupation number for an oscillator *in equilibrium* with the harmonic bath. Substituting (2.44) and (2.45) for  $\dot{p}_i$  in expression (2.43) we find that,  $\dot{\bar{n}}$  is,

$$\dot{\bar{n}} = \gamma \left\{ n_r \sum_i i^2 p_{i-1} - (2n_r + 1) \sum_i i^2 p_i + (n_r + 1) \sum_i i^2 p_{i+1} - n_r \sum_i i p_i + (n_r + 1) \sum_i i p_{i+1} \right\}. \quad (2.46)$$

The sums can all be rewritten in terms of  $\bar{n}$ ,  $p_0$ , and  $\sum_i i^2 p_i$ , which, when collected, yield the simple expression,

$$\dot{\bar{n}} = \gamma(n_r - \bar{n}). \quad (2.47)$$

In the high temperature limit equation (2.47) reduces to the form below, since  $\bar{n} = \frac{1}{e^{\hbar\omega/k_B T} - 1}$ :

$$\dot{T}_{osc} = \gamma(T_r - T_{osc}). \quad (2.48)$$

In our case the oscillator can couple to phonons or electron-hole pair fluctuations in the bulk. The occupation of both classes of elementary excitations are described

by Bose distributions at the appropriate electron or phonon reservoir temperatures  $T_e$  and  $T_l$  respectively. If we assumed the couplings are independent of each other, then the energy flow in and out of the oscillator equals the sum of the interactions with the two baths and equation (2.47) can be extended to read,

$$\dot{\bar{n}} = \gamma_e(\bar{n}(T_e) - \bar{n}) + \gamma_l(\bar{n}(T_l) - \bar{n}). \quad (2.49)$$

In reaching equation (2.49) we have assumed that there are no off-diagonal density matrix elements induced by interactions with the bath, and that the coupling to the bath is linear in the oscillator coordinate.

The rate equation for  $\bar{n}$  developed here can be compared to the results for  $Q$  of the previous section (Eq. 2.38). The equations for the linewidth and center frequency shifts can be expressed in terms of the mean squared displacement of the low frequency oscillator  $Q$ . For a quantum oscillator the mean squared displacement  $\langle Q^2 \rangle$  is proportional to  $\bar{n}$  with  $\langle Q^2 \rangle = Q_0^2(\bar{n} + \frac{1}{2})$  and  $Q_0$  is the zero point displacement  $Q_0 = \sqrt{\frac{2\hbar}{\Omega}}$ . By substituting the classical description of  $\langle Q^2 \rangle$  with a quantum description we obtain the following expressions for the complex frequency of the stretch vibration.

$$\delta_s(t) = \frac{\eta}{\hbar} Q_0^2 \left( \bar{n}(t) + \frac{1}{2} \right) \quad (2.50)$$

$$\gamma_s(t) = \frac{\eta^2 Q_0^4}{\hbar^2 W} \left( \bar{n}(t)[\bar{n}(t) + 1] + \frac{1}{4} \right) \quad (2.51)$$

These equations in addition to the rate equation (2.49) predict the transient spectral

response of the CO stretch given the time dependent temperatures of the substrate electrons and phonons. The next section discusses these substrate reservoirs.

## Chapter 3

### Substrate Response To Ultrashort Visible Excitation

The dynamics of adsorbates becomes particularly interesting when ultrashort laser pulses are used to excite the underlying substrate. This is because, on very short timescales, it is possible to excite the pure electronic degrees of the solid before energy can be substantially exchanged with the phonon degrees of freedom of the solid. Eventually we expect the electron and phonon temperature reservoirs to equilibrate, however just after excitation a unique environment can be created for the molecule in which the substrate electron and phonon temperatures are vastly different. These conditions cannot be achieved by conventional thermal heating processes.

Our interest is in the variation of adsorbate vibrational spectra just after substrate excitation. This response will depend on the coupling between the adsorbate vibrations and the near surface bulk phonon and electronic excitations. The population of the adsorbate vibrations induced by the bulk excitations will depend on the temperature of the respective substrate reservoirs. Here we review the current picture

[29, 49, 50, 51, 52, 53, 54, 55, 56] of the substrate temperature variations following ultrafast laser pulse excitation.

The initial interaction of the substrate with the visible electromagnetic field produces a hot electron-hole plasma. This highly nonequilibrium distribution of electrons and holes will thermalize in less than a picosecond. For some metals such as Au, this thermalization time can be as long as 600 fs [56], however for Cu this time is 30-70 fs [9]. Our light pulses have  $\approx 300$  fs duration and enable us to treat this electronic thermalization as essentially instantaneous. Once the electrons have thermalized the cooling problem can be considered in the context of a classical heat flow model first suggested by Anisimov [29]. In this model the cooling of electrons occurs via energy transfer to the phonons through electron-phonon collisions and via heat conduction away from the surface. These equilibration processes are fast, but before the two reservoirs thermalize, the electrons can reach peak temperatures much greater than those of the phonons. The coupled differential equations that describe these processes are as follows:

$$C_e(T_e) \frac{\partial T_e}{\partial t} = \nabla \kappa_e \nabla T_e - g(T_e - T_l) + S(\mathbf{z}, t), \quad (3.1)$$

$$C_l \frac{\partial T_l}{\partial t} = -G(T_l - T_e). \quad (3.2)$$

Here a source term  $S(\mathbf{z}, t)$  accounts for the initial deposition of heat by the light pulse, and is assumed to interact with the electrons only. The electrons have a heat capacity which depends linearly on temperature,  $C_e = \gamma T_e$ , and are subject to thermal

diffusion characterized by  $\kappa_e$ , and coupled to the phonons with rate  $G$ . The phonons, with a fixed heat capacity  $C_l$ , couple to the electronic reservoir temperature with rate  $G$ . Diffusion of energy through phonon mechanisms is negligible on these timescales and is ignored here.

The best measurements for the Cu electron-phonon coupling parameter  $G$  have been derived from transient reflectivity measurements of thin Cu films where the effect of diffusion is minimized due to the 2 dimensional nature of the samples[50, 54, 55]. For polycrystalline Cu this value is  $G = 0.7 \times 10^{17} - 1 \times 10^{17} \text{ W/m}^3\text{K}$ . Grain boundaries are believed to enhance the electron-phonon scattering process, so that single crystals might be expected to have smaller values of  $G$ . For Au, a comparison of polycrystalline films to single crystal thin films has been made and the single crystal  $G$  was 10 – 20% smaller than the polycrystalline sample [55]. Unless otherwise stated we have used a value of  $G = 0.7 \times 10^{17} \text{ W/m}^3\text{K}$ . The diffusion constant  $\kappa_e$ , is temperature dependent and has the form,  $\kappa_e = \kappa_{e0}(T_e/T_l)$  with  $\kappa_{e0} = 435 \text{ W/mK}$  [9, 51]. The heat capacities have been determined experimentally with  $C_e = 96.6 T_e \text{ J/m}^3\text{K}^2$  and  $C_l = 2.26 \times 10^6 \text{ J/m}^3\text{K}$  [57].

The problem must generally be treated in three dimensions. In our experiments however, the laser beam waists of  $\sim 100 \mu\text{m}$  were  $\geq 10^4$  times the penetration depth of the incident light. The heat will diffuse during the experiment but we anticipate (and will later check) that the depth will be increased by a factor of less than 100

during the timescale of our measurements ( $t < 50ps$ ). In this case the temperatures can be considered homogeneous in the plane of the crystal surface and the diffusion problem is effectively one dimensional in the direction,  $z$ , normal to the surface.

The heat can not diffuse into the vacuum and so the surfaces have boundary conditions of  $(\frac{\partial T_e}{\partial z})_{z=0} = (\frac{\partial T_l}{\partial z})_{z=0} = 0$  and  $(\frac{\partial T_e}{\partial z})_{z=z_{max}} = (\frac{\partial T_l}{\partial z})_{z=z_{max}} = 0$ . Since the sample depth (2mm) is many orders of magnitude greater than the heat penetration depth we increased  $z_{max}$  until no change is seen in the calculated front surface temperature ( $z_{max} \sim 1000$  times the optical skin depth). We have solved these equations numerically with a time centered Crank-Nicholson scheme[58] for our system parameters (see Appendix. 9.3). A 500 fs light pulse that deposits an absorbed fluence of  $F_{abs} = 0.33 \text{ mJ/cm}^2$  will induce an electron temperature rise of  $\delta T_e = 380\text{K}$  at the Cu surface(see Fig. 3.1). This elevated electron temperature will decay in  $\sim 1$  ps primarily through electron-electron heat diffusion into the bulk. The surface phonon temperature in contrast rises more gradually and increases by a smaller amount (i.e.  $\delta T_l = 7 \text{ K}$ ). Since the diffusion of heat away from the surface is dominated by the electrons,  $T_e$  drops slightly below  $T_l$  and both temperatures return to 95 K in  $\leq 1$  ns. The temperature dependence of  $\kappa_e$  means that initially the heat diffuses quite fast and then as  $T_e$  returns to a value  $\sim T_l$  the diffusion slows down. Thus the effective deposition depth for the duration of the experiment is reached after the first 1-2 ps. The temperature profile with respect to the depth within the substrate

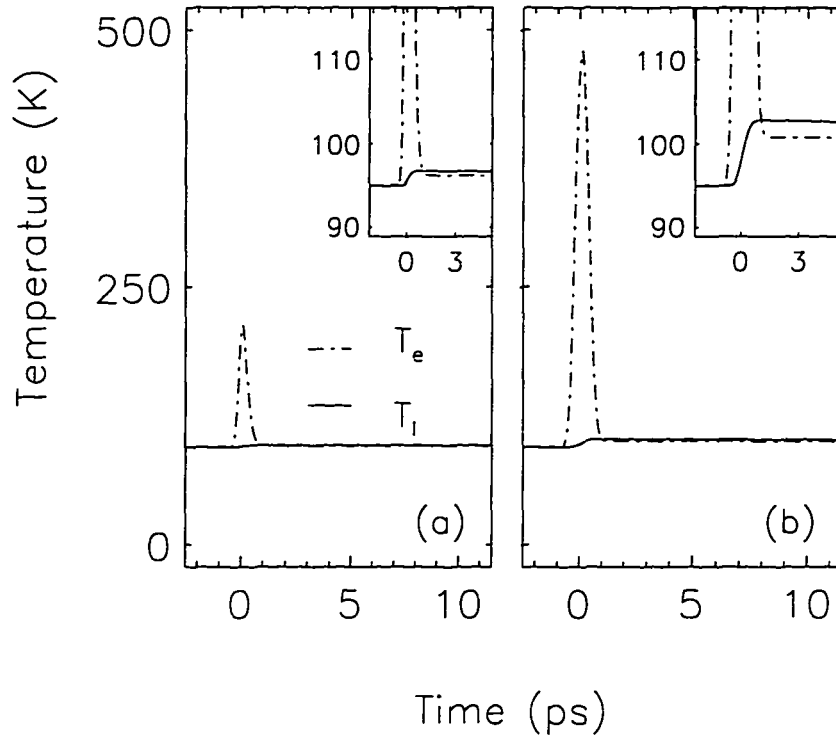


Figure 3.1: The substrate temperatures,  $T_e$  and  $T_l$ , induced by 500 fs laser pulses with our lowest ( $F_{abs} = 0.072 \text{ mJ/cm}^2$ ) (a), and highest  $F_{abs} = 0.33 \text{ mJ/cm}^2$  (b), fluences absorbed. The energy initially deposited in the electrons creates a sharp peak in  $T_e$ . The phonons in contrast have a much larger heat capacity and therefore experience a smaller temperature rise. Since  $T_e$  is modulated much more than  $T_l$ ,  $T_e$  is more sensitive to changes in fluence.

yields a  $1/e$  penetration depth of  $\sim 100\text{nm}$  at  $2\text{ ps}$ . The shape of the temperature variation therefore has a depth to the width ratio of  $\sim 10^{-3}$  which confirms the validity of our 1 dimensional treatment.

The adsorbate excitation and temperature profiles are calculated by convoluting a response function with  $T_e$  and  $T_l$  profiles. Errors in the substrate temperatures will lead to errors in our estimated adsorbate-substrate coupling rates. The accuracy of the parameters used in this problem therefore need to be considered. Our analysis is most susceptible to changes in  $G$ . A deviation in  $\kappa_e$  changes the effective penetration depth of the visible heat source but does not greatly change the over all shape of the curves. A change of the electron-phonon coupling constant  $G$ , however, proportionally changes the decay rate of the electron temperature and thus produces an error in the determination of the coupling rates of the adsorbate to these reservoirs. These effects are described with greater detail later in Chapter 6.

## Chapter 4

### Femtosecond Infrared Spectroscopy

Ultrafast laser pulses that are shorter than the vibrational dephasing times of condensed phase systems are quite common. For example, spectral linewidths of vibrational transitions in the steady state are usually narrower than  $\sim 20\text{cm}^{-1}$  corresponding to dephasing times longer than 500 fs. If vibrational states are caused to undergo changes on timescales less than 500 fs, it is evident that the interplay between the vibrational dephasing and the dynamical processes of interest must be considered as part of the interpretation of the experiment. In the particular case of CO on Cu(111) the free induction decay time, as measured by sum frequency generation (Ref. [59]), is  $T_2 = 2.2\text{ ps}$ . This section addresses some issues related to the probing of perturbed vibrational transitions using ultrashort pulses. There are a variety of possible approaches to obtaining transient IR spectra and the experimental manifestations of the vibrational dephasing are dependent on the method used. Two extreme approaches used in the study of IR transients are the conventional pump/probe method

(see for example Ref. [16, 17]), which uses short light pulses to pump and probe the sample, and the gated quasi-CW method (see for example Ref. [60, 61]) which uses ultrafast gated IR detection. These approaches generally yield different signals from the same sample so that a comparison of the advantages and disadvantages of each of them is worthwhile.

#### 4.1 Modulation of the complex frequency in a two level system

The simplest approach to calculating time-dependent vibrational spectra is to solve the damped Liouville equations (Bloch equations) for a two level system with Hamiltonian:

$$\mathcal{H} = \mathcal{H}_0 + S(t) + V(t) \quad (4.1)$$

where  $\mathcal{H}_0$  is a two level system with Bohr frequency  $\omega_{10} = \omega_1 - \omega_0$  which in the present case will be a vibrational frequency.  $S(t)$  is a time dependent perturbation such as a first order Stark effect that will usually be slowly acting compared with  $V(t)$ .  $V(t)$  represents the interaction of the two level system with an electromagnetic field  $\vec{E}(t)$ : i.e.  $V(t) = -\vec{\mu}_{01} \bullet \vec{E}(t)$ , where the field magnitude is  $\vec{E}(t) = \hat{e}E(t) = \hat{e}\mathcal{E}(t)\cos(\omega_L t)$ . For the experiments at hand the frequency shifts will be caused by the amplitude variations of a coupled low frequency oscillator as described in the previous section. The system is considered to be in contact with thermal reservoirs and the relaxation processes are as described in chapter 2.

The Liouville equation for the off-diagonal elements of the density matrix in the representation of  $\mathcal{H}_0$  or  $\mathcal{H}_0 + S(t)$  is written with a time dependent dephasing rate  $\Gamma(t)$  as follows:

$$\dot{\rho}_{01} = \frac{i}{\hbar}[\rho, \mathcal{H}]_{01} - \Gamma(t)\rho_{01} \quad (4.2)$$

$$= \frac{i}{\hbar}\{(\rho_{00} - \rho_{11})\mathcal{H}_{01} + (\mathcal{H}_{11} - \mathcal{H}_{00})\rho_{01}\} - \Gamma(t)\rho_{01} \quad (4.3)$$

$$= \frac{i}{\hbar}(\rho_{00} - \rho_{11})\mu_{01}E(t) - (i\omega_{01}(t) + \Gamma(t))\rho_{01} \quad (4.4)$$

For weak probe fields most of the population will reside in the ground state and we can assume that  $n_0 = \rho_{00} - \rho_{11}$  remains constant. Situations in which the population is modulated by the pump pulse will be addressed later in section 4.2.1. Integration of equation 4.4 (see appendix 9.2) yields:

$$e^{-i\omega_L t}\rho_{01}(t) = -\frac{i\mu_{01}n_0}{\hbar} \int_{-\infty}^t dt_1 E(t_1) e^{-\int_{t_1}^t d\tau (i\omega_{01}(\tau) + \Gamma(\tau))}, \quad (4.5)$$

where  $\omega_{01}(\tau) = \omega_{01} + \frac{1}{\hbar}[S_{00}(\tau) - S_{11}(\tau)]$  represents the frequency modulated by the time-dependent Stark shift. The dephasing parameter  $\Gamma(\tau) = \gamma_0 + \gamma(\tau)$  has a time-dependent part  $\gamma(\tau)$ , to account for any changes brought about by the baths to which the system is coupled, and a time-independent component  $\gamma_0$ .

The two experimental approaches considered are the gated quasi-CW probe pulse (see Fig. 4.1a) and the filtered short probe pulse (see Fig. 4.1b). These two methods can be explored by taking the short and long pulse limits of a Gaussian pulse expression for the probe IR pulse. A Gaussian probe pulse with pulse duration  $\tau_p = \sqrt{\frac{2\ln 2}{a}}$ ,

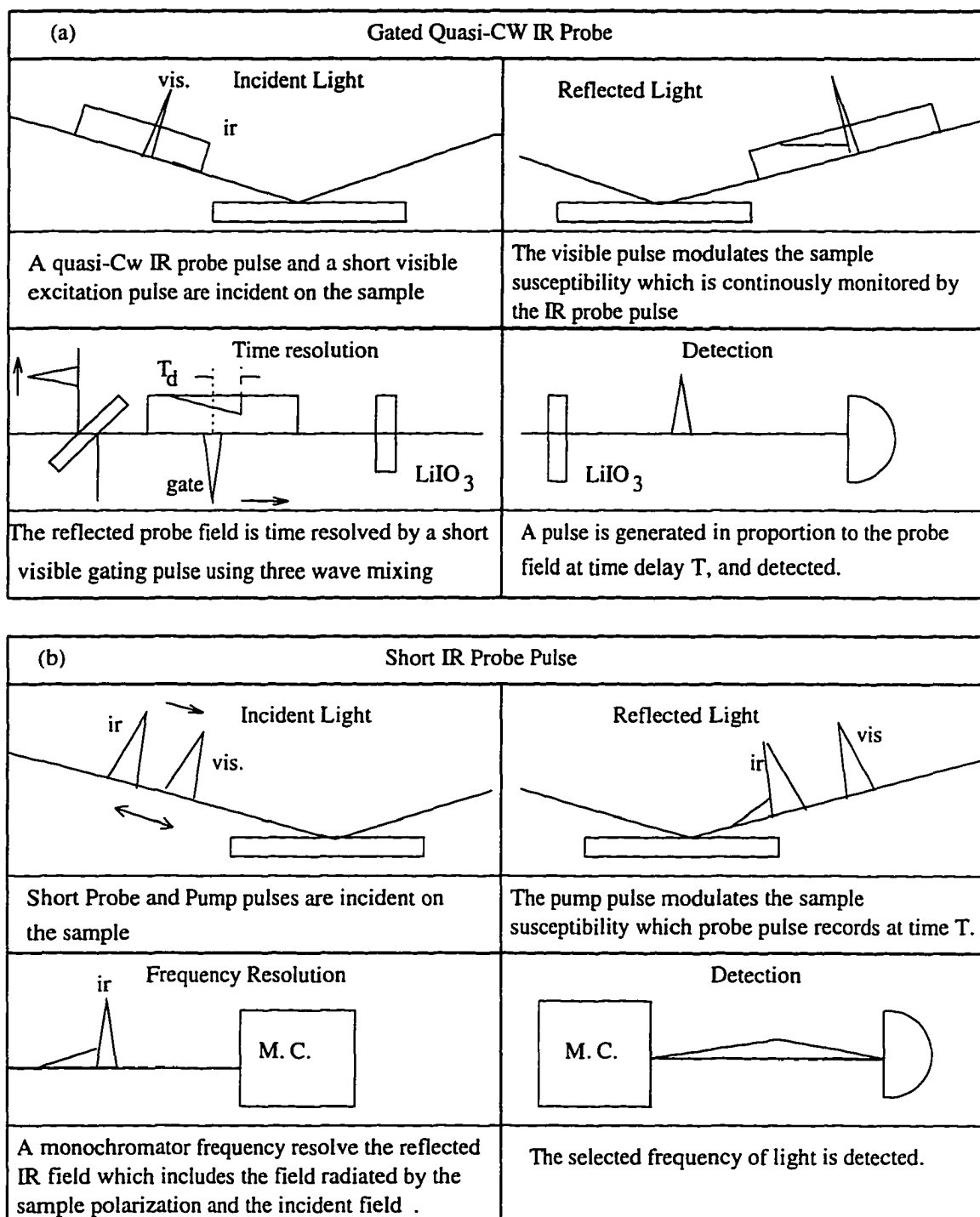


Figure 4.1: Schematic of two time-resolved IR probe methods.

and shape  $E(t) = \mathcal{E}_0 e^{-a(t-t_{pr})^2 + i\omega_i(t-t_{pr})}$ , substituted into equation (4.5) will generate the following polarization;

$$e^{-i\omega_i(t-t_{pr})} \rho_{01}(t) = \frac{i\mu_{01}n_0\mathcal{E}_0}{\hbar} \int_{-\infty}^t dt_1 e^{-a(t_1-t_{pr})^2} e^{-\int_{t_1}^t d\tau \Omega_{01}(\tau)}. \quad (4.6)$$

where  $\Omega_{01}(\tau) = i(\omega_{01}(\tau) + \omega_L) + \Gamma(\tau)$ . We now compare two different experimental approaches to measuring  $\rho_{01}(t)$  or its spectra. We defer the inclusion of substrate effects to appendix (9.1) and consider here a sample probed in *transmission*.

When short probe pulses are employed in the experiment, the envelope  $\mathcal{E}(t)$  is finite and usually has a duration shorter than the dynamics of interest. On the other hand, with the gating technique the IR field is quasi-monochromatic and  $\mathcal{E}(t) = \mathcal{E}_0$  is effectively a constant over the time scale of the experiment. As can be seen from the exponentials inside the integral (Eq. 4.6) the detuning frequency  $\Delta_{01} = \omega_{01} + \omega_L$  and the decay time,  $\Gamma(\tau)$ , are the physical constants which define the relevant time scales. While typical experimental values of the pulse duration and  $|\Omega_{01}|$ , may not provide for completely separated timescales, to illustrate the basic nature of the two approaches, we study solutions in the limits  $\sqrt{a} \gg |\Omega_{01}|$  and  $\sqrt{a} \ll |\Omega_{01}|$ .

### Gated quasi-CW probe

For the gated quasi-CW probe, we assume  $\sqrt{a} \ll |\Omega_{01}|$  (i.e. long pulse limit). In this limit the polarization can be written

$$e^{-i\omega_i(t-t_{pr})} \rho_{01}(t) = \frac{i\mu_{01}n_0\mathcal{E}_0}{\hbar} \int_{-\infty}^t dt_1 e^{-\int_{t_1}^t d\tau \Omega_{01}(\tau)} \quad (4.7)$$

The resulting quasi-CW infrared beam is gated by up- or down- conversion in a nonlinear crystal after the sample by mixing with a short pulse having field envelope  $\mathcal{E}_{gate}(t - t_g)$  centered at the gating time or delay time,  $t_g$ . If the signal is small, the current in the square law photodetector is proportional to :

$$\langle \mathcal{E}_{gate}^2(t - t_g)[\mathcal{E}_0 + \mathcal{E}_{gen}(t)]^2 \rangle \quad (4.8)$$

where  $\mathcal{E}_{gen}(t)$  (to be distinguished from the complex  $E_{ads}$  which explicitly accounts for the reflection geometry) is the in-phase part of the IR field generated at time  $t$  by the polarization derived from  $\rho(t)$  given in equation (4.7). The angle brackets denote time average. Note that if the gating pulse is very short compared with the relevant dynamics, and if the signal is small then the detected light intensity is given approximately by:

$$I_{ir}(t_g) \propto \mathcal{E}_0^2 + 2\mathcal{E}_0\mathcal{E}_{gen}(t_g). \quad (4.9)$$

The relevant part of the generated field is  $\mathcal{I}m\{P(t)e^{-i\omega_L t}\}$  which is obtained from (4.5) using  $P = Tr\{\boldsymbol{\mu}\boldsymbol{\rho}\}$  with  $t = t_g$ . For the CW method the field is, apart from constants,

$$\mathcal{E}_{gen}(t_g) = \mathcal{I}m\left\{i \int_{-\infty}^{t_g} dt_1 e^{-\int_{t_1}^{t_g} \Omega_{01}(\tau) d\tau}\right\}. \quad (4.10)$$

In general we are interested in the differential change in absorption with and without the pump, so the signal,  $S(t)$ , is;

$$S(t) = \frac{I_{pumped}}{I_0} - \frac{I_{unpumped}}{I_0} \quad (4.11)$$

$$= -2\text{Re}\left\{\frac{\mathcal{E}_{gen}(t) - \mathcal{E}_{gen}^0}{\mathcal{E}_0}\right\} \quad (4.12)$$

$$\approx \text{Re}\left\{\int_{-\infty}^{t_g} dt_1 e^{-\int_{t_1}^{t_g} \Omega_{01}(\tau) d\tau} - \frac{1}{\Omega_{01}^0}\right\}. \quad (4.13)$$

Where  $\mathcal{E}_{gen}^0$  and  $\Omega_{01}^0$  are for the unpumped case.

### Short Pulse Probe

The situation for a short pulse probe signal is qualitatively different from (4.10). The relevant part of the field is obtained from (4.5) using explicit form for  $\mathcal{E}(t)$ . Assuming that the pulse is Gaussian and much shorter than the modulations in the IR response, ( $\sqrt{a} \gg |\Omega_{01}|$ ), we can write the generated field for time  $t > t_{pr}$ :

$$E_{gen}(t, t_{pr}) \sim \mathcal{E}_0 \sqrt{\frac{\pi}{a}} e^{-\int_{t_{pr}}^t d\tau (i\omega_{01}(\tau) + \gamma(\tau))} \quad (4.14)$$

With a filter in front of the detector enabling only the frequencies near  $\omega_F$  to be measured, the signal current is equal to the product of the Fourier transforms of the probe and generated fields at  $\omega_F$ . In other words, the spectrum of the generated field is given by its Fourier transform. This can be expressed using a detuning frequency,  $\Omega_{01}^F(t) = i(\omega_{01}(t) + \omega_F) + \Gamma(t)$  between the oscillator and the filter.

$$\mathcal{E}_{gen}(\omega_F, t_{pr}) = \int_{-\infty}^{\infty} dt_1 E_{gen}(t_1) e^{-i\omega_F t_1} \quad (4.15)$$

$$= \mathcal{E}_0 \sqrt{\frac{\pi}{a}} \int_{t_{pr}}^{\infty} dt_1 e^{-\int_{t_{pr}}^{t_1} d\tau (\Omega_{01}^F(\tau))} \quad (4.16)$$

The short probe pulse signal, apart from constants, is thus given by:

$$I(\omega_F, t_{pr}) = |\mathcal{E}(\omega_F)|^2 - 2\text{Re}\{\mathcal{E}_{gen}(\omega_F, t_{pr})\mathcal{E}(\omega_F)\}. \quad (4.17)$$

Again using unpumped measurements as a reference, the signal ( $S(t)$ ) obtained is;

$$S(t) = \frac{I_{pumped}}{I_0} - \frac{I_{unpumped}}{I_0} \quad (4.18)$$

$$= 2Re\left\{\frac{\mathcal{E}_{gen}(\omega_F, t_{pr}) - \mathcal{E}_{gen}^0(\omega_F)}{\mathcal{E}_0(\omega_F)}\right\} \quad (4.19)$$

$$\approx Re\left\{\int_{t_{pr}}^{\infty} dt_1 e^{-\int_{t_{pr}}^{t_1} d\tau(\Omega_{01}^F(\tau))} - \frac{1}{\Omega_{01}^F}\right\} \quad (4.20)$$

## 4.2 Model of an Impulsive Complex Frequency Shift

These signals described in the previous section can be easily calculated numerically for arbitrary pulses and functions  $S(t)$  and  $\Gamma(t)$ , but the basic properties and limitations for time domain experiments are more clearly exposed by considering  $\delta$ -function pump pulses resulting in step function changes in  $\Omega_{01}$ . We suppose here that the CO resonance has a width  $\Gamma_a$  and detuning  $\Delta_{10}^a$  before  $t=0$ , and width  $\Gamma_b$  and detuning  $\Delta_{10}^b$  immediately after  $t=0$ . “Immediately” in this context means faster than could be measured. Delta function light pulses are used here to simplify the mathematics but without loss of the significant physics.

The quasi-CW method yields a spectrum of the form given by equation (4.13). With the conditions of  $\delta$ -function pump and gating pulses, separated by  $\tau_d = t_g - t_{pump}$ , the differential reflectivity signal in the CW experiment is readily obtained from equation (4.10):

$$\tau_d < 0; \quad S = 0 \quad (4.21)$$

$$\tau_d > 0; \quad S = \text{Re}\left\{\left(\frac{1}{\Omega_b} - \frac{1}{\Omega_a}\right)[1 - e^{-\Omega_b \tau_d}]\right\} \quad (4.22)$$

where  $\Omega_a = i\Delta_{01}^a + \Gamma_a$  and  $\Omega_b = i\Delta_{01}^b + \Gamma_b$  are the complex frequencies before and after heating the electrons. Equation (4.22) determines how quickly the new signal can be observed and how suddenly the original absorbance characterized by  $\Omega_a$  can disappear as a result of a change in the complex frequency. Notice that the dynamics are determined by the *new* complex frequency.

On the other hand the short probe pulse method is described by equation (4.20). With  $\tau_d = t_{pr} - t_{pump}$  and the selection of a frequency initially detuned by complex frequency  $\Omega_a^F$  from resonance the short probe pulse yields a signal intensity as follows:

$$\tau_d < 0; \quad S = \text{Re}\left\{\left(\frac{1}{\Omega_b^F} - \frac{1}{\Omega_a^F}\right)e^{\Omega_a^F \tau_d}\right\} \quad (4.23)$$

$$\tau_d > 0; \quad S = \text{Re}\left\{\left(\frac{1}{\Omega_b^F} - \frac{1}{\Omega_a^F}\right)\right\} \quad (4.24)$$

Interestingly the  $\tau_d < 0$  term of equation (4.23), and hence *dynamics* of these signals, always grows in with time constant determined by the *unperturbed* resonance frequency  $\Omega_a^F$  and the peak signal occurs at zero delay of pump and probe pulses.

The significant differences between the gated quasi-CW probe (Eq. 4.13 and 4.22) and the short pulse probe (Eq. 4.20 and 4.24) are most readily understood by examining the integrals involved. The time ordering of the integrals can be depicted by diagrams representing these processes as shown in Fig. 4.2. For each diagram the horizontal line is a time axis. The probe fields initially interact with the sample where the solid

## (a) Gated Quasi-CW Probe

$$= \text{Im}\left\{i \int_{-\infty}^{t_g} dt' e^{-\int_{t'}^{t_g} \Omega_a(\tau) d\tau}\right\}$$

$$= \text{Im}\left\{i \int_{-\infty}^{t_p} dt' e^{-\int_{t'}^{t_p} \Omega_a(\tau) d\tau - \int_{t_p}^{t_g} \Omega_b(\tau) d\tau}\right\}$$

$$= \text{Im}\left\{i \int_{t_p}^{t_g} dt' e^{-\int_{t'}^{t_g} \Omega_b(\tau) d\tau}\right\}$$

## (b) Short Pulse Probe

$$= \text{Im}\left\{i \int_{t_{pr}}^{t_p} dt' e^{-\int_{t'}^{t_p} \Omega_a(\tau) d\tau}\right\}$$

$$= \text{Im}\left\{i \int_{t_p}^{\infty} dt' e^{-\int_{t'}^{t_p} \Omega_a(\tau) d\tau - \int_{t_p}^{t'} \Omega_b(\tau) d\tau}\right\}$$

$$= \text{Im}\left\{i \int_{t_{pr}}^{\infty} dt' e^{-\int_{t'}^{t'} \Omega_b(\tau) d\tau}\right\}$$

Figure 4.2: Time ordering of the integrals for the impulsive perturbation model.  $t'$  is the integration variable and  $t_p$  is the arrival time of the pump-pulse. (a) Quasi-CW method: The delay time,  $T_d$ , is measured between the pump-pulse, and  $t_g$  the time at which the gate pulse upconverts the IR probe. (b) Short Pulse Probe method: The delay time is measured between the pump-pulse and  $t_{pr}$ , the time at which the IR probe pulse impinges upon the sample.

arrows point onto the line. The field is reradiated when the squiggly arrows leave. In the integrals for the quasi-CW case the field interacts with the sample at time  $t'$  and is reradiated at time  $t_g$ . For the short duration probe case the field initially interacts at time  $t_{pr}$  and is reradiated at time  $t'$ . The pump arrow indicates the time at which the complex frequency is shifted from  $\Omega_a$  to  $\Omega_b$ .

For both methods the evaluation of the integrals with delta function probe and gating pulses requires consideration of three regions; in regions 1 the probe field couples and is reradiated before the pump, in regions 2 the probe field couples before the pump and is reradiated after the pump and in regions 3 the probe field is coupled and reradiated after the pump. In the quasi-CW case the integral only extends up to the gating time. In the short pulse probe experiment the detector senses the free induction decay (FID) radiated starting from the arrival time of the probe ( $t_{pr}$ ) up to infinity. Diagrams 4.2a.2 and 4.2b.2 correspond to the FID of the unpumped sample being perturbed by the pump at  $t_p$ . In the short pulse probe case the system propagates with complex frequency  $\Omega_a$  from  $t_{pr}$  to  $t_p$  and with complex frequency  $\Omega_b$  from  $t_p$  to  $t'$  and the detector response results in an integration over  $t'$ . With the quasi-CW method the system propagates with complex frequency  $\Omega_a$  from  $t'$  to  $t_p$  and with complex frequency  $\Omega_b$  from  $t_p$  to  $t_g$ . The total field reradiated at time  $t_g$  involves an integration over  $t'$ .

Consider some qualitative features of the two approaches. The short pulse probe

signal evolution is always shaped initially by the unpumped vibrational properties in  $\Omega_a^F$ . On the contrary the time dependence of the quasi-CW signal is determined by  $\Omega_b$ . Fig. 4.3a shows the signals expected for the case where the absorption width is suddenly increased. The only effect this increase has on the short pulse probe signal is on its amplitude at zero delay. On the other hand the gated CW method yields a signal growth kinetics that depends on the amount of line broadening that occurred. In the second example the perturbation causes an instantaneous line shift which is small compared to the linewidth and the linewidth remains constant Fig. 4.3. Again the short pulse probe signal (bleach) grows up to zero delay in accordance with  $e^{\Gamma_a \tau_d}$  and is constant thereafter at a level determined by the magnitude of the frequency shift. The gated-CW method provides a similar signal only it grows after time zero. Both signals grow in with similar response times. In this case the information about the line shifting comes purely from the magnitude of the signal and can be similarly obtained from either approach.

The responses to a large frequency shift are shown in Fig. 4.3c. The short pulse measurement shows similar dynamics to the small frequency shift. A quite different response is exhibited by the quasi-CW method in which damped oscillations with period corresponding to the frequency mismatch are seen. If this shift is sufficiently large so that the time resolution is insufficient to isolate the beats or if the sample is sufficiently inhomogeneous, then an instantaneous change in absorbance will

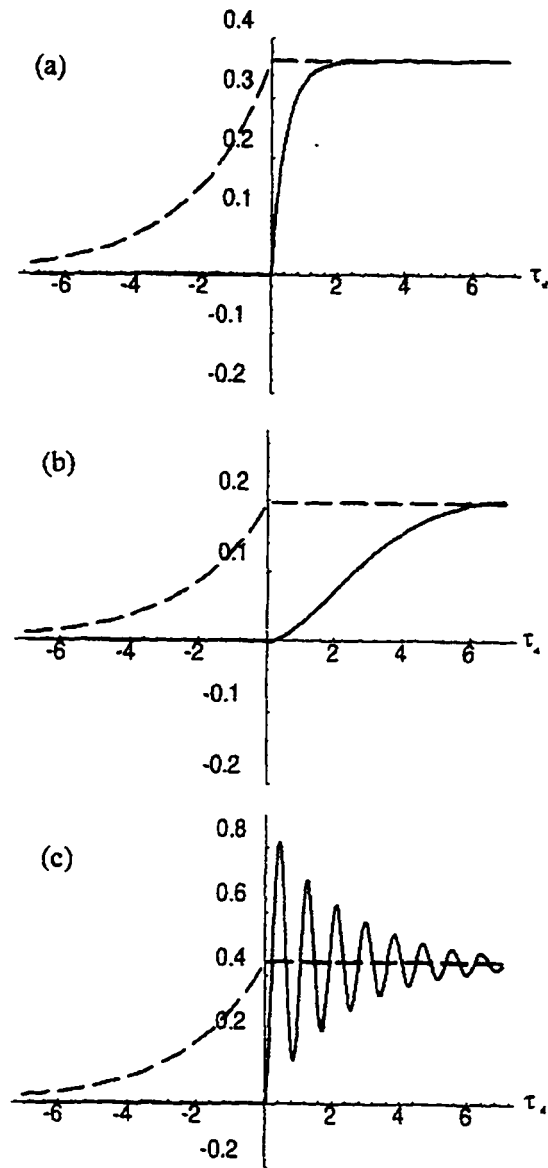


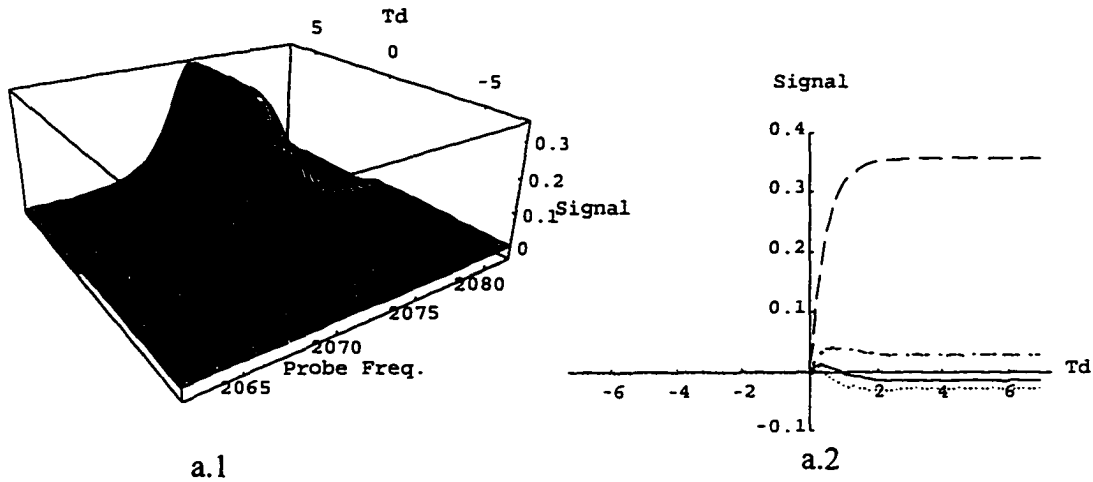
Figure 4.3: Simulations of an impulsive frequency response for three different complex frequency shifts. For the gated CW method (dashed) the laser frequency is at  $2075 \text{ cm}^{-1}$ . For the short probe pulse method the filter frequency is at  $2075 \text{ cm}^{-1}$ . (a) Increase in line width,  $\Gamma_a = 2.25 \text{ cm}^{-1}$ ,  $\Gamma_b = 12.25 \text{ cm}^{-1}$ , and  $\omega_{01}^a = \omega_{01}^b = 2074$ ; (b) center frequency shift of  $\sim 50\%$  the linewidth  $\Gamma_a = \Gamma_b = 2.25 \text{ cm}^{-1}$ ,  $\omega_{01}^a = 2074 \text{ cm}^{-1}$ , and  $\omega_{01}^b = 2072 \text{ cm}^{-1}$ ; (c) center frequency shift of  $\sim 5x$  the linewidth  $\Gamma_a = \Gamma_b = 2.25 \text{ cm}^{-1}$ ,  $\omega_{01}^a = 2074 \text{ cm}^{-1}$ , and  $\omega_{01}^b = 2001 \text{ cm}^{-1}$ .

be sensed. An example of this effect was observed in the experiment on the photodissociation of carbon monoxide from an iron carbonyl [62]. On dissociation, the resonance frequency shifts in about 50 fs from  $1951\text{ cm}^{-1}$  to  $2135\text{ cm}^{-1}$  without much change in width. This shift of  $184\text{ cm}^{-1}$  corresponds to a beat period of 180 fs which could not have been resolved in that experiment so an "instantaneous" bleach signal is observed. Any changes of integrated absorption cross section that occur as a result of the perturbation must also be included in the evaluation of the responses. These appear in much the same way as the population changes in equation (4.5). This is an example where the population kinetics give a reasonable interpretation of spectral changes. Simulations of the same three complex frequency shifts but with a range of probe frequencies are depicted in figures 4.4, 4.5 and 4.6.

The comparison shows the advantage of the quasi-CW method when the experimental objective is to study the change in position or width of an existing absorption without population changes: the kinetics of the change can be observed without direct interference from the free induction decay of the existing absorption. For example if an absorption band is instantaneously bleached, perhaps by a photochemical reaction that removes the species, the observed response is immediate. On the other hand, the short pulse probe method has a clear advantage when the signal is a new absorption introduced by the pumping process. The short pulse probe technique is capable of tracking processes much faster than the equilibrium dephasing times when there is no

Increased line width ( $\Gamma_b = 5 * \Gamma_a$ )

## Gated CW Probe



## Short pulse probe

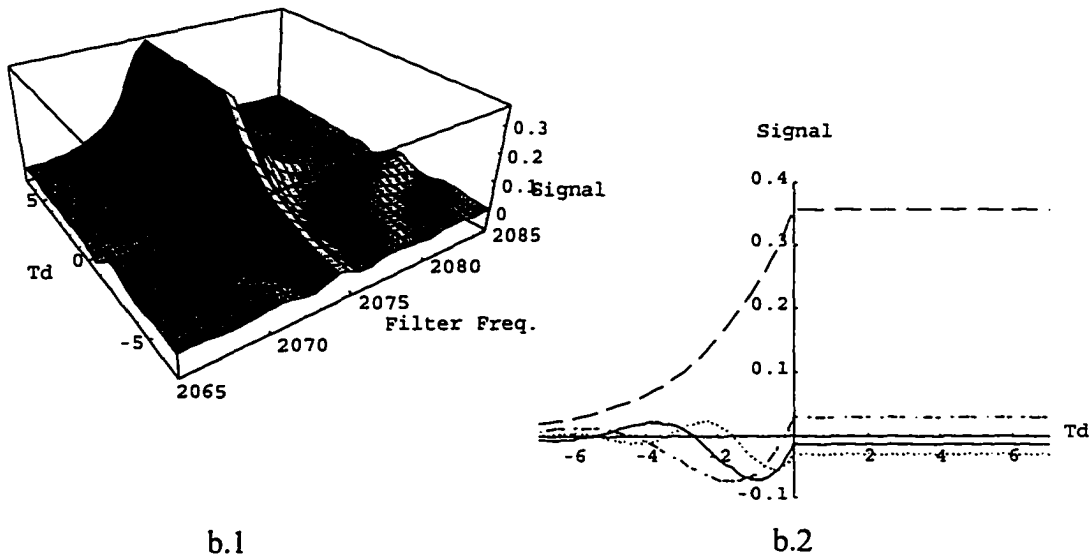
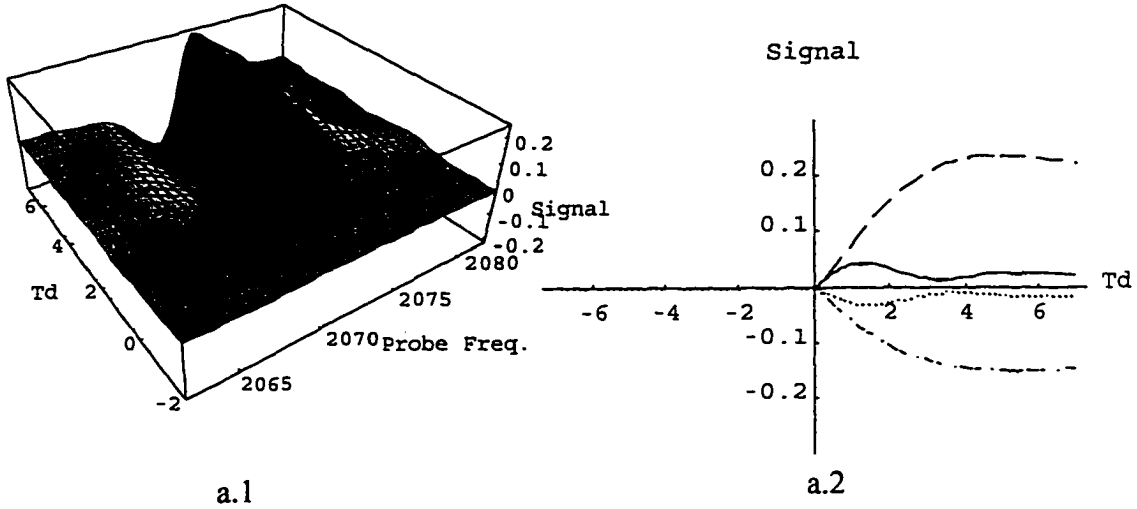


Figure 4.4: Simulations of an impulsive frequency response for a linebroadening of a factor of 5.  $\Gamma_a = 4.5$  and  $\Gamma_b = 22.5 \text{cm}^{-1}$ ,  $\omega_{01}^a = \omega_{01}^b = 2074 \text{cm}^{-1}$ ; (a.1) and (a.2) are for the gated CW probe measurement. (b.1) and (b.2) are for the short probe pulse. The lines in (a.2) and (b.2) are for the probe frequencies 2065  $\text{cm}^{-1}$ - dotted, 2070  $\text{cm}^{-1}$ - dotted and dashed, 2074  $\text{cm}^{-1}$ - dashed, 2080  $\text{cm}^{-1}$ - solid.

Small Frequency Shift ( $\delta\omega_{01}=\Gamma/2$ )

## Gated CW Probe



## Short pulse probe

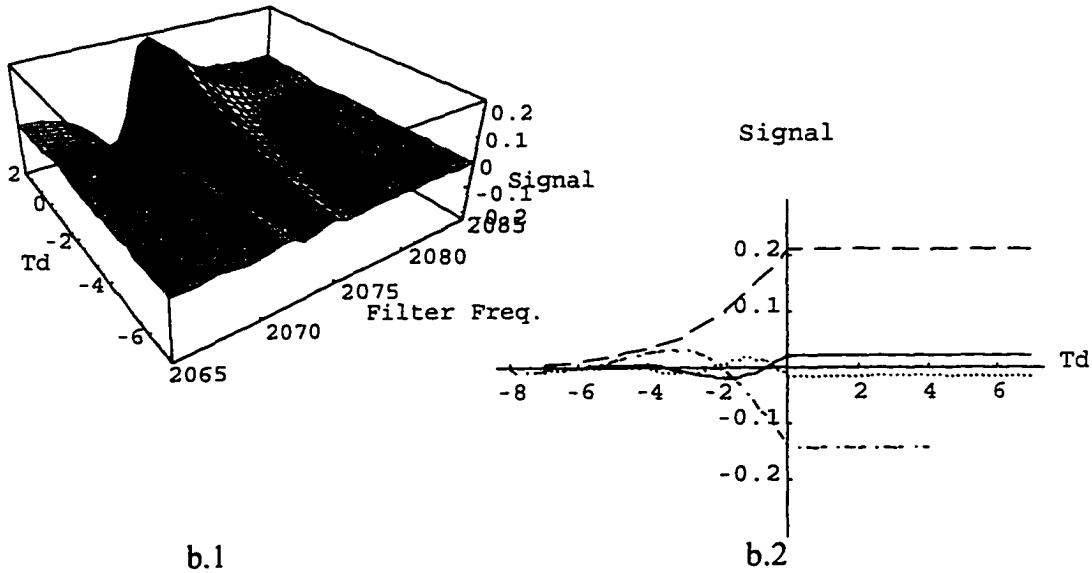


Figure 4.5: Simulations of an impulsive frequency response for a center frequency shift of about 50% the linewidth  $\Gamma_a = \Gamma_b = 2.25\text{cm}^{-1}$ ,  $\omega_{01}^a = 2074\text{cm}^{-1}$  and  $\omega_{01}^b = 2072\text{cm}^{-1}$ ; (a.1) and (a.2) are for the gated CW probe measurement. (b.1) and (b.2) are for the short probe pulse. The lines in (a.2) and (b.2) are for the probe frequencies 2065cm<sup>-1</sup>- dotted, 2070cm<sup>-1</sup>- dotted and dashed, 2075cm<sup>-1</sup>- dashed, 2080cm<sup>-1</sup>- solid.

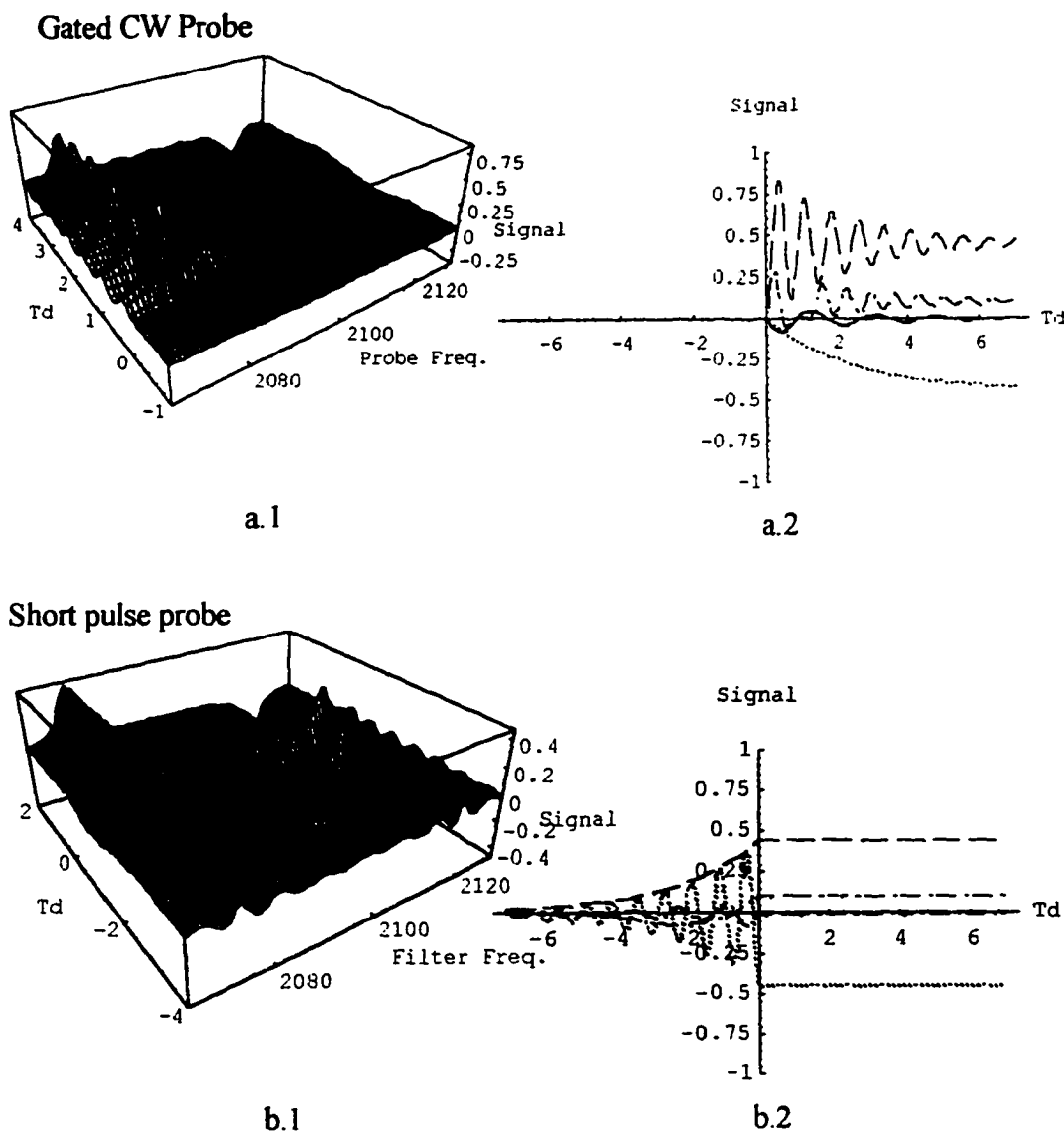
Large Frequency Shift (  $\delta\omega_{01}=10*\Gamma$  )

Figure 4.6: Simulations of an impulsive frequency response for a center frequency shift of 10 times the linewidth  $\Gamma_a = \Gamma_b = 2.25\text{cm}^{-1}$ ,  $\omega_{01}^a = 2074\text{cm}^{-1}$  and  $\omega_{01}^b = 2119\text{cm}^{-1}$ ; (a.1) and (a.2) are for the gated CW probe measurement. (b.1) and (b.2) are for the short probe pulse. The lines in (a.2) and (b.2) are for the probe frequencies  $2119\text{cm}^{-1}$ -dotted,  $2070\text{cm}^{-1}$ -dotted and dashed,  $2074\text{cm}^{-1}$ -dashed,  $2100\text{cm}^{-1}$ -solid.

requirement to single out a particular frequency, i.e. when no filter or monochromator is placed in front of the detector. Consider a transition having a typical vibrational width of  $10\text{ cm}^{-1}$  that is shifted by  $100\text{ cm}^{-1}$ , but whose stationary width is unchanged as a result of a pumping process. If the shift is essentially immediate the signal at the new frequency grows in with time constant  $T_2 = 2.2\text{ ps}$  if a filter is placed in front of the detector. However, without the filter and detecting all the frequency components, the signal will track the profile of the probe pulse. At times much less than the dephasing time the field corresponding to the new transition is distributed over a broader frequency region, but the probe pulse itself is by definition spectrally broad enough to detect the whole absorption on the timescale of the pulsewidth.

#### 4.2.1 Desorption

One other pump pulse effect is considered here as extensions of the previous treatment of pump induced complex frequency shifts. The discussion will focus only on the gated quasi-CW probe method. The removal of a diatomic molecule from a surface will alter its vibrational potential and hence oscillation frequency. Since the frequency shift is much greater than the linewidth, the detuning oscillations are averaged by the gating or short probe pulse. Desorption can therefore be considered to remove the sample molecules from the laser probe and is modeled here by a pumping function  $A(t)$ . Using a two level density matrix model for the stretch vibration of a diatomic molecule one

obtains;

$$\dot{\rho}_{01}(t) = \frac{i}{\hbar} \rho_{00} V_0(t) - \Omega_{01}(t) \rho_{01}(t) - A(t) \rho_{01}(t) \quad (4.25)$$

$$\dot{\rho}_{00}(t) = -A(t) \rho_{00}(t) \quad (4.26)$$

$$\dot{\rho}_{11}(t) = -A(t) \rho_{11}(t) \quad (4.27)$$

The polarization can be obtained by integrating these equations to yield the following:

$$\rho_{01}(t) = \frac{i}{\hbar} V_0 \int_{-\infty}^t dt_1 \rho_{00}(t_1) e^{-\int_{t_1}^t A(\tau) d\tau - \int_{t_1}^t \Omega_{01}(\tau) d\tau} \quad (4.28)$$

Substituting in the time dependence of  $\rho_{00}(t) = \rho_{00}(t_1) e^{-\int_{t_1}^t A(\tau) d\tau}$  into the previous equation brings the ground state population out in front of the integral,

$$\rho_{01}(t) = \frac{i}{\hbar} V_0 \rho_{00}(t) \int_{-\infty}^t dt_1 e^{-\int_{t_1}^t \Omega_{01}(\tau) d\tau}. \quad (4.29)$$

This indicates that the population changes due to desorption will show up instantaneously.

## Chapter 5

### Experimental Description

#### 5.1 Basic plan of experiments

The experiment incorporates ultrafast visible, and tunable IR pulses with ultrahigh vacuum (UHV) technologies. The substrate is heated with a short visible light pulse (0.3-1.5 ps) and the adsorbate response is monitored using time resolved infrared spectroscopy (see the schematic in Fig. 4.1). The IR probe used is a quasi-CW infrared pulse (30 ps) tunable from  $\sim 1925$  to  $2175 \text{ cm}^{-1}$ . The reflected IR field intensity records the adsorbate susceptibility and is time-resolved by upconversion in a nonlinear crystal using an ultrafast ( $\sim 500 \text{ fs}$ ) visible gating pulse.

The pulse duration necessary to separate electronic and surface temperatures varies from metal to metal according to the physical parameters discussed in chapter 3. For platinum which has a relatively fast electron-phonon equilibration time, a 1ps pulse will create a temperature difference ratio between the electrons and the phonons of  $\frac{\delta T_e}{\delta T_l} = 2$  (see Ref. [14]). Experiments have shown that such a ratio is not

significant enough to establish the separate coupling rates between the adsorbate and the two substrate temperature reservoirs. However for copper the same pulse will generate a sufficient temperature difference ratio of  $\frac{\delta T_c}{\delta T_s} = 20$ . For metal substrates with electron-phonon coupling rates like Pt, the pulse will need to be closer to 100 fs.

The quasi-CW probe pulse is generated in a three wave mixing process with two visible pulses in a lithium iodate ( $\text{LiIO}_3$ ) crystal. The resulting IR pulses possess peak powers of  $\sim 1\text{kW}$  facilitating an efficient upconversion detection scheme which would not be feasible using a true CW IR source. In this chapter the UHV diagnostics and sample conditions will be reviewed and the laser system used will be described.

## 5.2 Vacuum system

The UHV chamber that houses the Cu(111) crystal sample utilizes a dual level cylindrical chamber design[59]. The upper level contains an ion gun and basic surface diagnostics including LEED, AUGER, and quadrupole mass spectrometry. The bottom level consists of a ring of view ports spaced by  $\sim 30^\circ$  that are used to carry out optical measurements with various incident angle geometries. By using  $\text{CaF}_2$  and quartz windows the accessible spectral region extends from  $5.5 \mu\text{m}$  to  $200\text{nm}$ . One set of ports separated by  $178^\circ$  provide glancing incident angles from  $82^\circ$  to  $90^\circ$ . By moving the incident beam over to the next port the angles  $65^\circ$  to  $79^\circ$  can be obtained.

Auger electron spectroscopy is used to examine the constituent atoms of a surface.

The particular model used, a Physical Electronics 255G double pass cylindrical mirror analyzer, provides an energy resolution of  $\Delta E/E = 0.6$ . The data was collected in a differential mode by modulating the analyzer voltage. The technique has a spectral range of 50-1500 eV and so the information is mostly about the core electron energy levels. Since the surface bonds involve the valence orbitals the spectra are not particularly sensitive to surface structure and yield information mainly about the relative concentrations of the atoms at the surface.

Low energy electron diffraction (LEED) is a useful technique with which to determine the surface structure. An incident low energy electron (10-100eV) is diffracted off the surface and detected with a biased phosphor coated screen, yielding a real time visibly observable diffraction pattern. A simple analysis records only the positions of the diffraction spots. This yields information about the symmetry of the surface and can be used to identify fairly simple over-layer structures and reconstructions. A more sophisticated analysis measures the spot intensity in addition to the spot position as a function of the incident beam voltage (dynamical LEED). When combined with theory this can provide more detailed information about the surface such as the distance between the 1st and 2nd layer atoms.

Besides laser spectroscopy which will be discussed below, the optical level of the chamber is also used for reflection absorption infrared spectroscopy (RAIRS). A Mattson 2020 Fourier Transform IR (FTIR) spectrometer is used with an external HgCdTe

detector as depicted in Fig. 5.1. Using silver mirrors and  $\text{CaF}_2$  optics and the FTIR broadband source light was redirected and focused on to the sample. To facilitate beam alignment, an IR/Vis beam combiner was used to incorporate a HeNe tracing beam. The resolution of the FTIR was  $2\text{ cm}^{-1}$ . The sensitivity was limited by drifts in the sample position, detector sensitivity, and ambient gas absorptions. All of these drifts altered the background absorption introducing spectral artifacts which could not be time averaged out. Under normal conditions a noise level of 0.3% could be maintained for an hour after taking a background scan.

Two sample holders were used. Most measurements were done with an  $\text{LN}_2$  cooled dewar sample holder. The sample was held by two tungsten filaments which provided resistive heating and a conduit for thermal cooling. The resulting temperature range was from 95 to 700 °K. Tilt and azimuthal rotation about the sample normal are built into the crystal holder assembly. The main dewar support provided the other axis of rotation about the cryostat arm and three axes of translation. Low temperature FTIR measurements were also made with a Kurt Lesker Helium cryostat sample holder. Only the main support axis of rotation and three axes translation were available with this sample holder. The cryostat cools the sample using a continuous flow of liquid helium that boils off on copper cooling block. The helium flow rate is  $\sim 2\text{L}$  of helium per hour. A leak in the helium transfer arm hindered the use of this sample holder. The leak caused oscillations with a period of  $\sim 2\text{ min}$  in the flow rate of the helium.

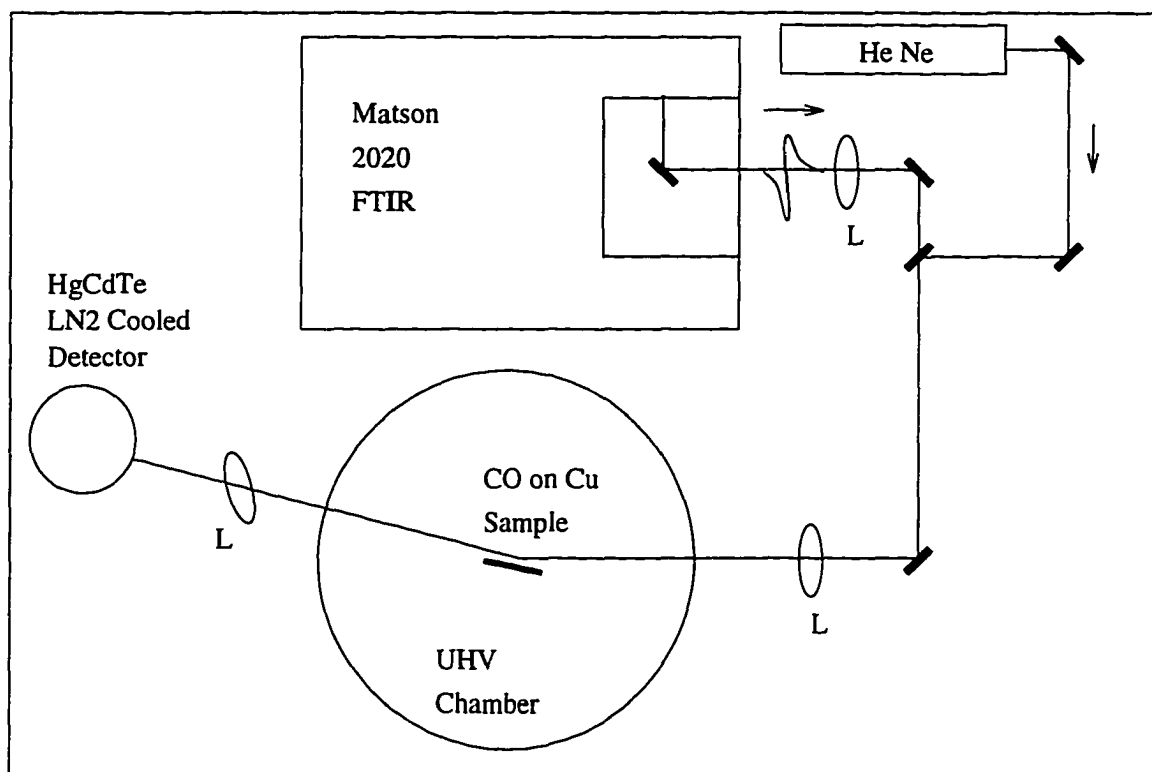


Figure 5.1: The broadband IR light exiting the FTIR interferometer is redirected into the UHV chamber using mirrors and  $\text{CaF}_2$  lenses. A He Ne laser beam is combined with the IR to facilitate alignment. After reflecting off the sample the light is detected with a HgCdTe detector.

This resulted in raising the lower temperature limit from the specified 35K to 55K and caused  $\sim 5K$  oscillations this base temperature.

The Cu(111) crystal, a 3/4" Dia. x 1/8" thick sample from Monocrystal was polished with successively smaller powders of alumina. The alumina powders of sizes 5, 1, 0.3 and 0.05  $\mu m$  were obtained from Buehler. The alumina was suspended in distilled water and dispersed on a rotating felt sanding disk. The main variable involved in the process was the polishing time for each alumina solution. These polishing times were determined by monitoring the degree of surface roughness visually. As polishing began with each powder solution a streaking pattern would develop with a grain proportional to the polish powder size. To avoid problems with sub-surface structural damage the polishing was continued three times longer than the time needed to establish the first streaking pattern with the new grain size. Rotating the sample by 90° between streaking patterns allowed for easier identification of new streaking patterns.

The final stages of sample preparation were conducted in UHV. A clean ordered Cu(111) surface was obtained by cycles of 500V Ar sputtering at 450C for 30 minutes, and flash annealing to 600 C. The level of carbon, the major surface contaminant, as determined by Auger, is kept at less than 3% of a monolayer. The surface order was established by observing a 1x1 LEED pattern and by CO absorption studies. After dosing with 3L of CO at 95 K and annealing to 125 K, subsequent cooling to

95 K produces an ordered overlayer with a  $(\sqrt{3} \times \sqrt{3})R30^\circ$  pattern (see Fig. 5.2) as confirmed by both LEED and FTIR linewidth measurements.

To facilitate overlapping the visible and IR beams a silicon wafer (1 cm x 2 cm ) was attached to the bottom of the sample holder with a simple tantalum foil holder. A visible pulse can excite electrons across the silicon band gap which produces transient metal like optical properties. Particularly near the Brewster angle, the  $\Delta R/R$  for far IR light ( $\sim 2000 \text{ cm}^{-1}$ ) can be very large. With our laser fluences we regularly obtained  $\Delta R/R$  signals of  $\sim 100\%$ . The silicon wafer (1cm x2cm) was aligned parallel to the Cu using the reflection of a HeNe beam. This arrangement permitted either the silicon or the Cu to be placed in the optical position by adjusting the vertical position of the crystal holder. Once the overlap of the visible and IR beams was established by monitoring the silicon signal, the sample holder was repositioned so the beams overlapped on the Cu.

### 5.3 Laser system

A schematic of the apparatus is shown in Fig. 5.3. At the heart of the laser system [21, 59, 61] is a mode-locked Nd:YLF master oscillator, which delivers pulses of 70 ps in duration at a 76 MHz repetition rate. These pulses are frequency doubled in a heated LBO crystal yielding 1.8 W of the 527 nm radiation. The unconverted light is used to synchronously pump two dye lasers, and 500 mW of the remaining

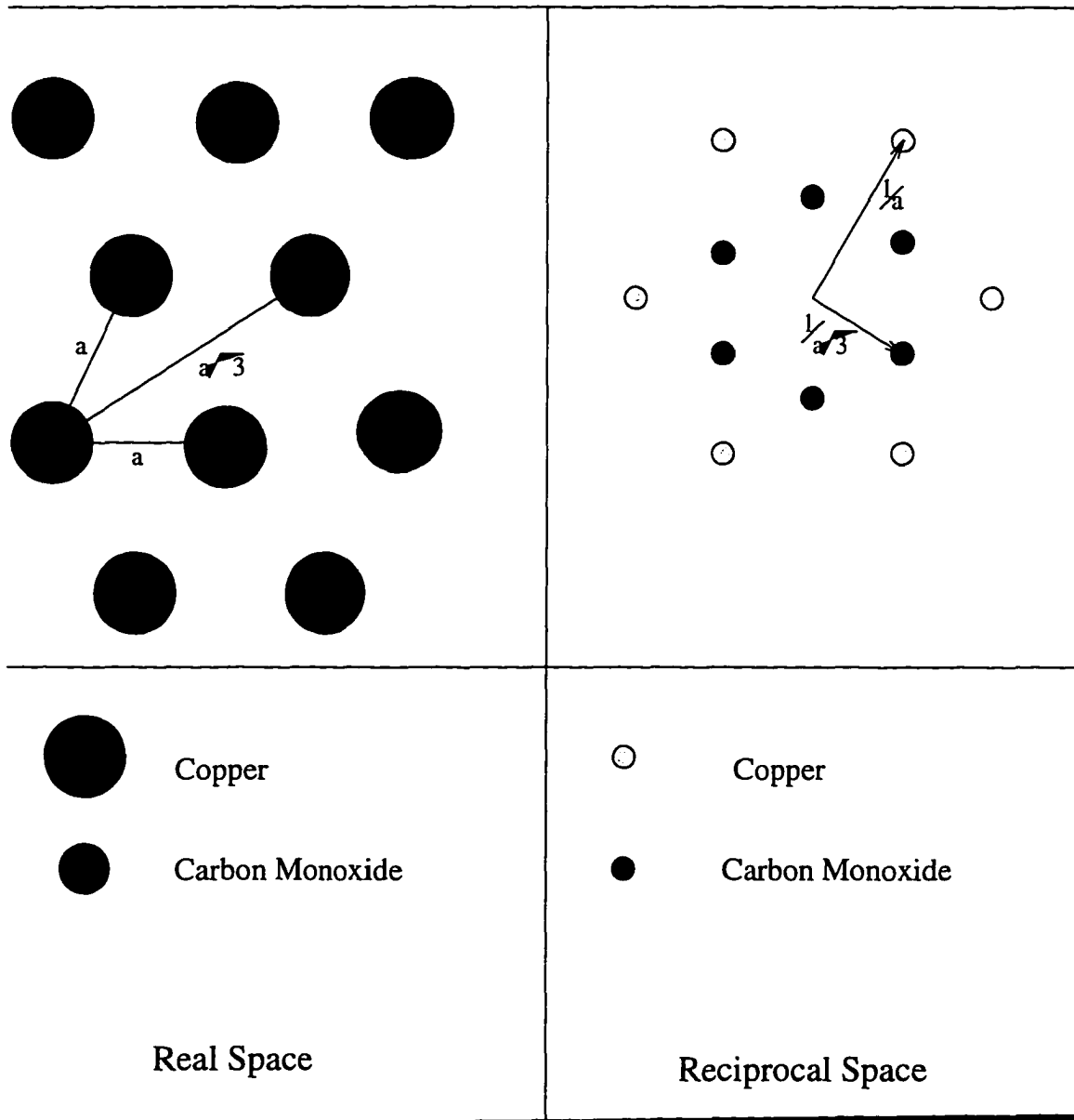
$\sqrt{3} \times \sqrt{3} R 30^\circ$  CO on Cu(111) overlayer structure


Figure 5.2:  $(\sqrt{3} \times \sqrt{3})R30^\circ$  overlayer structure. a) real space b) reciprocal space

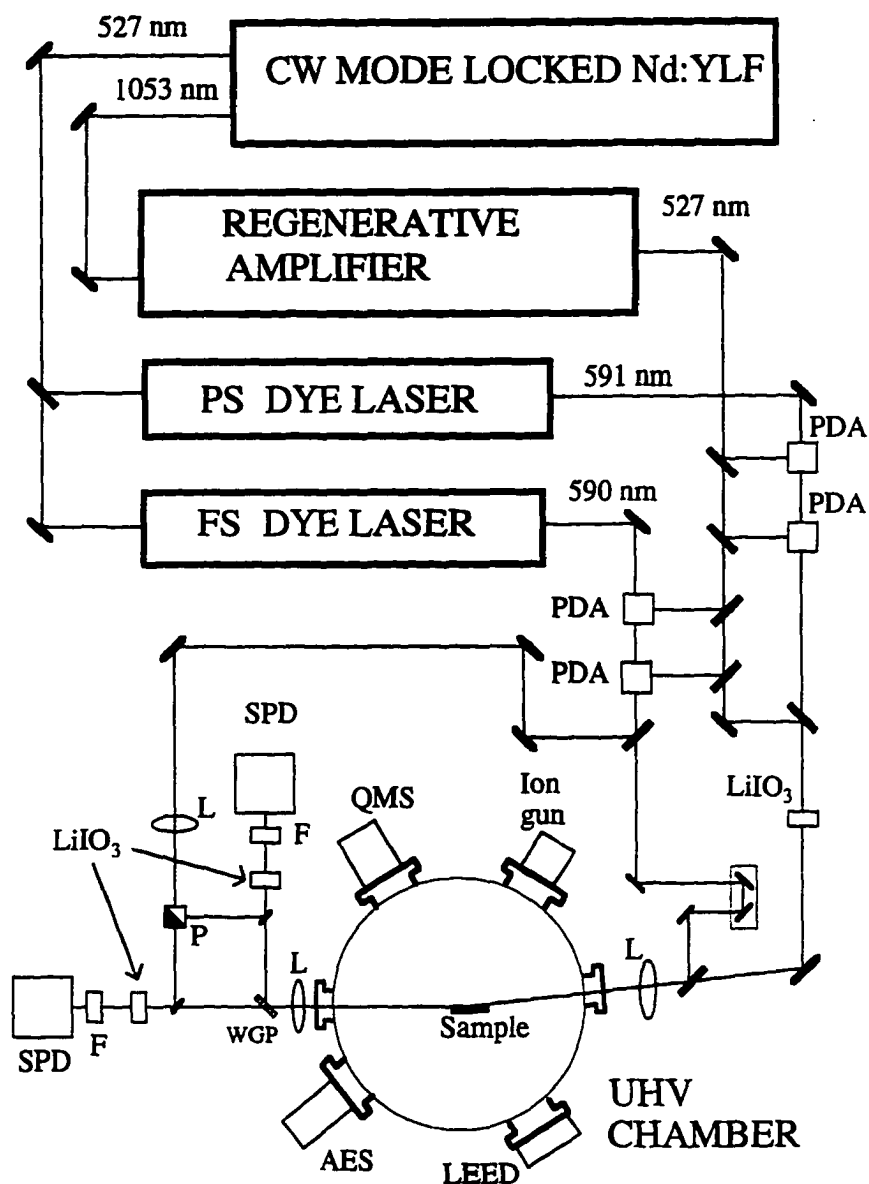


Figure 5.3: Schematic of the apparatus. FS DYE LASER, synchronously pumped hybrid mode-locked dye laser (pulses  $\sim 200$  fs in duration); PS DYE LASER, synchronously pumped dye laser (pulses  $\sim 30$  ps); PDA, pulsed dye amplifier cells; F, spectral filter; SPD, silicon photodiode; L, lens; WGP, wire grid polarizer; P, polarizer; LEED, low energy electron diffraction; AES, Auger electron spectrometer; QMS, quadrupole mass spectrometer.

fundamental radiation (i.e.  $1.053 \mu\text{m}$ ) seeds a Nd: YLF regenerative amplifier.

One of the dye lasers generates femtosecond pulses using a dual jet hybrid mode-locked design[63, 64]. An intercavity prism pair placed at one end of the linear cavity is double passed to provide dispersion compensation. Rhodamine 590 is used as a gain medium and a 2/3 mixed solution of DODCI/DQOCI as a saturable absorber. The output train consists of 280 fs pulses at 76 MHz with 0.3 nJ pulse energy centered at 588nm. The other synchronously pumped dye laser operates with a single jet, a 3-plate birefringent filter and an intercavity etalon in the cavity, producing narrowband ( $1 \text{ cm}^{-1}$ ), tunable (580 - 610 nm), 30 ps pulses.

The 1 kHz doubled output of the regenerative amplifier (1mJ, 60ps, 527nm) provides pump energy for a series of dye amplifiers. The dye amplification cells, arranged in two stage pairs, with pump energy ratios of 20%-80% for the first and second stages respectively, use Rhodamine 610 with water as a gain medium and are pumped collinearly. The femtosecond pulses are amplified by a set of dye cells with 500  $\mu\text{J}$  total pump power. In the first stage the pump and seed pulses copropagate. In the second stage the pump and seed pulses counterpropagate. The picosecond pulses are amplified by the other set of amplifiers with 100  $\mu\text{J}$  total pump power, and both stages copropagating.

The resulting femtosecond pulses (4  $\mu\text{J}$ , 300 fs) are then split into pump and gating pulses, while the amplified picosecond pulses(3  $\mu\text{J}$ , 30 ps), are down-converted

by difference-frequency-generation in a 1 cm  $\text{LiIO}_3$  crystal with the  $200\mu\text{J}$  of the remaining doubled regenerative amplifier output. Tunable ( $1800 - 2100\text{ cm}^{-1}$ ) quasi-CW, 10 nJ infrared pulses with a spectral fullwidth of  $1\text{ cm}^{-1}$  are produced.

The pump visible pulses and probe IR pulses were made collinear and using a 2f focusing relay introduced into a UHV chamber containing the Cu(111) crystal sample. The visible pump pulses are p-polarized, and the IR beam polarization was adjusted to be 70% p-polarized and 30% s-polarized. Optimizing the incident angle for the best sensitivity and signal level involves balancing the probe absorption that has a maximum at  $\theta = 88^\circ$  and the fluence absorbed which peaks at  $\theta = 62^\circ$ . The functional forms of this are detailed in appendix (9.1). For most experiments a particular fluence was desired. In this case the greatest angle possible was used to increase sensitivity. Because of the limits in laser power it was necessary to use angles less than  $88^\circ$  for all measurements. The incident angle, spot sizes and fluences are for each measurement are indicated later in the results chapter.

Time-resolved *detection* is accomplished by difference frequency mixing the IR beam reflected off the sample with the optically delayed visible gating pulses in  $\text{LiIO}_3$  crystals. A wire grid polarizer is used to separate the p-polarized and s-polarized components of the IR beam. Subsequent upconversion of these components in separate  $\text{LiIO}_3$  crystals produces pairs of visible pulses ( $\sim 675\text{ nm}$ ) which are detected by two sets of matched photodiodes, amplifiers, and spectral filters. Since the adsorbed CO

stretch vibrations only absorb energy from the p-polarized IR field, the s-polarized reflected beam provides a useful reference signal for normalization on every laser shot. Timing and overlap of the pulses are independently checked by examination of the transient reflectivity signal from the silicon wafer located underneath the Cu on the same sample manipulator as mentioned earlier. Finally gated amplifiers are employed to acquire and ratio the p- and s- polarized transient reflectivity signals on a shot-by-shot basis.

## Chapter 6

### Results and Discussion

In the general description of the infrared response developed in section 4, we found that the physics of the relaxation phenomena is contained in the time variation of the complex frequency  $\Delta S(t, t_p)$  and the population  $n_0(t)$ . In principle any theoretical model explicitly relating substrate evolution to the complex frequency and population of the stretch mode can be tested. A priori there exist many possible effects. This chapter will use the IR probe analysis developed in chapter 4, along with experimental data to discuss possible substrate-adsorbate interactions outlined in chapter 2. Since the experiments involve transient substrate heating, a short discussion of static substrate heating measurements will be presented first.

#### 6.1 CW IR Spectra

Static FTIR measurements were performed as a function of substrate temperature over the temperature range  $55^\circ K - 125^\circ K$  (Fig. 6.1). These measurements provide a context for the transient heating measurements and confirm that the FT-stretch

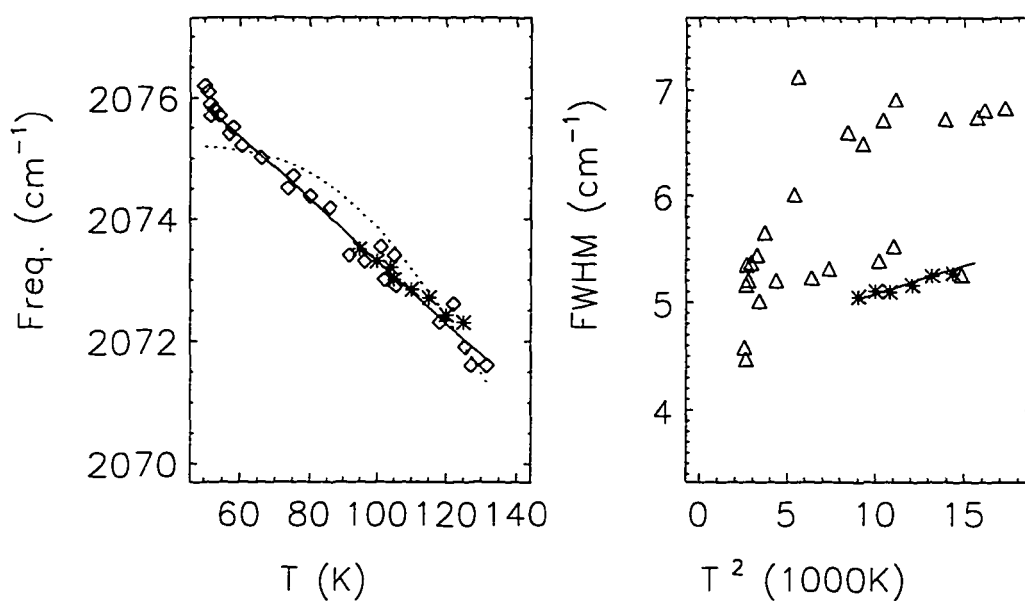


Figure 6.1: Temperature dependence of the C-O stretch absorption. The open diamonds and triangles are data obtained with the helium dewar. The asterisks are data obtained with the LN<sub>2</sub> dewar. The solid lines are fits to the dephasing model with  $\hbar\Omega = 45 \text{ cm}^{-1}$ . The dashed lines is the best fit using the FR frequency  $\hbar\Omega = 280 \text{ cm}^{-1}$ .

dephasing model adequately describes the temperature dependent complex frequency shift. Two sets of measurements were made, one with a helium dewar and one set with a LN<sub>2</sub> dewar. The helium dewar provided much lower temperatures, however the measurements were adversely affected by the temperature oscillations discussed earlier. The spectra obtained were averages over a temperature range of  $\sim 5^\circ$ . The averaging did not effect the line center determination but noticeably degraded the linewidth measurements. Much better linewidths were obtained using the LN<sub>2</sub> dewar over a smaller temperature range.

The dephasing model of section 2.3 predicts that for a low frequency dephasing mode, Q, with frequency  $\Omega$  and population  $\bar{n}$ , the stretch mode complex frequency shifts as;

$$\delta_s(T) = \delta\omega\left(\bar{n} + \frac{1}{2}\right) \quad (6.1)$$

$$\gamma_s(T) = \frac{\delta\omega^2}{W} \left( \bar{n}(\bar{n} + 1) + \frac{1}{4} \right). \quad (6.2)$$

Here  $\delta_s(T)$  and  $\gamma_s(T)$  are the center frequency and linewidth shifts respectively, and  $\delta\omega = \frac{\zeta}{\hbar} Q_0^2$  is the anharmonic coupling between the stretch mode and mode Q, as defined in Section 2.3.

Within the accessible temperature range the measured CO stretch lineshift varies linearly according to  $\omega_{10} = [2078.4 - 0.052 * T] \text{cm}^{-1}$ . This variation indicates the measurements are in the high temperature limit of the exchange theory where  $\bar{n}$  becomes linear in temperature,  $\bar{n} \sim \frac{kT}{\hbar\Omega}$ . A nonlinear least squares fit of the frequency

shift with equation 6.1 places an upper limit of  $\Omega \leq 110\text{cm}^{-1}$ . Since the frequencies of the frustrated rotation ( $\omega_{FR} \sim 281\text{ cm}^{-1}$ ) and the Cu-CO stretch ( $\omega_{Cu-CO} \sim 330\text{ cm}^{-1}$ ) are too high to account for the FTIR data, the frustrated translation with a theoretically expected frequency  $< 100\text{ cm}^{-1}$  is proposed to be the dephasing mode. This assignment is also supported by studies of atop bound CO on Pt(111)[65, 66], and Cu(100)[14], Ru(100)[48]. In all these examples the frustrated translation dephases and shifts the frequency of the stretch mode. For an experimental estimate of the lower limit of  $\omega_{ft}$  we use the Cu(100) result which is the lowest measured frequency of  $\omega_{ft}$  on a metal surface.

Analysis of the linewidths for the LN<sub>2</sub> dewar data was consistent with the lineshift measurements. Equation (6.2) predicts a quadratic high temperature limit for the dephasing rate (linewidth) of the CO-stretch transition and we modeled  $\gamma_s(T)$  accordingly obtaining a best quadratic fit  $\gamma_s(T) = (4.85 + 0.000065T^2)\text{cm}^{-1}$ .

These results confirm the notion that the substrate temperature shifts the stretch mode frequency due to thermal population of the FT motion. The slope of the shift yields the ratio of the zero temperature anharmonic shift to the oscillator frequency. Experimentally we find  $\frac{\delta\omega}{\hbar\Omega} = 0.0753$  and  $W=80\text{cm}^{-1}$ . This can be compared to the density functional theory calculations for  $\delta\omega$  and  $\hbar\Omega$  of CO on Cu(100) that yield a ratio of  $\frac{\delta\Omega}{\hbar\Omega} = 0.022$ . With the presently available data the factor of 3 difference could be due to the prediction of either  $\delta\omega$ ,  $\hbar\Omega$ , or a combination of both. Better

low temperature FTIR measurements of Helium scattering studies will be needed to determine  $\hbar\Omega$  and  $\delta\omega$  separately.

## 6.2 Transient IR measurements

The data of Fig. (6.2) depicts the general features of our differential reflectivity measurements as a function of probe IR frequency. The differential reflectivity measured at a fixed time delay of 3.5 ps between the pump and the gate pulses, exhibits behavior indicative of a shifting Lorentzian absorption spectral line. The shift is a fraction of the linewidth, and since the feature is roughly symmetric the linewidth and integrated absorption remain roughly constant. Explanations for the observed signal that involve a loss of adsorbers by mechanisms such as diffusion, desorption or dissociation are unlikely from the outset since they would involve a decrease in the integrated absorption. Frequency scans taken at longer relative delay times indicate the feature remains qualitatively the same but with a decreased amplitude. Similar observations were obtained in the other visible pump/IR probe experiments by Germer et al for CO on Pt(111)[14] and Cu(100)[22].

In Fig. 6.3 we exhibit measured transient reflectivity with the probe laser tuned off resonance by  $1.5\text{ cm}^{-1}$  to the higher energy side of the  $2073.5\text{ cm}^{-1}$  resonance (i.e.  $\omega_{10} = 2075\text{ cm}^{-1}$ ) with a pump fluence of  $0.072\text{ mJ/cm}^2$ . We see that the signal rises, peaks at  $\sim 3\text{ ps}$ , and then exponentially decays with a characteristic time of  $\sim 3\text{ ps}$

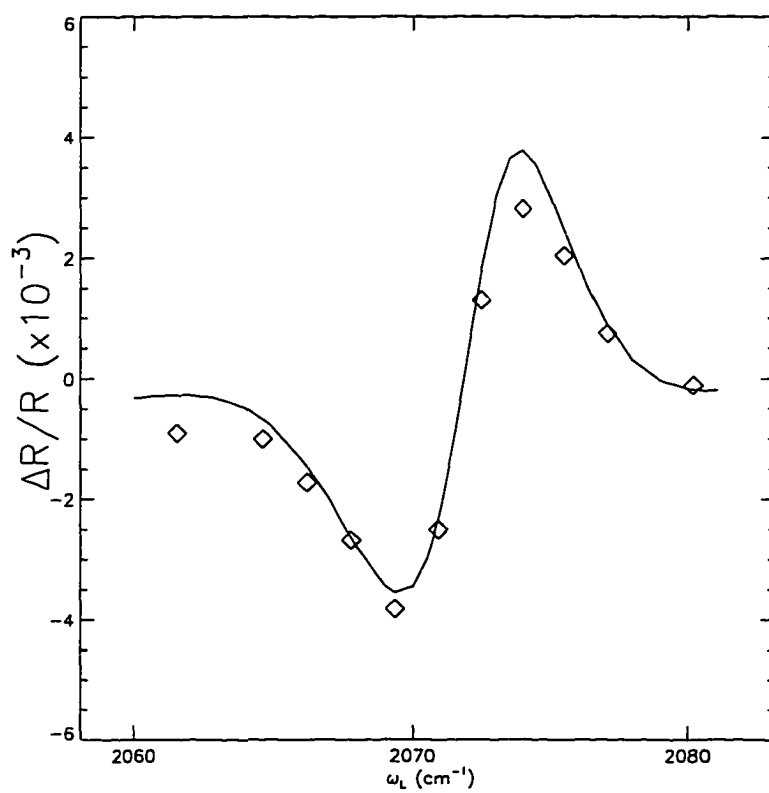


Figure 6.2: Transient fractional difference reflectivity of CO on Cu(111). Frequency scan taken at fixed time delay of 3ps.

returning to a plateau  $\sim 40\%$  the peak value. These features clearly rule out direct excitation of the CO stretch by either nascent or thermal electrons. Direct excitation by nascent electrons would occur during the 300 fs visible pulse duration. The new population would then decay with the CO stretch  $T_1$  time of  $\sim 1-2$  ps. Neither the signal growth kinetics, the 3 ps decay nor the plateau can be accounted for with such a scenario. The thermal population of the CO stretch can be estimated with equation (2.49). At the present fluence levels the  $v=1$  C-O mode obtains a peak population of  $1 \times 10^{-4}$ . Multiplying this change in population times the 5% static absorption places an upper limit on the signal strength at  $5 \times 10^{-6}$ , about 1000 times smaller than the signal we observe.

Instantaneous dephasing processes involving substrate electron-hole pairs would cause line broadening. As evident in the model for an impulsive perturbation (equation (4.22) and Fig. 4.4 an instantaneous line broadening would grow in with the new  $T_2$  dephasing time which, by assumption, would be extremely short. The smoothness of the rising edge data in Fig. 6.3b rules out the existence of any fast components in the new absorption at current signal to noise levels. One simple model remains, whereby the CO internal stretch is anharmonically coupled to a lower frequency surface adsorbate mode, as described in section 2.3.

Relating the features of the experimental data to the substrate temperatures, the phonon temperature profile seems an unlikely candidate as the sole driving force of the

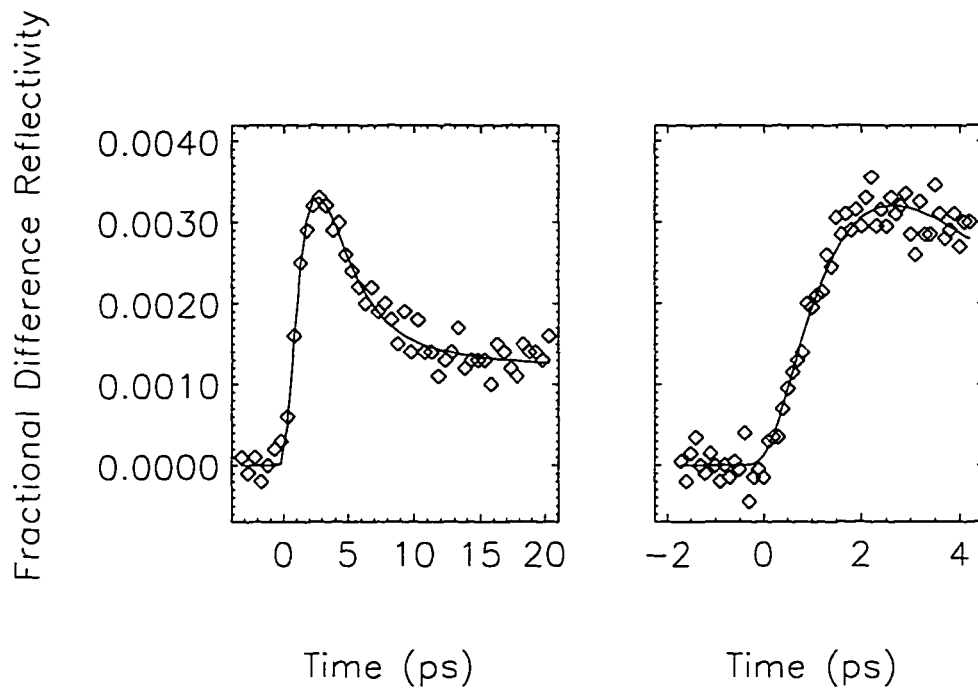


Figure 6.3: Transient fractional difference reflectivity of CO on Cu(111). Time scans with a visible pump  $F_{abs}=0.072$  mJ/cm<sup>2</sup> and probe laser with  $\omega_L = 2075$  cm<sup>-1</sup>; a) from -3 to 20 ps, b) from -2 to 4 ps.

adsorbate response. On the other hand, if the electronic temperature is responsible for the peak feature in the adsorbate response then something must account for the delay of the peak by 2 ps. This delay can again be understood using the model of an impulsive perturbation discussed in section 4.2. From equation (4.22) and Fig. 4.5, one can see that for an instantaneous shift in frequency, a new absorption grows in with the inverse of the new linewidth. For small frequency shifts, and small detunings the new signal will grow in with a response time of  $1/\Gamma \sim 2.2ps$  and hence the signal peaks roughly 2ps after the peak adsorbate temperature.

To fit this data a few issues must first be discussed. The magnitude of the signal depends upon the fluence absorbed. Since we have two overlapped Gaussian beams (i.e. the pump and probe beams) there are a distribution of temperatures and hence frequency shifts being probed. This can be accounted for by noting the cylindrical symmetry of the Gaussian beams and then calculating the signal obtained from rings that have surface areas of similar temperature. We used 5 rings, each with 20% of the total IR light intensity. For each ring the average fluence was calculated. Once the signals for each fluence were calculated they were averaged together to obtain a final signal that was compared with the detected signal. This process weights the signal calculated for a particular ring with the percentage of the total IR light which is probing it.

The average fluence absorbed for an IR beam waist of  $\omega_{ir}$ , visible beam waist of

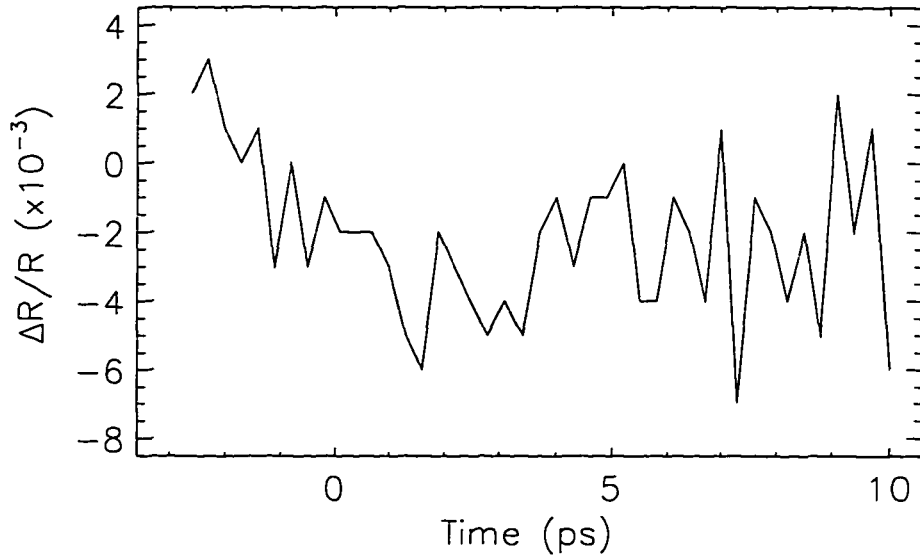


Figure 6.4: Transient fractional difference reflectivity of bare Cu(111). The pump pulse imparted a fluence of  $F_{abs} = 0.33 \text{ mJ/cm}^2$ .

$\omega_{vis}$  and a total visible beam energy absorbed of  $U_{abs}$ , is  $F_{avg} = \frac{U_{abs}}{\pi(\omega_{ir}^2 + \omega_{vis}^2)}$ . Experimental determination of  $F_{avg}$  proved to be difficult. The main errors are in overlapping the beams due to a combination of alignment errors, drifting and deviations from a Gaussian beam profile. These effects combined to give us a fitted fluence value of about 50% the value predicted from direct pulse energy and beam waist measurements.

In addition to the pump induced changes in the CO absorption there are pump induce changes in the bare metal reflectivity. Fig. (6.4) depicts the transient reflectivity of of the bare metal surface following a heating pulse with a fluence absorbed of  $F_{abs} = 0.33 \text{ mJ/cm}^2$ . The signal follows the lattice temperature with a

$\frac{dR}{dT_i} = 0.00003 \frac{1}{\text{K}}$ . Thus the substrate response contributes a signal  $\sim 1/10$  the size of the differential signal when CO is present. This is roughly in accordance with static temperature changes in the dielectric constant of Cu. For light of wavelength  $5\mu\text{m}$ , the measured Cu dielectric constants at 82K and 295K are  $2.48 + 32.8i$  and  $3.02 + 32.8i$  respectively[67]. To fit our data we extended the femtosecond experimental result at  $\theta_{inc} = 66^\circ$  to other incident angles using the angular dependence obtained from the reported static temperature dielectric constants.

In appendix 9.1 it is shown that modulations in the dielectric constants and the adsorbate susceptibility yield additive signal modulations. The fits were obtained using the following equation;

$$\left(\frac{\Delta R}{R}\right)_{pump} - \left(\frac{\Delta R}{R}\right)_{unpump} = 2\text{Re}\{\zeta(t) + iG(\chi(t) - \chi_0)\} \quad (6.3)$$

where  $\zeta(t) = \frac{dR}{dT}T(t)$ , G is defined in appendix 9.1 and  $\chi(t)$  and  $\chi_0$  are the adsorbate susceptibility defined in chapter 4

The time-dependent population of the frustrated translation mode,  $n_{ft}$ , is predicted using the following rate equation for a harmonic oscillator,

$$\dot{n}_{ft} = \gamma_e(n_e - n_{ft}) + \gamma_l(n_l - n_{ft}). \quad (6.4)$$

where  $n_e$  and  $n_l$  represent the occupation numbers of the reservoir excitations at energy  $\hbar\Omega$  for the instantaneous temperatures  $T_e$  and  $T_l$  respectively[13].  $\gamma_e$  and  $\gamma_l$  are the coupling rates of the frustrated translation to the substrate electrons and the

phonon reservoirs respectively. For simplicity and later comparisons  $\gamma_e$  is first treated as *temperature independent*. Later we relax this assumption.

The complete fitting procedure is outlined in Fig. 6.5. Trial values of  $\gamma_e$  and  $\gamma_l$  are used to calculate  $n_{ft}$  from the  $T_e$  and  $T_l$  profiles. The stretch mode complex frequency is calculated using the FTIR results. The differential reflectivity is then calculated for the appropriate probe laser frequency. The predicted signal is compared with the data to obtain the  $\chi^2$  which is used to optimize  $F_{abs}$ ,  $\gamma_e$ , and  $\gamma_l$ . The values of  $\omega_L$  and the time of the pump pulse arrival are allowed to vary within the following constrained regions;  $\omega_L = \omega_L^{meas} \pm 0.6 \text{ cm}^{-1}$  and  $\tau_p = \tau_p^{meas} \pm 0.3 \text{ ps}$ .

Best fits of the data reveal that couplings to both electrons and phonons are present. Our best estimates for the low frequency reservoir coupling rates,  $\gamma_e = 145(24) \text{ GHz}$  and  $\gamma_l = 280(100) \text{ GHz}$ , give the solid lines shown in Fig. 6.3, and give the adsorbate temperature variation shown in Fig. 6.6 (see solid line). The measurements clearly reveal that the frustrated translational mode couples to both electron and phonon bulk temperature reservoirs on a timescale of 2-6 ps. As mentioned earlier there are errors associated with uncertainties in the value of the electron-phonon coupling constant  $G$ . This will be discussed later after all the data has been presented.

Before considering the system response to higher levels of excitation it is worthwhile to review the limitations of the present model. The model assumes temperature-independent coupling rates, and essentially extrapolates static FTIR data obtained

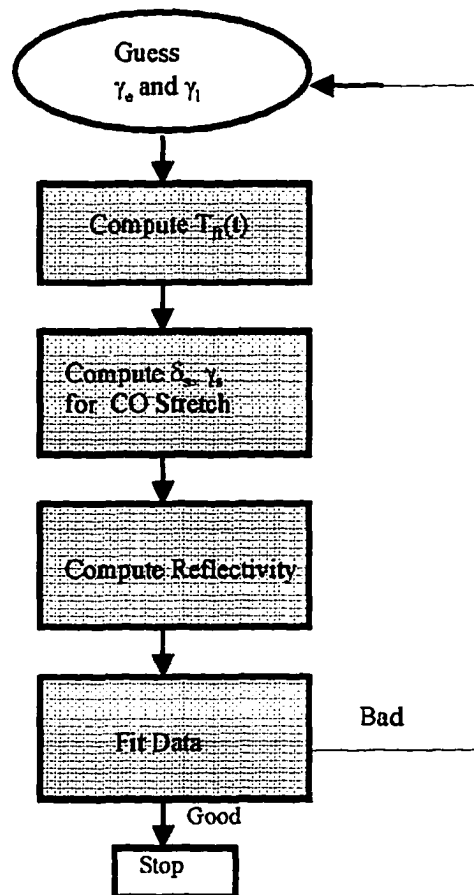
Flow Chart of Procedure to Fit  $\gamma_e$  and  $\gamma_l$ 

Figure 6.5: A schematic of the fitting procedure.

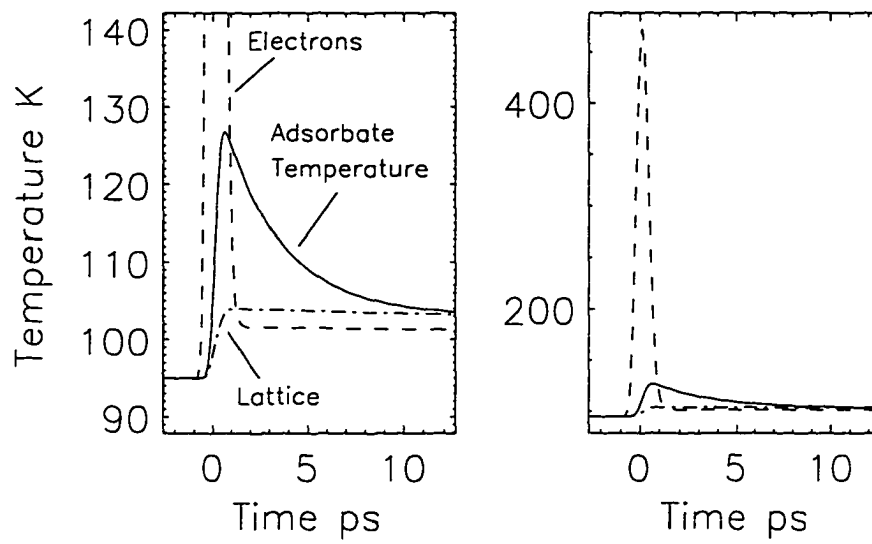


Figure 6.6: Transient temperatures of the CO on Cu(111) system, pulse duration  $\tau_p = 500 \text{ fs}$ ,  $F_{abs} = 0.33 \text{ mJ/cm}^2$ ;  $T_e$  (dashed line),  $T_l$  (dotted line) and  $T_{ft}$  (solid line)

at  $\sim 100^\circ\text{K}$  to temperatures (albeit transient temperatures) in considerable excess of these values. The model treats the frustrated translation as an ideal harmonic oscillator, ignoring anharmonicities that may be important at high temperatures. The possible effects of other low lying vibrational modes, particularly of surface waves that may couple to or be involved in the frustrated translation motion are not incorporated and need to be considered in more detail. On the other hand, the data clearly indicate that the model is a good starting point by which to understand these phenomena at low levels of substrate excitation.

### 6.3 Fluence Dependence

A summary of the complete data set is provided in Table 6.1. Data were taken over fluences up to the desorption threshold and at several frequencies for each fluence in order to increase the accuracy of the numbers reported. Some examples of the data obtained at a fluence absorbed of  $F_{abs} = 0.18\text{mJ}/\text{cm}^2$  are exhibited in Fig. 6.7. These time domain data illustrate the same basic spectral feature as in Figs. 6.2 and 6.3; a shifting Lorentzian absorption profile which exhibits a maximum shift at around 2 ps and returns to an offset value within the next 10 ps. Figure 6.8 exhibits data taken at five different fluences with the probe laser tuned to  $\omega_L \sim 2074.5\text{cm}^{-1}$ .

To maximize the signal level, the low fluence measurements were taken at glancing angles ( $\theta_{incident} \sim 85^\circ$ ) where the effective CO absorption is larger. On the other hand

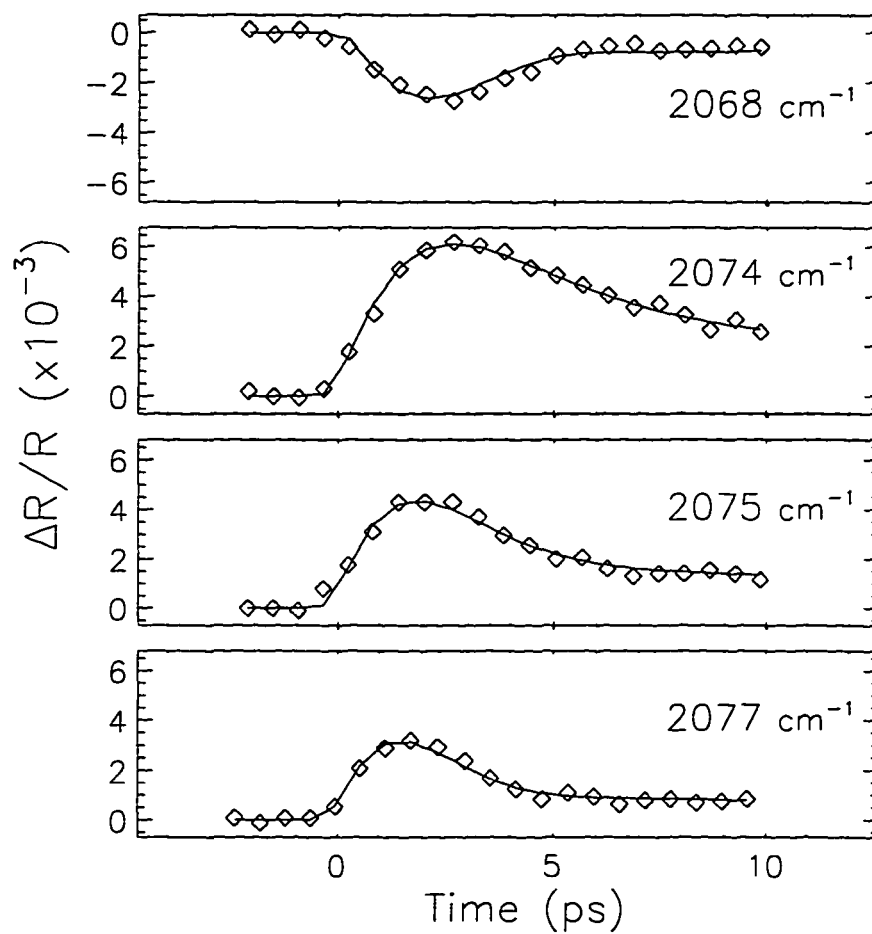


Figure 6.7: Transient fractional difference reflectivity of CO on Cu(111). Time scans as a function of probe laser frequency.

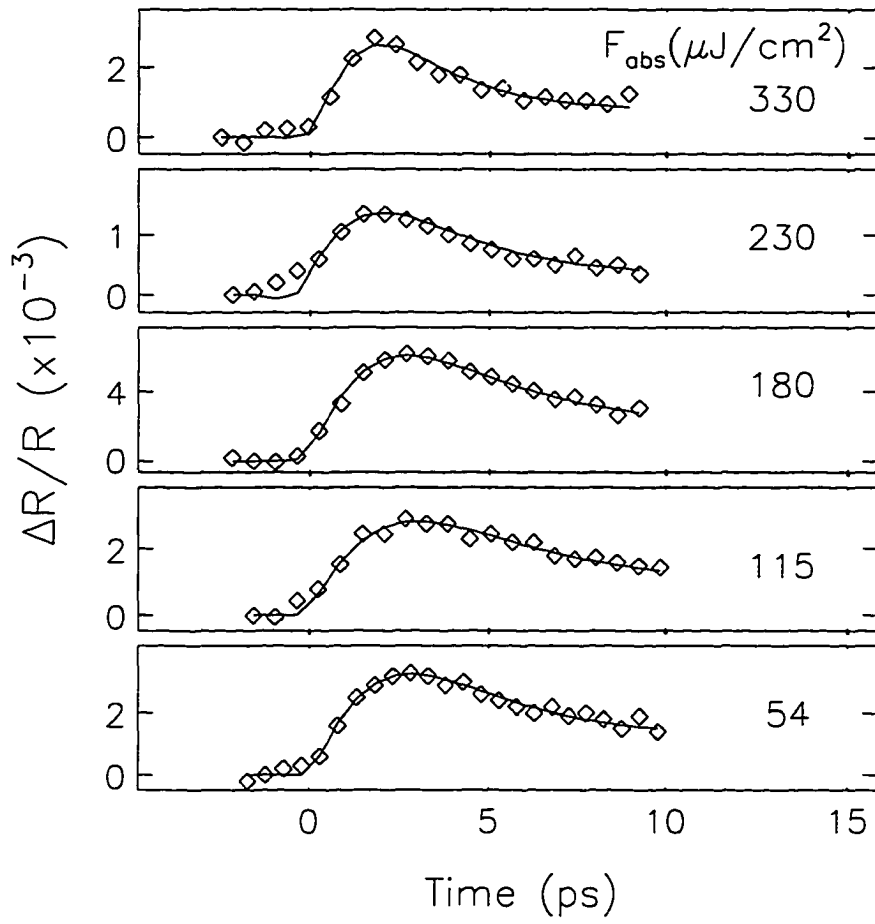


Figure 6.8: Data taken at several different fluences, with  $\omega_L = 2074.5 \pm 0.5 \text{ cm}^{-1}$ . The fits are described in the text.

Table 6.1: Summary of Results

Fluence	$\theta_{incident}$	$\frac{\Delta R}{R}(\%)$	$\omega_L$	$\gamma_e^0$ (GHz)	$\gamma_l$ (GHz)
0.072	84.5	7.5	2075.4	25	278
0.12	79	3.2	2074.6	30	167
			2076.4		
			2077.2		
0.18	79	3.2	2067.7	28	280
			2074.6		
			2076.4		
			2077.5		
0.23	66	1.3	2069.8	20	232
			2075.4		
0.33	66	1.3	2069.2	20	345
			2075.4		

the higher fluence data was taken at smaller incident angles to increase the fluence absorbed. When the incident angle for each measurement is taken into account the magnitude of the signal scales with the fluence absorbed. At fluences higher than  $F_{abs} = 0.33mJ/cm^2$  the total signal level decreased over successive time scans ( $\sim 10$  min) indicating desorption of the CO. Before discussing the fits of these data, we consider the desorption threshold that limited our data range.

#### 6.4 Desorption Threshold

The threshold level of substrate excitation, above which the desorption process occurs is important. We have determined this level using both SHG and IR absorption as time resolved coverage sensitive probes. SHG from the Cu(111) surface provides information about the CO coverage (Fig. [6.9]). Prybyla et al. were able to monitor

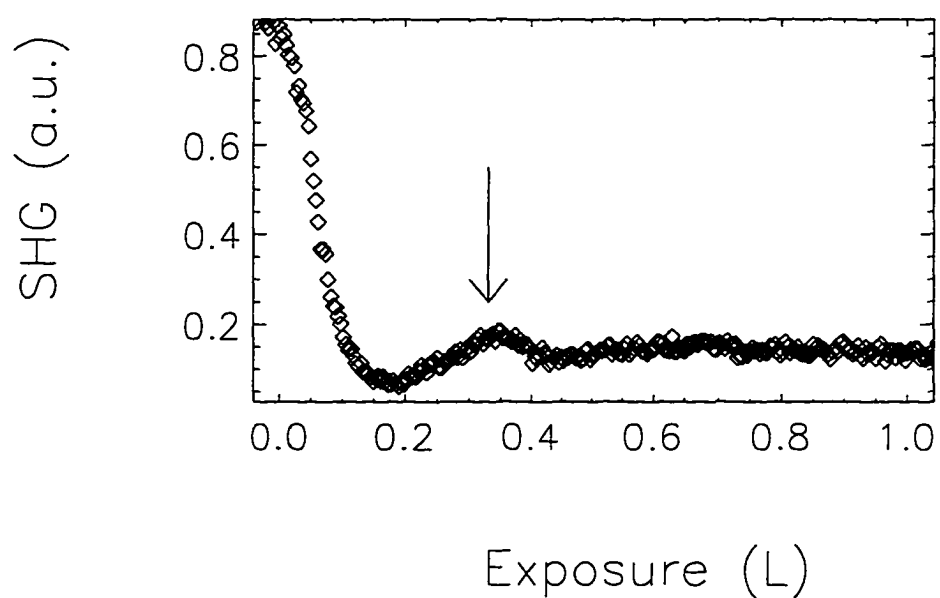


Figure 6.9: Variation of surface SHG signal (at 295 nm) from a Cu(111) surface as a function of CO coverage ( $1 \text{ L} = 1 \times 10^{-6} \text{ Torr s}$ ). The arrow designates the exposure for the ordered overlayer where the transient heating measurements were performed.

desorption induced by 100 fsec 640 nm pulses using an SHG probe[9]. Although our observed SHG was not a linear function of coverage as in Ref. [9] (due in part to our visible laser frequency), we were able to place limits on the desorption threshold. With a  $(\sqrt{3} \times \sqrt{3})R30^\circ$  CO adlayer using the 590nm visible pulse both as pump and SHG probe, we increased the fluence absorbed looking for deviations from the expected  $I(2\omega) = \alpha I^2(\omega)$  dependence. At fluence levels which cause the molecules to desorb, the SHG signal increases towards the the undosed value. At  $F_{abs} \geq 1.25mJ/cm^2$  a 1/3 coverage of CO is reduce by  $\geq 80\%$  in  $10^5$  laser shots. Differential reflectivity also provides information about CO coverage. By observing where the signal strength decreases with an increase in fluence, a lower limit of  $F_{abs} = 0.33mJ/cm^2$  for the desorption threshold is obtained. With  $F_{abs} = 0.33$ , more than 80% of a 1/3 coverage of CO will remain after  $10^7$  laser shots. Combining the transient IR probe results and the SHG results we find the desorption threshold lies between  $0.33mJ/cm^2 < F_{abs} < 1.25mJ/cm^2$ .

## 6.5 Fitting Results

For the fluences in the range of 0.054-0.33 mJ/cm<sup>2</sup> the data clearly agree with the qualitative aspects of the time dependent exchange picture[13]. At higher fluences (see Fig. 6.8), there appears to be a faster adsorbate response. The faster response is due to larger net frequency shifts at higher fluences. As demonstrated in equation

(4.10) the adsorbate polarization depends on the detuning between the laser frequency and the adsorbate frequency. When the probe is off-resonant the signal will oscillate at the difference frequency (i.e.  $\omega_L - \omega_{01}(\tau)$ ). The oscillations generated by the larger frequency shifts will therefore produce signals which appear to decay faster when the probe laser is tuned to the high frequency side of line center[68].

To model the temperature dependence of the coupling rate we must, in general, consider the six temperatures that are needed to describe our system: two for the substrate electrons and phonons, and four for the CO vibrational modes. In principal any of these temperatures could affect the coupling rates. However since the substrate temperatures represent thermal occupation of a continuum density of states they are the most likely to effect the coupling mechanisms. In considering the substrate temperatures, only the electron temperature varies appreciably with fluence (see Fig. 3.1). The change in  $T_e$  can be several times the value of the base temperature of 95 K, and the ratio of the change in  $T_e$  compared to the change in  $T_l$  is  $\frac{\delta T_e}{\delta T_l} \sim 20$ . Thus we concentrate on the  $T_e$  dependence of the coupling rates.

In chapter 2 a dynamical charge transfer model was used to arrive at the following form of a temperature dependent coupling rate;

$$\gamma(T_e) = \frac{\gamma_e^0}{1 - e^{-\hbar\Omega/kT_e}} \quad (6.5)$$

Instead of fitting with a temperature independent rate as done previously, the data were fit for  $\gamma_e^0$  of equation (6.5). An intermediate value of  $\hbar\Omega = 45 \text{ cm}^{-1}$  was used

to obtain the best fit value of for the zero temperature coupling rate  $\gamma_e^0 = 25(\pm 7)$  GHz. The result was obtained using all possible light fluences. The coupling to the phonons was found to be  $\gamma_l = 280(\pm 100)$  GHz. Since  $T_e$  is time-dependent in these measurements, the coupling rate is also time-dependent. This is depicted in Fig. 6.10 for the highest fluence using the best fit value of  $\gamma_e^0$ . Within the errors quoted the same value of  $\gamma_e^0$  was found for all fluences. Thus the excitation dependence of the CO response is well accounted for by the dynamical charge transfer model.

The error bars are derived from nonlinear least squares fitting of the the data. However the value of  $\gamma_e^0$  is subject to the uncertainty of two physical parameters encountered in the full fitting procedure. As has been discussed previously, the range of experimental values for the electron-phonon coupling constant affects the value of  $\gamma_e^0$  [15]. In the present analysis an intermediate value of  $G = 0.7 \text{ W/m}^3 \text{ K}$  has been used. For the values of  $G$  at the ends of the experimental range ( $G = 0.3 - 1.0 \text{ W/m}^3 \text{ K}$ ), we find  $\gamma_e^0 = 10(+6 -2)$  GHz and ,  $\gamma_e^0 = 30(\pm 7)$  GHz respectively. The zero temperature rate  $\gamma_e^0$  also depends on  $\hbar\Omega$  and for the values at the ends of the range  $\hbar\Omega = 30 - 60 \text{ cm}^{-1}$ , we find  $\gamma_e^0 = 21(\pm 7)$  GHz and  $\gamma_e^0 = 33(\pm 7)$  GHz respectively. As noted above, we are assuming the coupled mode is harmonic. No experimental information yet exists to test this assumption.

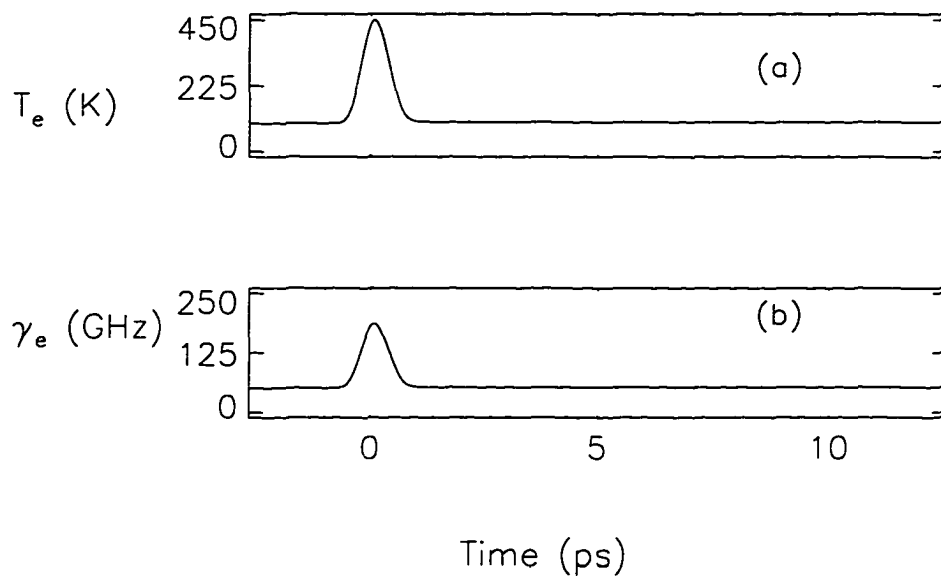


Figure 6.10: The coupling rate  $\gamma_e$  depends on the Fermi distribution of the electrons. Since the electron temperature is time dependent the coupling rate is also time dependent. The time evolution of (a)  $T_e$  and (b)  $\gamma_e$  are shown for the best fit value of  $\gamma_e^0$  with  $\hbar\Omega = 45 \text{ cm}^{-1}$  and  $F_{abs} = 0.23 \text{ mJ/cm}^2$ .

## 6.6 Discussion

The present analysis makes use of temperature-dependent coupling rates ( $\gamma_e(T_e)$ ) derived from the dynamical charge transfer model for adsorbate/substrate vibrational energy relaxation. The 95°K value for the coupling rate,  $\gamma_e(95) = 50GHz$ , is lower than the value  $\gamma_e = 145GHz$ , obtained using a temperature independent analysis with the same physical constants[69]. The present fits have similar  $\chi^2$  values to those obtained using the previous method that employed a fixed temperature-independent rate,  $\gamma_e$ . Thus one can see that these experiments do not uniquely establish the presence of temperature dependent rates but the results are entirely consistent with the more complete and basic theoretical model.

The most recent theoretical predictions for  $\gamma_e$  are molecular dynamics (MD) calculations which incorporate electronic friction. These calculations predict a  $\gamma_e = 23$  GHz for  $T=10K$  and  $\gamma_e = 43$  GHz for  $T=150K$ [26]. Allowing for the uncertainty in the electron-phonon coupling rate, these are in reasonable agreement with our findings. In contrast the temperature independent rate of  $\gamma_e = 145GHz$ , differs by a factor 3 with the theory predictions. In addition the temperature dependence of  $\gamma_e$  predicted by the MD calculations is similar to the DCT results with the coupling increasing by a factor of two between 10K and 150K. Our analysis does differ from the MD calculations in one particular way. The MD calculations conclude that the couplings are not independent. To determine each separate coupling rate the other

relaxation mechanism is turned off. When the separate rates are obtained in this manner and added together they equal a rate slower than the rate found when both mechanisms are activated simultaneously. It is not clear whether this is an artifact of their calculation or has real physical significance. We have analyzed our data assuming that the couplings are independent as this is the simpler model and adequately describes our data.

The most recent calculations for  $\gamma_l$  are density functional (DF) calculations which have a more complete treatment of the electrons than the MD calculations and also use a slab geometry to better capture the periodic nature of the surface. The DF theory predicts a value of  $\gamma_l = 333$  GHz which is in good agreement with our results. The MD calculations on the other hand predict rates of 103 GHz for 150K which is off by a factor of 3 from our results. It should be noted that the error bars on the  $\gamma_l$  are  $\pm 100$  GHz and so the MD prediction can not be completely ruled out by our experiment.

## Chapter 7

### Free Induction Decay

This chapter will present free induction decay (FID) measurements of the vibrational dephasing of CO adsorbed on Cu(111). This represents the first measurement of a FID signal from an adsorbate on a metal. A short IR pulse (380 fs) generates the vibrational coherence and its temporal evolution is measured by upconverting the decaying surface polarization with a delayed visible pulse. In addition to the FID measurement, a frequency domain surface sum frequency generation (SFG) spectrum was measured for CO on Cu (111) using spectrally narrowed IR pulses at two coverages, 0.10 and 0.45 L. The spectra, especially at low coverage, display an interference which was analyzed to determine the relative amplitude and phase of the resonant and nonresonant parts of the second-order susceptibility. The total dephasing time and linewidth obtained in the time and frequency domains are self-consistent. The values agree with those obtained in the FTIR studies discussed earlier.

## 7.1 Experimental

The experimental apparatus for these measurements is depicted in Fig. 7.1. The same laser system as described in chapter 5 was used with a few alterations. For these experiments only the hybrid mode locked dye laser was used. The amplified visible pulses from this laser were used to generate IR and to detect the adsorbate polarization using a 3 wave mixing scheme.

In the free induction decay measurement, we coherently excite CO adsorbed on Cu(111) with a 380 fs IR pulse at  $2074\text{ cm}^{-1}$  and interrogate the temporal evolution of the coherence by measuring the variation of a surface-induced upconversion signal using a 280 fs visible pulse that is delayed with respect to the IR pulse. The spectrally narrowed IR pulses ( $2\text{ cm}^{-1}$ , 10 ps) were used to obtain the surface SFG spectra as a function of IR frequency at two coverages. In both cases gated photon counting was employed to detect the SFG signal. The laser was operated at 591 nm to generate IR at the frequency of the CO stretch (near  $2075\text{ cm}^{-1}$ ) on Cu(111). The dye laser bandwidth was  $100\text{ cm}^{-1}$ . For the frequency domain work, the saturable absorber was removed and a 3 plate Lyot filter was placed in the cavity. The pulses were thus spectrally narrowed to  $2\text{ cm}^{-1}$  and temporally broadened to 10ps.

Short IR pump pulses were generated in an optical parametric amplifier by mixing the amplified dye laser pulse ( $10\text{ }\mu\text{J}$ ) with a portion of a frequency doubled, regeneratively amplified ND:YLF pulse ( $400\text{ }\mu\text{J}$ ) in a 1 mm LiIO<sub>3</sub> crystal. The photon

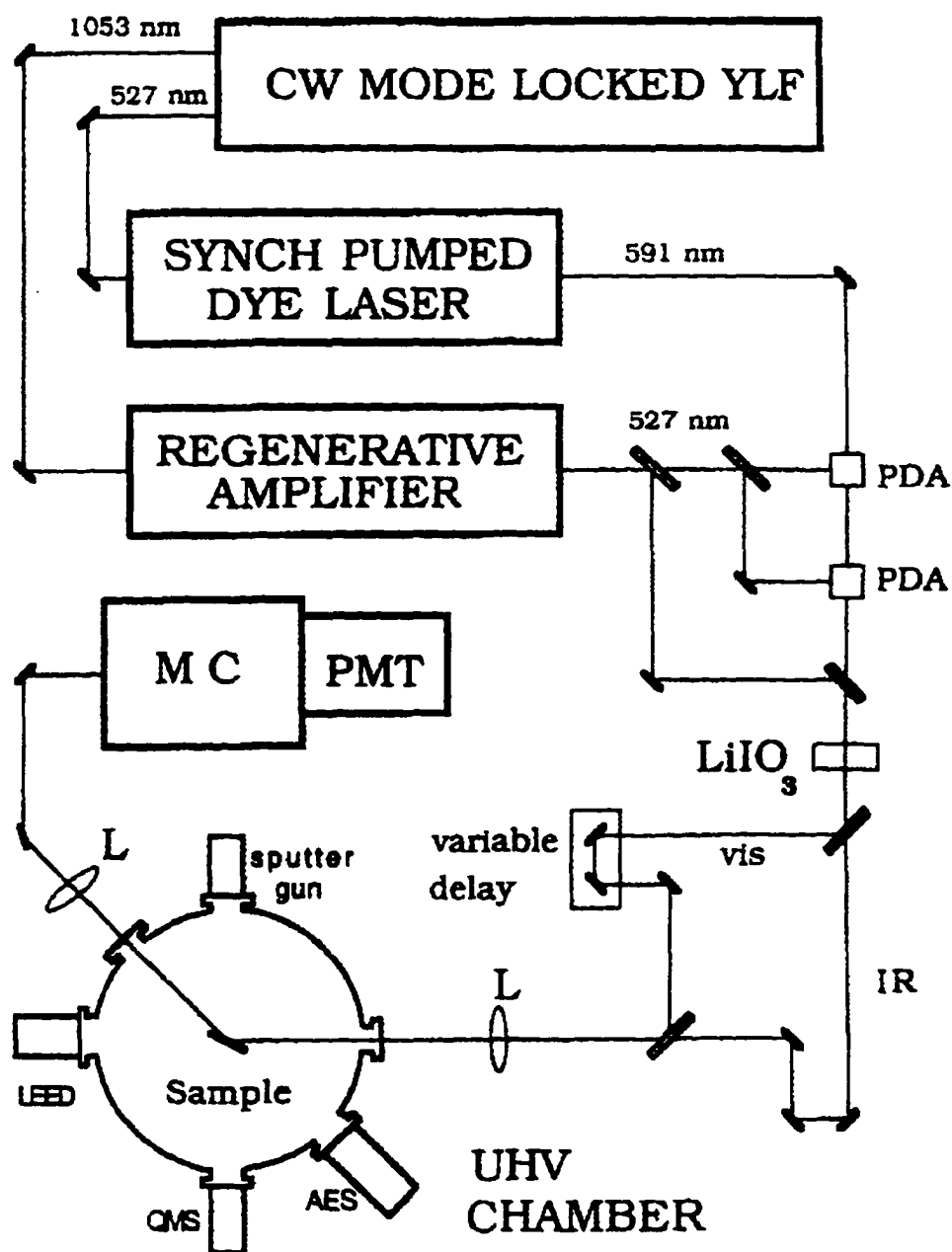


Figure 7.1: Schematic of the apparatus used to measure the free induction decay and surface sum frequency spectrum for CO on Cu(111). PDA, pulse dye amplifier cells, L, lenses; MC a monochromator, PMT, photomultiplier tube; AES, Auger electron spectrometer; LEED, low energy electron diffraction; QMS, quadrupole mass spectrometer.

conversion efficiency was - 0.5 % and the IR pulse energy was - 5 nJ. For the longer (10 ps) pulses, the IR was generated with 10% conversion efficiency in a 1 cm LiIO<sub>3</sub>. 100 nJ IR pulse energies were produced. After the LiIO<sub>3</sub> crystal the IR and dye pulses were separated and optically delayed. The IR and dye pulses were p-polarized with respect to the copper crystal and the beams were recombined and focused on the surface at an incident angle of 72°. The crystal was oriented such that the plane of incidence was along the [211] axis.

While it was possible to focus the lasers to a 250  $\mu\text{m}$  diameter the experiments were performed with beam diameters at 500  $\mu\text{m}$  to avoid photodesorbing CO from the surface and causing temperature shifts in the stretch frequency. The upconverted photons (SFG) were collected outside the chamber and imaged through an interference filter, a 0.5 m double monochromator, and then onto a photomultiplier tube (PMT). The SFG signal at 527 nm was measured by gated single photon counting.

For the FID measurements (Fig. 7.2) the SFG signal was recorded as a function of the relative IR-visible pulse delay. The peak signal was 6 counts/s with a background of 0.01 counts/s. The frequency domain data (Fig. 7.3) were obtained by measuring the SFG signal enhancement as a function of IR laser frequency. The largest signal in this case was about 200 counts/s. These data were acquired by recording the SFG signal for bare copper, and at 0.10 and 0.45 L CO coverages for a fixed frequency setting of the IR source laser. This procedure minimized systematic errors that are

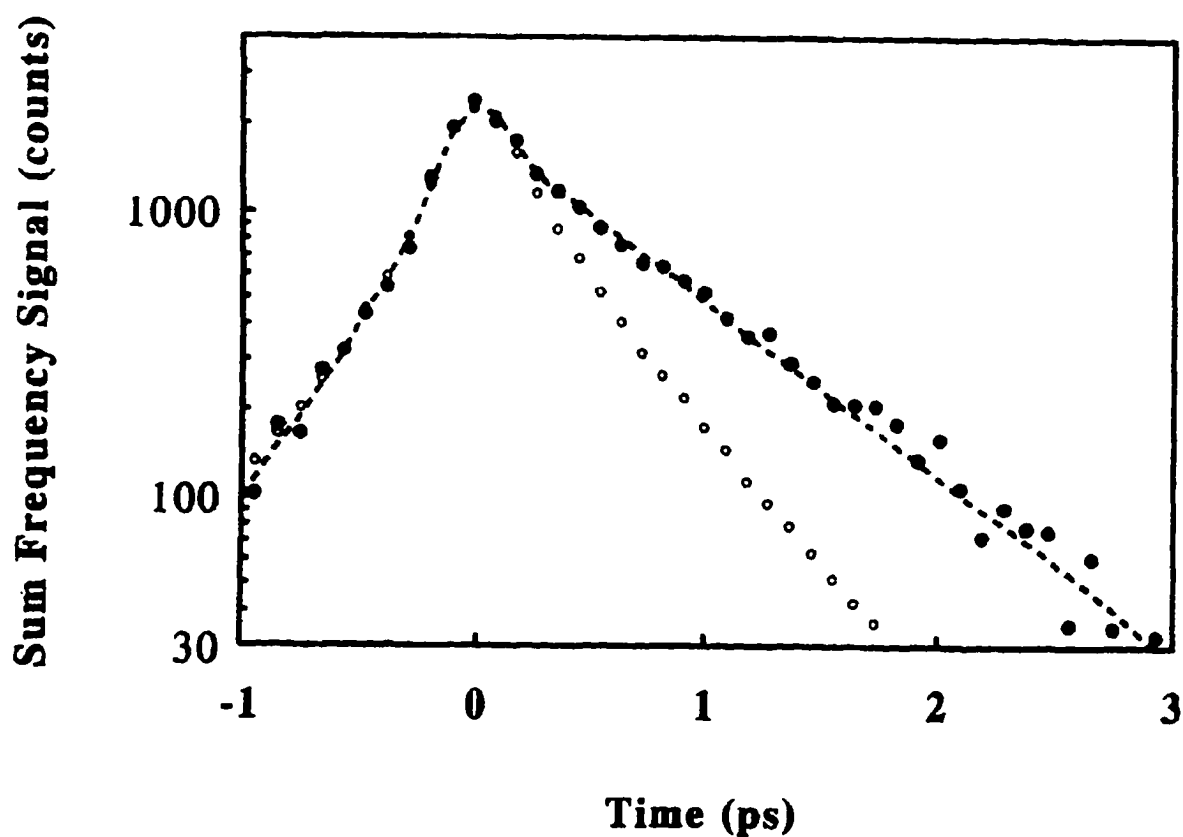


Figure 7.2: The variation of the vibrational coherent transient for CO on Cu(111) at 0.45 L measured using 380 fs IR and 280 fs visible pulses as a function of delay. The signal was obtained using surface SFG. The points are the data and the dashed line is the curve obtained using parameters from a least-squares analysis which yields  $T_2 = 2 \pm 0.3$  ps. A cross correlation of the visible and IR pulses is shown with open circles.

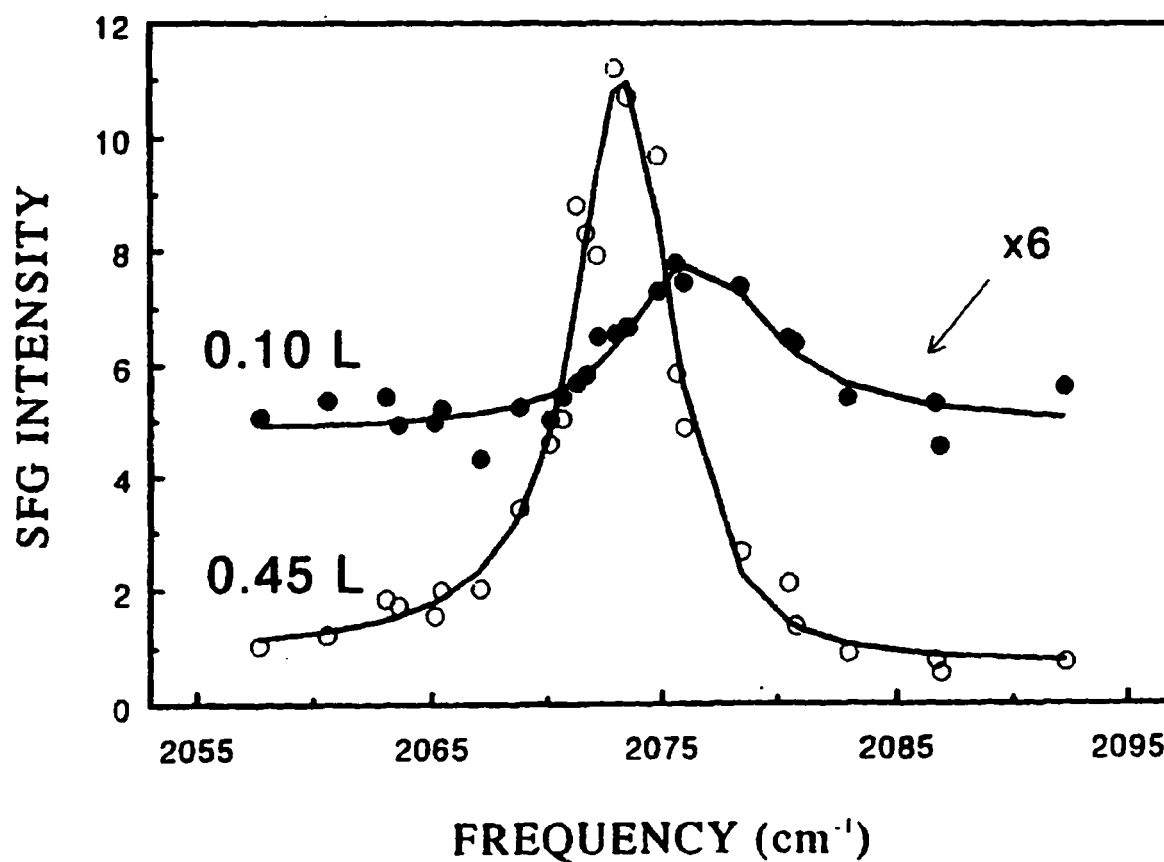


Figure 7.3: IR frequency dependence of the surface SFG enhancement for CO on Cu(111) at 95K for exposures of 0.1 and 0.45 L. The points are the data and the lines are curves derived from the parameters of a least squares analysis

normally introduced by varying the IR frequency at fixed CO coverage.

## 7.2 Theory

In the experiment we coherently excited molecular CO with an infrared pulse, and then probed the temporal evolution of this coherence by surface induced upconversion using a time-delayed visible probe pulse. Interestingly we found that the temporal pro-

file of the infrared ( $E_{ir}(t)$ ) and visible ( $E_{vis}(t)$ ) input electric fields could significantly influence the shape of the curve in Fig. 7.2, and therefore conclusions concerning the total dephasing time. In essence, the resonant and non-resonant contributions of the upconverted field interfere. To account for the interference it is convenient to consider the macroscopic polarization giving rise to the sum frequency signal in the Born-Oppenheimer approximation[70]. In that case the response is given in terms of the macroscopic observables of the surface-adsorbate system. For field envelopes  $\mathcal{E}_v^{(j)}(t)$  and  $\mathcal{E}_{ir}^{(j)}(t)$  corresponding to polarization  $j$ , the complex macroscopic dipole  $P_i(t, \tau)$  oscillating at the sum frequency ( $\omega_v + \omega_{ir}$ ) is given by:

$$P_i(t, \tau)e^{-i(\omega_{ir}+\omega_v)t} = \langle \beta_{ijk} \rangle \{ \mathcal{E}_v^{(j)}(t-\tau) \mathcal{E}_{ir}^{(k)}(t) + \mathcal{E}_{ir}^{(j)}(t) \mathcal{E}_v^{(k)}(t-\tau) \} \quad (7.1)$$

$$+ i \mathcal{E}_v^{(j)}(t-\tau) \int_{-\infty}^t dt' \mathcal{E}_{ir}^{(k)}(t') \langle [\alpha_{ij}, \mu_k(t'-t)] \rangle e^{i\omega_{ir}(t'-t)} \quad (7.2)$$

Here  $\mu_k$ ,  $\alpha_{ij}$  and  $\beta_{ijk}$  are the dipole, polarizability and hyperpolarizability operators respectively, and  $\tau$  the time delay between the visible and the IR pulses. The first term corresponds to the instantaneous (electronic) response from the surface-adsorbate hyperpolarizability. The second term is the polarization resulting from the visible field coupling with the polarizability induced by the infrared field driving the nuclear vibrational motions. The first and second terms can also be considered the non-resonant and resonant terms respectively.

First we consider the resonant term which involves the vibrational dynamics of the CO stretch. This term can be analyzed by expanding polarizability  $\alpha_{ij}$  and dipole

$\mu_k$  in terms of the nuclear displacements. If there is no angular motion the operators  $\alpha_{ij}$ ,  $\mu_k$  can be expanded in terms of nuclear displacements;

$$\mu_k(t) = \mu_k(0) + \left(\frac{d\mu_k}{dq}\right)_0 q(t) \quad , \quad \alpha_k(t) = \alpha_k(0) + \left(\frac{d\alpha_{ij}}{dq}\right)_0 q(t)$$

With these expansions the resonant contribution to the sum frequency polarization (Eq. 7.2) can be written;

$$-i \left(\frac{d\alpha_{ij}}{dq}\right)_0 \left(\frac{d\mu_k}{dq}\right)_0 \mathcal{E}_v^{(j)}(t - \tau) \int_{-\infty}^t dt' \mathcal{E}_{ir}^{(k)}(t') \langle qq(t' - t) \rangle e^{i\omega_{ir}(t' - t)} \quad (7.3)$$

This term is seen to depend on the convolution of the correlation function of the nuclear displacements,  $q(t)$ , with the IR field. For a homogeneous system the correlation, or coherence, of the nuclear displacements decays exponentially with a characteristic decay of  $T_2$ ;

$$\langle qq(t - t') \rangle = \langle 0|q|1 \rangle \langle 1|e^{iH_0(t-t')} q(0) e^{-iH_0(t-t')} |0 \rangle \quad (7.4)$$

$$\langle qq(t - t') \rangle = q_{01} q_{10} e^{i\omega_{10}(t-t')} e^{-(t-t')/T_2} \quad (7.5)$$

The total polarization can now be written as;

$$P_i(t, \tau) e^{-i(\omega_{ir} + \omega_0)t} = \mathcal{E}_v^{(j)}(t - \tau) \left\{ A e^{i\theta} \mathcal{E}_{ir}^{(k)}(t) - iB \int_{-\infty}^t dt' \mathcal{E}_{ir}^{(k)}(t') e^{i\delta\omega(t' - t)} e^{(t' - t)/T_2} \right\} \quad (7.6)$$

where  $\delta\omega = \omega_{ir} - \omega_{10}$ ,  $A e^{i\theta} = 2\langle \beta_{ijk} \rangle$  and  $B e^{i\theta} = \left(\frac{d\alpha_{ij}}{dq}\right)_0 \left(\frac{d\mu_k}{dq}\right)_0 q_{01} q_{10}$ . We can now look at the time and frequency domain data by taking the short and long IR pulse limits respectively.

### 7.2.1 Frequency Domain

To obtain the SFG spectra the IR pulse was long and tunable. Taking the CW IR limit and setting  $\tau = 0$ , the polarization can be written:

$$P_i(t)e^{-i(\omega_{ir}+\omega_v)t} = \mathcal{E}_v^{(j)}(t)\mathcal{E}_{ir}^{(k)}\left\{Ae^{i\theta_a} - iBe^{i\theta_b} \int_{-\infty}^t dt' e^{i\Delta_{10}(t'-t)} e^{(t'-t)/T_2}\right\} \quad (7.7)$$

$$= \mathcal{E}_v^{(j)}(t)\mathcal{E}_{ir}^{(k)}\left\{Ae^{i\theta_a} + \frac{Be^{i\theta_b}}{\Delta_{10} + i\Gamma}\right\} \quad (7.8)$$

The signal detected is the time integral of the square of the sum frequency polarization magnitude so we have

$$S = \left|Ae^{i\theta} + \frac{B}{\Delta_{10} + i\Gamma}\right|^2 \int_{-\infty}^{\infty} dt I_v(t)I_{ir}(t). \quad (7.9)$$

Where we have defined the relative phase between the nonresonant and resonant terms as  $\theta = \theta_a - \theta_b$ .

### 7.2.2 Time Domain

For the time domain data the laser was tuned in resonance with the stretch mode frequency. The integral in the resonance term of Eq. 7.6 can then be expressed in terms of function G where,  $G(t) = \int_{-\infty}^t dt' \mathcal{E}_{ir}(t')e^{-(t-t')/T_2}$ , and the polarization can be written;

$$P_i(t, \tau)e^{-i(\omega_{ir}+\omega_v)t} = \mathcal{E}_v^{(j)}(t - \tau)\left\{Ae^{i\theta_a}\mathcal{E}_{ir}^{(k)}(t) - iBe^{i\theta_b}G(t)\right\} \quad (7.10)$$

The signal observed for a time delay  $\tau$  is the time integral of the square of the sum frequency polarization magnitude,  $S(\tau) = \int_{-\infty}^{\infty} dt |P(t, \tau)|^2$ . For the time domain

measurements the data were fit with an equation of the form:

$$S(\tau) = \int_{-\infty}^{\infty} dt I_{vis}(t - \tau) |Ae^{i\theta} \mathcal{E}_{ir}(t) + BG(t)|^2 \quad (7.11)$$

Notice the deconvolution involves the visible intensity envelope  $I_{vis}(t)$  and the IR field envelope  $\mathcal{E}_{ir}(t)$ . These pulse envelopes were obtained from an autocorrelation of the visible pulse and a cross correlation of the visible and IR pulses.

## 7.3 Results

### 7.3.1 Frequency domain

We will first present the frequency domain results. The SFG signal enhancement with respect to bare copper was measured for exposures of 0.10 and 0.45 L of CO on Cu(111) and is shown in Fig. 3. We fit the observed SFG spectra using Eq. 7.9. In this treatment we assume negligible inhomogeneous broadening.

SFG spectra display interferences in the form of dispersive line shapes that are caused by cross terms between the resonant and nonresonant susceptibilities. This is seen most clearly in our work for the lower exposure spectrum in which the resonant and nonresonant contributions to the signal are comparable. From an analysis that includes interferences it is possible to determine the relative magnitude and phase of the resonant and nonresonant susceptibilities.

Over the range of IR (and sum) frequencies studied (2055-2095  $\text{cm}^{-1}$ ) we assumed that the SFG signal from bare copper is constant, and the SFG spectra observed at

Table 7.1: Parameters derived from a nonlinear least-squares analysis of the surface sum frequency spectra observed for CO on Cu(111). The spectra were fit using the functional form in Eq.7.11 .

	0.1L	0.45 L
A	0.9	0.9
B	0.9	5.6
$2\Gamma(\text{cm}^{-1})$	6.8(1.6)	4.2(0.6)
$\omega_{10}(\text{cm}^{-1})$	2076.4	2073.6
$\theta$	84(20) $^\circ$	107(30) $^\circ$

0.10 and 0.45 L were fit to the form specified in Eq 7.9. The line shapes were deconvoluted from the IR laser (assuming a Gaussian with  $2 \text{ cm}^{-1}$  intensity bandwidth). Parameters obtained from the analysis are presented in Table 7.1 and the best fit line shapes are shown along with the data in Fig. 7.3. The largest SFG enhancement (10X) was observed for the higher dosage spectrum at 0.45 L. This curve will generally be a function of incident and azimuthal angles, but we did not study these variations. The peak signal for the spectra did not vary linearly with coverage in part because the lower coverage band has a broader linewidth thereby reducing the SFG signal. The lower coverage resonance was shifted to higher frequency from 2073.6 to 2076.4  $\text{cm}^{-1}$  and was broadened from 4.2 to 6.8  $\text{cm}^{-1}$ . The bandcenters and linewidths determined in this work are consistent with those measured by the linear FTIR method.

This study differs from the FTIR work because we have obtained information about the relative magnitude and phase of the system's nonresonant second order susceptibility as a function of coverage. In particular, we observed that the off-

resonance SFG intensities were within 10% of the bare Cu value, and we found a relatively small variation in the magnitude and phase of the nonresonant susceptibility at coverages of 0.10 and 0.45 L. These observations suggest a simple model for the influence of adsorbed CO on the nonlinear response of the system. The nonresonant response of the system can arise from the surface and surface-adsorbate-states at the vacuum-metal interface or from bulk Cu located within one optical skin depth of the metal surface. We have observed that the total nonresonant contribution is relatively insensitive to the presence of the adsorbate. The simplest explanation of this effect is that the nonresonant SFG signal is produced by the bulk Cu at these coverages. Explanations involving the surface layer must either assume that the adsorbate does not appreciably change the polarizability of the surface response or that there are competing effects with different signs. Although unlikely, the latter possibility could, in principle, be investigated further by studying the azimuthal dependence of the signal. Interestingly, the SHG signals depend strongly on adsorbate coverage. This is probably because the UV photons generated in SHG experiments are energetically closer to electronic states of the surface[9, 71] or the surface-adsorbate complex than are the upconverted photons in the SFG measurements.

### 7.3.2 Time Domain

We now turn our attention to the time domain experiments. The free induction decay of the vibrational coherence for CO on Cu(111) at a coverage of 0.45 L is shown in Fig. 7.2. We have fit the data using Eq. 7.11. The temporal profile of the visible pulse intensity was determined from an autocorrelation to be reasonably approximated by a Gaussian with a full width of 280 fs. A cross correlation between the IR and visible pulses (shown in Fig. 7.2) demonstrated that the full width of the IR pulse was 380 fs. Using these values in the above equation with the field envelopes modeled as Gaussians, we determine the total dephasing time to be  $T_2 = 2.0 \pm 0.3ps$ . The fit curve from this analysis is shown as the solid line in Fig. 7.2. If we use  $\text{sech}^2$  pulse rather than Gaussian we find that  $T_2 = 1.8 \pm 0.3ps$ . A value of  $T_2 = 1.8 \pm 0.3ps$ . A  $T_2 = 2.0 \pm 0.1ps$ . was also obtained by fitting the decay observed between 2 and 3 ps, i.e. after the driving field is absent, to a single exponential. The measured dephasing time is related to the fullwidth at half-maximum by  $\delta\nu = 1/\pi cT_2$ . The measured  $T_2$  corresponds to a linewidth of  $\delta\nu = 5.3 \pm 0.8 \text{ cm}^{-1}$  which is consistent with the value we obtain by our analysis of the frequency domain SFG spectrum as well as with the RAIRS measurements ( $4.5 \text{ cm}^{-1}$ ).

An important result of this study is that the form of the measured FID is fit very well by an exponential decay as measured over more than a decade of signal. Thus we predict that the vibrational line shape is homogeneously broadened. A shallow

temperature dependence of the linewidth is measured over the range 95-116 K for the ordered overlayer using FTIR. If the linewidth is assumed to be composed of a temperature independent population relaxation ( $T_1$ ) and temperature dependent pure dephasing, we calculate from their results that the polarization decay is largely due to population relaxation ( $T_1 = 1.2$  ps), where the fast relaxation rate is probably due to electron-hole pair coupling. Since the linewidth is very close to being homogeneously broadened, a photon echo would provide essentially the same information on the homogeneous dephasing rate as the free induction decay we have observed for this system. Sufficient inhomogeneous broadening to delay the echo might be present at very low temperature if the relaxation were to lengthen significantly on cooling.

#### 7.4 Conclusion

In summary, we have measured the surface SFG spectrum of CO on Cu (111) at 0.1 and 0.45 L. The analysis accounts for observed interferences that permit a determination of the relative magnitude and phase of the second order susceptibility. The bandcenter and linewidth parameters are consistent with those found in previous RAIRS studies. We have also used transient coherent IR spectroscopy to obtain the FID of CO on Cu(111) at 0.45 L. We have analyzed the signal in a manner that incorporates the influence of the pulse envelope to obtain a value of  $T_2 = 2 \pm 0.3$  ps. This is the first coherent transient measured for an adsorbate on a metal surface.

Although the present experiment differs from previous ultrafast measurements of adsorbate relaxation on metals[18, 17], there are important similarities. In each case a very rapid  $T_1$ , process depopulates the  $v = 1$  level and presumably heats the electrons in the metal so that the pure dephasing ( $T_2'$ ) of the CO vibrational transition is slow compared with  $T_1$ , at the temperatures employed in the experiments. This measurement of  $T_1$ , relaxation can only be accomplished with pulses ( $T_p$ ) that are shorter than the total dephasing time [ $T_2 = \frac{2T_1T_2}{(2T_1+T_2)}$ ]. This means that the experiments must be considered in the coherent limit. This is different from many conventional condensed phase dynamics experiments that fall in the range  $T_2 < T_p < T_1$  such that signal decays are naturally governed by the rate equations for the populations of the levels. In the coherent limit the  $T_1$  relaxation can be measured by frequency selection of a spontaneous process. The conventional pump-probe method does not provide a clean measurement of  $T_1$ , in the coherent limit since the transmitted probe pulse energy depends on both  $T_1$ , and  $T_2$  and the material system is expected to oscillate at detuning frequencies. Indeed such effects were observed explicitly in the dephasing experiments of earlier chapters. These effects were also observed in  $T_1$  measurements conducted for CO on Pt[16]. Probing the vibrational coherence by sum frequency generation, as pioneered by Harris and Levinos[] also does not measure  $T_1$ , exclusively. Clearly there is a great need for experiments that probe surface dynamics in the coherent limit. The FID measurements presented here are an important step in

this direction.

## Chapter 8

### Conclusion

In this thesis I have discussed a novel way to measure the coupling rate of low frequency ( $<100\text{ cm}^{-1}$ ) adsorbate vibrations to the substrate electrons and phonons. Low frequency adsorbate-like modes, are often of much interest, particularly because they are the modes which, when sufficiently excited, lead to desorption and diffusion. Recently both helium atom scattering[73] and CW far IR [74] experiments have examined the low frequency vibrational dynamics of CO on Cu. However the CO stretch mode, with  $\hbar\omega \sim 2000\text{ cm}^{-1}$ , is the only CO complex vibration to be directly monitored by ultrafast IR spectroscopy thus far. The experimental method described, exploits the frequency shift of the stretch vibration induced by the frustrated translation mode. By monitoring the temperature of the frustrated translation, via the stretch frequency shift, ultrafast measurements of the relaxation of a sub-100  $\text{cm}^{-1}$  vibration were obtained.

The dynamical charge transfer model for energy exchange between adsorbate

vibrations and substrate electrons involves a coupling rate which is strongly temperature-dependent in two temperature regimes relevant to current femtosecond photoprocess studies. For low frequency adsorbate modes even liquid nitrogen temperatures are sufficient to cause temperature-dependent rates. Electron-hole pair relaxation of adsorbate vibrations can only be considered temperature independent for modes with frequencies,  $\hbar\Omega$ , much larger than the thermal temperatures present in the system. For femtosecond photoprocess, the electron temperatures are often several thousand degrees. This is high by comparison with the energies of most adsorbate vibrations and thus the temperature dependence of coupling rates will need to be accounted for in models of most femtosecond surface photochemistry.

Applications of the techniques discussed may have some utility in studies of other processes which shift adsorbate frequencies. A variety of surface properties are known to shift the vibrational frequency of an adsorbate, including; adsorbate coverage, the presence of coadsorbed species, binding sites and surface reconstructions to cite a few examples. Combining the novel environment created by femtosecond visible excitation of surfaces with the detailed mode specific descriptions of IR spectroscopy, much can be learned about ultrafast surface photoprocesses.

## Chapter 9

### Appendices

#### 9.1 IR Reflection Absorption Spectroscopy

##### 9.1.1 CW Basics

The adsorbate/metal system is often modeled as three adjoined layers. Reflection spectroscopy in this case has been treated by several authors [75, 76, 77]. Here we will summarize the development in Ref. [77]. As depicted in Fig. 9.1, we consider the adsorbate layer with dielectric constant  $\epsilon_3$ , to be sandwiched between two sem infinite layers: vacuum with dielectric constant  $\epsilon_1$ , and metal with dielectric constant  $\epsilon_2$ . We are interested in the reflectivity change of the p-polarized component of the incident IR beam. The effect of the adsorbate layer is considered weak and is treated as a perturbation.

Generally an incident field of the form,

$$E_o(t) = \mathcal{E}_o e^{i(\vec{k}_1 \cdot \vec{r} + \omega t)} \quad (9.1)$$

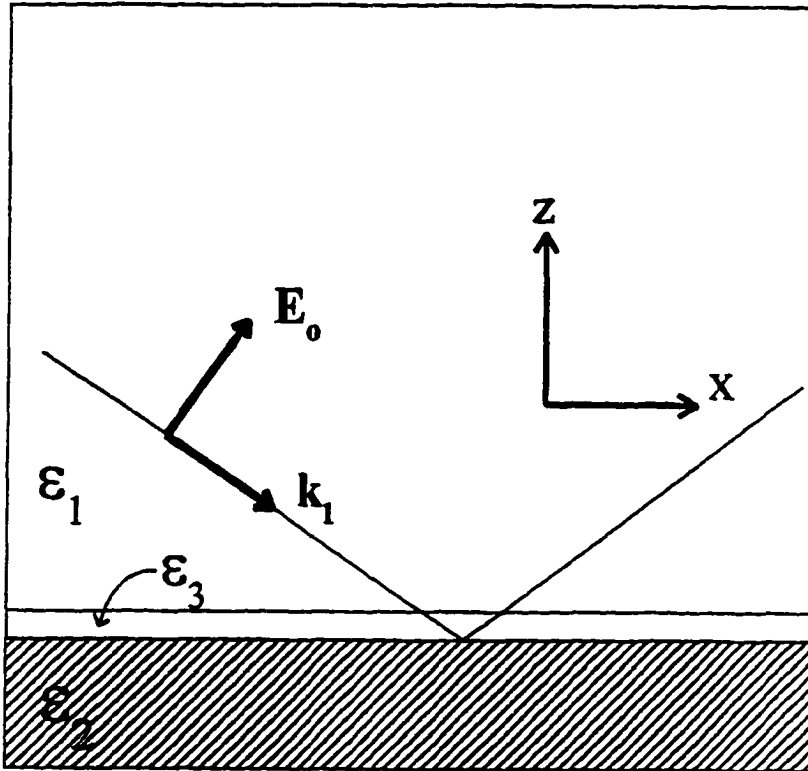


Figure 9.1: Reflection of the incident IR field  $E_o(t) = \mathcal{E}_o e^{i(\vec{k} \cdot \vec{r} + \omega t)}$  from the adlayer and metal substrate is treated with a three layer model. The adsorbate with dielectric constant  $\epsilon_3$  is sandwiched between the vacuum with dielectric constant  $\epsilon_1$  and the metal with dielectric constant  $\epsilon_2$ . The field in the monolayer is determined by  $E_o(t)$  and the substrate reflectivity. The total reflected field is the sum of  $r_p E_o t$  and the specular field reradiated by the induced adlayer polarization.

with wave vector  $\vec{k}_1$  and carrier frequency  $\omega$ , impinges on the sample. The basic plan is to compute the electric field above the surface, the adsorbate polarization in the monolayer, and then the field radiated by this polarization. The field *in the monolayer* is approximately the sum of the incident and reflected fields just above the metal surface. This driving field will depend on the incident angle of the IR beam, and the p-polarized complex reflection amplitude,  $r_p$  (i.e. Fresnel amplitude). For the particular case of non-interacting CO on Cu(111), the z-component of monolayer polarization perpendicular to the surface is of the form[76],

$$P_z = \chi_{\perp} E_o (r_p + 1) (k_{1x}/k_1), \quad (9.2)$$

where  $\chi_{\perp}$  is the CO adlayer susceptibility,  $r_p$  is the p-polarized reflectivity of the metal in the absence of the adlayer, and  $k_{1i}$  is the  $i^{\text{th}}$  component of  $\vec{k}_1$ . The reradiated field in the specular direction due to a thin sheet of polarization  $P_z$  [76] is,

$$E_{ads} = \left( \frac{i4\pi k_1}{\varepsilon_2 k_{1z} + \varepsilon_1 k_{2z}} \right) \left[ \frac{\varepsilon_2}{\varepsilon_3} k_{1x} P_z \right]. \quad (9.3)$$

The *total* reflected field is simply the sum of the reflected field in the absence of the monolayer, i.e.  $E_p = r_p E_o$ , plus the adsorbate field  $E_{ads}$ . In the small signal limit, the differential p-polarized reflectivity is,

$$\frac{\Delta R}{R} \cong -2\text{Im}(G\chi_{\perp}), \quad (9.4)$$

where

$$G = \frac{8\pi k_{1z} k_{1x}^2}{k_{1z}^2 - (k_1/k_2)^4 k_{2z}^2}. \quad (9.5)$$

The angular dependence of the signal is determined by  $G$  (Fig. 9.2). To a first approximation  $G$  can be considered completely real and  $\Delta R/R$  is linearly proportional to the imaginary component of the adsorbate susceptibility. However for high incident angles (i.e.  $89^\circ$  for Cu)  $G$  can be 10 % imaginary (Fig. 9.2b) and therefore  $\Delta R/R$  is a mixture of the real and imaginary components of the adsorbate susceptibility. In our experiments with  $\theta_{incident} \leq 85^\circ$ ,  $G$  is  $\geq 97$  % real.

In pump-probe experiments, particularly at high fluence, one must be careful to include all potential changes in  $G$  induced by the pump pulse. These include rapid changes in dielectric constants due to their temperature dependence.

### 9.1.2 Static and Time Variant Substrate Reflectivity

The time-resolved results of the chapter 4 can be incorporated into the description of reflection absorption spectroscopy from the previous section. For the gated CW probe method, we first consider the case of static substrate optical properties. Introducing a time dependent adsorbate susceptibility  $\chi(t)$  the total field can be written,

$$E_{tot} = r_p E_0 [1 + iG\chi(t)] \quad . \quad (9.6)$$

Here the parameter  $G$  accounts for the adsorbate geometry and is defined by equation (9.5). The time dependent susceptibility  $\chi(t)$  is obtained by dividing the adsorbate polarization  $P(t)$ , by the driving field and can be expressed in a form similar to Eq.

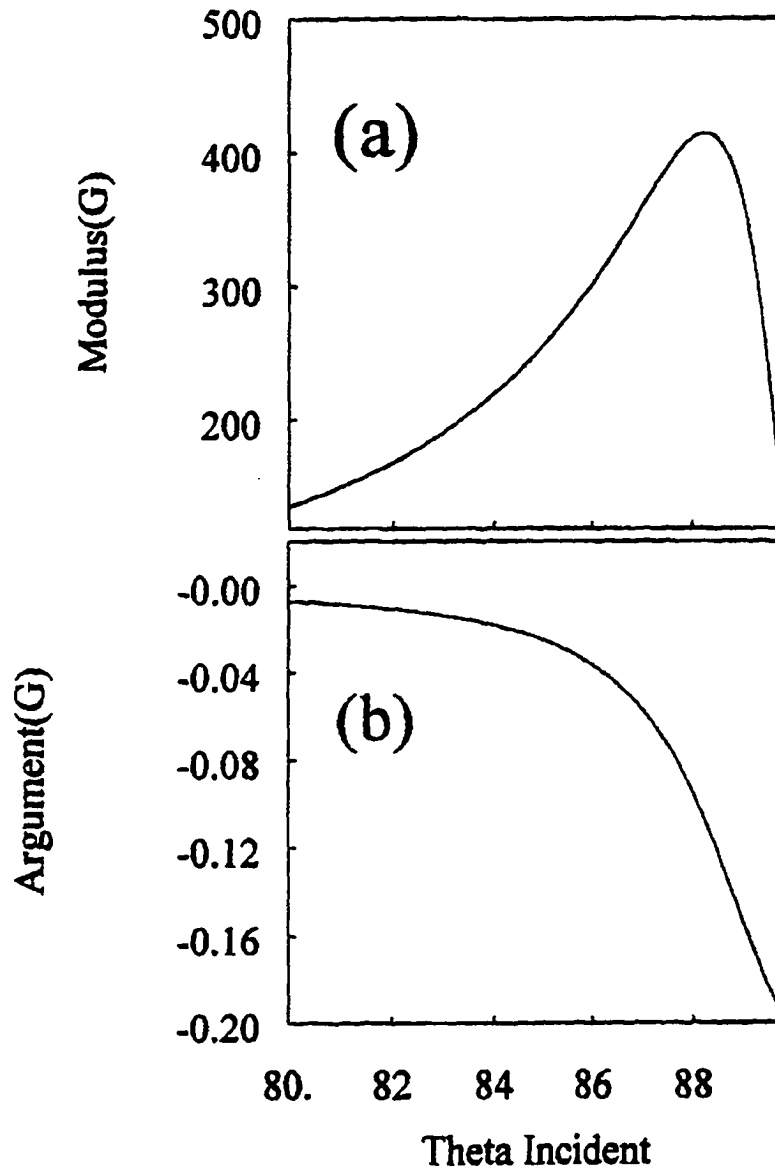


Figure 9.2: The function  $G$  determines the  $\Theta_{incident}$  dependence of  $\Delta R/R$ , the adlayer absorption signal. Using optical coefficients of Cu the modulus (a) and argument (b) of  $G = |G|e^{i\theta}$  were calculated.

(12),

$$\chi(t) = i \frac{\mu_{01}^2 n_0(t)}{\hbar} \int_{-\infty}^t dt_1 e^{-\int_{t_1}^t \Omega_{01}(\tau) d\tau} . \quad (9.7)$$

In the pump/unpump scheme, the differential reflectivity will be,

$$\left(\frac{\Delta R}{R}\right)_{pump} - \left(\frac{\Delta R}{R}\right)_{unpump} = 2\mathcal{I}m\{G(\chi(t) - \chi_0)\} . \quad (9.8)$$

Note that when G has a significant imaginary component the signal will be proportional to a mixture of the imaginary *and real* components of  $\chi(t)$ .

When heated by a visible pulse the dielectric constant of the underlying metal will change. For example, a change of temperature from 72°K to 275° K produces a 3% change in reflectivity at  $\Theta_{incident} = 72^\circ$ . Ultimately a complete description of the total reflected field  $E_{tot}(t) = E_p(t) + E_{ads}(t)$  must account for the time variance of *both* the substrate optical properties and the adsorbate layer polarization. We will estimate the effect of changes in substrate reflectivity below. Following the development of section IIb we assume a small time-dependent component to the reflectivity amplitude,

$$r_p(t) = r_p[1 + \zeta(t)] \quad (9.9)$$

Using the wave vectors  $\vec{k}_1$  and  $\vec{k}_2$  for the field in vacuum and in metal respectively, the time dependence of the substrate optical response can be described in terms of a fractional change  $\frac{\delta k_2(t)}{k_2}$  in complex  $k_2$ , i.e.

$$\zeta(t) = \left[ \frac{k_2}{r_p} \frac{\partial r_p}{\partial k_2} \right] \frac{\delta k_2(t)}{k_2} = \left[ \frac{2k_2^2 k_1^2 k_{1z} (2k_{2z}^2 - k_2^2)}{k_{2z} (k_2^4 k_{1z}^2 - k_1^4 k_{2z}^2)} \right] \frac{\delta k_2(t)}{k_2} . \quad (9.10)$$

The adlayer polarization  $P_z = NTr\{\mu\rho\}$ , can be calculated as in section IIc, with the time evolution of  $\rho$  obtained from the integrated Liouville equation (4.5), with the driving field,

$$E_z(t) = E_0(t)\{1 + r_p[1 + \zeta(t)]\} \frac{k_{1z}}{k_1}. \quad (9.11)$$

Two different aspects of the reflection geometry which are combined in the function  $G$  have different time dependences. One factor which relates the incident field,  $E_0$ , to the driving field,  $E_z$ , must be convoluted with the adsorbate response. The other factor which relates the adsorbate polarization to the specularly reradiated field is considered to have an instantaneous effect on the reradiated field. These two factors must therefore be treated separately in considering a time dependent substrate optical response. We introduce the function  $H(t)$  to relate the adsorbate polarization to the specularly reradiated field.  $E_{tot}$  can be written,

$$E_{tot}(t) = r_p[1 + \zeta(t)][E_0 + iH(t)P_z(t)] \quad (9.12)$$

where

$$H(t) = [1 + \eta(t)] \left\{ \frac{4\pi k_1 k_{1x} k_2^2}{k_2^2 k_{1z} - k_1^2 k_{2z}} \right\}, \quad (9.13)$$

and

$$\eta(t) = \left[ \frac{k_1^2 (k_2^2 - 2k_{2z}^2)}{k_{2z} (k_2^2 k_{1z} - k_1^2 k_{2z})} \right] \frac{\delta k_2(t)}{k_2}. \quad (9.14)$$

In equation (9.13) we have accounted for the change in dielectric constants of the metal through  $\eta(t)$ , which is the same order of magnitude as  $\zeta(t)$ . From equation

(9.12) one can see that the leading contribution to  $E_{tot}$  due to changes in substrate reflectivity is  $\zeta(t)r_pE_0$ . This term *does not* involve the adsorbate polarization. The terms which modulate the adsorbate polarization are at least an order of magnitude smaller. Keeping only the  $\zeta(t)r_pE_0$  term, the total reflected field can be written.

$$E_{tot} = r_pE_0[1 + \zeta(t) + iG\chi(t)] \quad . \quad (9.15)$$

For a pump/unpump scheme the difference signal will be,

$$\left(\frac{\Delta R}{R}\right)_{pump} - \left(\frac{\Delta R}{R}\right)_{unpump} = 2Re\{\zeta(t) + iG(\chi(t) - \chi_0)\} \quad . \quad (9.16)$$

The magnitude of the effect due to temperature dependent substrate optical properties can be estimated by tuning the probe laser far from the CO stretch resonance. measuring  $\zeta(t)$  directly. In our low fluence experiments ( $F_{abs} = 0.09mJ/cm^2$ ) we have not observed any changes in reflectivity far off resonance. However in the case of CO on Pt(111) the changes in substrate reflectivity were the same size as the differential signals induced in the adsorbate absorption [14].

## 9.2 Integrating inhomogenous first order differentials equations

In the analysis of the Liouville and Langevin equations one often needs to integrate first order inhomogenous differential equations. To facilitate these studies we integrate the following first order differential equation;

$$\frac{dy(t)}{dt} + a(t)y(t) = b(t) \quad (9.17)$$

The function  $a(t)$  is arbitrary and might represent a time dependent frequency for example. The function  $b(t)$  is also arbitrary and will usually represent a driving field or force term of some kind. The density matrix term will usually be represented by  $y(t)$ .

We start by multiply the differential equation by a function  $u(t)$ .

$$u(t) \frac{dy(t)}{dt} + u(t)a(t)y(t) = u(t)b(t). \quad (9.18)$$

$u(t)$  is defined by requiring the following condition;

$$\frac{d}{dt}[u(t)y(t)] = u(t)b(t), \quad (9.19)$$

and equating the LHS's of Eq.9.18 and Eq. 9.19;

$$\frac{d}{dt}[u(t)y(t)] = u(t) \frac{dy(t)}{dt} + u(t)a(t)y(t) \quad (9.20)$$

$$u(t) \frac{dy(t)}{dt} + y(t) \frac{du(t)}{dt} = u(t) \frac{dy(t)}{dt} + u(t)a(t)y(t) \quad (9.21)$$

$$y(t) \frac{du(t)}{dt} = u(t)a(t)y(t) \quad (9.22)$$

$$\frac{du(t)}{dt} = u(t)a(t) \quad (9.23)$$

$$(9.24)$$

Integrating this last relation yields an explicit form for  $u(t)$ ;

$$\frac{u(t)}{u(t_0)} = e^{\int_{t_0}^t a(\tau) d\tau}. \quad (9.25)$$

Now that  $u(t)$  is known we can obtain  $y(t)$  by integrating equation 9.18;

$$u(t)y(t) - u(t_0)y(t_0) = \int_{t_0}^t u(t')b(t') dt' \quad (9.26)$$

$$y(t) - \frac{u(t_0)}{u(t)}y(t_0) = \int_{t_0}^t \frac{u(t')}{u(t)}b(t')dt' \quad (9.27)$$

And finally by substituting the expression for  $u(t)$  into the last equation we have the general solution for  $y(t)$ ;

$$y(t) = y(t_0)e^{-\int_{t_0}^t a(\tau)d\tau} + \int_{t_0}^t dt'b(t')e^{-\int_{t'}^t a(\tau)d\tau} \quad (9.28)$$

If we have  $t_0 \rightarrow -\infty$  and  $Re\{a(t)\} > 0$  then the initial condition term decays to zero and we are left with

$$\lim_{t_0 \rightarrow -\infty} y(t) = \int_{-\infty}^t dt'b(t')e^{-\int_{t'}^t a(\tau)d\tau}. \quad (9.29)$$

### 9.3 Substrate temperatures: c program

```

/* Te and Tl calculation assuming thermal conductivity is Te
Tl dependent */

#include <stdio.h>
#include <stdlib.h>
#include <math.h>

#include "nrutil.h"
/* #include "nr.h" */

#define C1 0.9394373 /* 2*sqrt(ln(2)/3.14159) */
#define C2 2.7725887 /* 4*ln(2) */

#define JMAX 4000

#define E 2984.172662F /* 10.0 cm-1 /0.695, 1K =0.695 cm-1 */
#define NO 1.0F
/***** step size *****/
****/

static int numt; /* numt-timesteps in Te cal. */
static int outstep; /* numt/outstep= # of steps output*/
static int discs; /* number of
discs used (for avg. fluence) */
static float t_min, t_max, x_max = 0.0004;
static float dx, dt;

/***** parameters for Gaussian pump pulse *****/
*****/
static float Fab0; /* absorbed fluence at
center of vis*/
static float Fabs[10]; /* absorbed fluences */
static float Skind; /* skin depth */
static float Tp; /* pulse duration FWHM */

/***** physical constants *****/
*****/

static float G; /* electron-lattice coupling */
static float K; /* thermal conductivity */

```

```

static float Cl;    /* lattice heat capacity */
static float Ce0;  /* electron heat capacity */
static float GAMMA = 0.2;
/***** initial conditions *****/
*****/

static float Te0 = 95.0;
/***** Functions in tetl main loop *****/
*****/

static float Tl, Te;
static void lattice();
static void tridagmd ();
static void abcv  ();

/*****/

void main()
{
    int i, j, n;
    float rr[JMAX], aa[JMAX], bb[JMAX], cc[JMAX] ;
    float y, t, P, Pmax, Te[JMAX], Tl[JMAX];
    FILE *fp, *fdat;

    fdat = fopen("pulse.par","r");
    fscanf(fdat,"%f %f %f",&Fabs[1],&Fabs[2],&Fabs[3]);
    fscanf(fdat,"%f %f\n",&Fabs[4],&Fabs[5]);
    fscanf(fdat,"%f\n", &Fab0);
    fscanf(fdat,"%f\n", &Skind);
    fscanf(fdat,"%f\n", &Tp);
    fclose(fdat);

    Fabs[1]*=Fab0;
    Fabs[2]*=Fab0;
    Fabs[3]*=Fab0;
    Fabs[4]*=Fab0;
    Fabs[5]*=Fab0;

```

```

fdat = fopen("phys.par","r");
fscanf(fdat,"%f\n", &G);
fscanf(fdat,"%f\n", &K);
fscanf(fdat,"%f\n", &Cl);
fscanf(fdat,"%f\n", &Ce0);
fclose(fdat);

fdat = fopen("timescan.par","r");
fscanf(fdat,"%f\n", &t_min);
fscanf(fdat,"%f\n", &t_max);
fscanf(fdat,"%f\n", &y);
fscanf(fdat,"%i\n", &numt);
fscanf(fdat,"%i\n", &outstep);
fscanf(fdat,"%i\n", &discs);
fclose(fdat);

dx = x_max /(float) JMAX; /* step size for x */
dt = ( t_max - t_min ) / (float)( numt );/* step size for time */

fp = fopen( "tet15.dat", "w" );

for( n=1 ; n<=discs ; n++ ){
    Pmax = C1*Fabs[n]/( Skind*Tp );

    for( i = 0; i < JMAX; i++ ){ Te[i] = Te0; Tl[i] = Te0; }
    for( i = 0; i < numt; i++ ){

        t = t_min + i * dt;

        P=Pmax * exp(-C2*t*t/Tp/Tp);

        abcv( aa, bb, cc, rr, Te, Tl,P );
        tridag( aa, bb, cc, rr, Te, JMAX );
        lattice( Tl, Te );
        if (i% outstep == 0)
            fprintf( fp, "%6.2f", t );
        if (i% outstep == 0)

```

```

        for( j = 0; j < 1; j++ )
        {
            fprintf( fp, "%9.2f %9.2f \n ", Te[j], Tl[j]);
        }
    }
}
fclose( fp );
}

/***** a[] b[] c[] r[] vectors for tridag*****/

static void abcv(a, b, c, r, Te, Tl, P)
float a[], b[], c[], r[], Te[], Tl[], P;
{

    float A = K * dt / (2.0 * Ce0 * dx * dx );
    float B = G * dt / Ce0;
    float C = dt / Ce0;
    int i;
    float Ktb0, Ktc0, Ktam, Ktbm;
    float Kt[JMAX], Kta[JMAX], Ktb[JMAX], Ktc[JMAX];
    float x, t;

    for( i = 0; i < JMAX; i++ ){
        Kt[i] = A*Te[i]/(Tl[i] +0.0000137*Te[i]*Te[i]);

    }

    for(i =1; i <JMAX-1; i++){
        Kta[i]= 0.5*(Kt[i] +Kt[i-1]);
        Ktb[i]= 0.5*(Kt[i+1] +2.0*Kt[i] +Kt[i-1]);
        Ktc[i]= 0.5*(Kt[i+1]+Kt[i]);

        x = i*dx;
        a[i] = -Kta[i];
        b[i] = Ktb[i] +Te[i] +0.5*B;
        c[i] = -Ktc[i];
        r[i] = Kta[i]*Te[i-1];
        r[i] +=(Te[i]- Ktb[i]- 0.5*B)*Te[i];
        r[i] +=Ktc[i]*Te[i+1];
    }
}

```

```

    r[i] +=B*Tl[i];
    r[i] +=C*P*exp(-x/Skind);

};

/*-----boundary conditions -----*/

    Ktb0 = 0.5*(Kt[1]+Kt[0]);
    Ktc0 = 0.5*(Kt[1]+Kt[0]);
    a[0] = 0.0;
    b[0] = Ktb0 +Te[0] +0.5*B;
    c[0] = -Kt[0];

    r[0] = (Te[0] -Ktb0- 0.5*B)*Te[0];
    r[0] += Ktc0*Te[1];
    r[0] += B*Tl[0];
    r[0] += C*P;

    Ktbm = 0.5*(Kt[JMAX-2]+Kt[JMAX-1]);
    Ktam = 0.5*(Kt[JMAX-1]+Kt[JMAX-2]);
    a[JMAX-1] = -Kt[0];
    b[JMAX-1] = Ktbm +Te[JMAX-1] +0.5*B;
    c[JMAX-1] = 0.0;

    r[JMAX-1] = Ktam*Te[JMAX-2];
    r[JMAX-1] += (Te[JMAX-1] -Ktbm- 0.5*B)*Te[JMAX-1];
    r[JMAX-1] += B*Tl[JMAX-1];
    r[JMAX-1] += C*P*exp(-(JMAX-1)*dx/Skind);
};

/***** lattice.c *****/

static void lattice(Tl,Te)
float Tl[], Te[];
{
    float D = G * dt / Cl/2.0;
    int i;

```

```
for( i=0; i<=JMAX-1; i++) {  
    Tl[i] =(1.0-D)/(1.0+D)*Tl[i] +2.0*D/(1.0+D)*Te[i];  
}  
}
```

#### 9.4 Fitting routine: c program

```

/* integrates the liouville equation for a time dependent
complex frequency */
/* first it calculates w(t) and g(t) from n_ft(t)      */
/* which is read in from tads5.dat                    */

#include <stdio.h>
#include <stdlib.h>
#include <math.h>
#include <string.h>

#include "nrutil.h"

#define PMAX 6
#define DMAX 100
#define IMAX 1000
#define DISCMAX 10
#define FREQMAX 10
#define SETMAX 10
#define Pi 3.141592653
#define C2 2.7725887 /* 4*ln(2) */
#define Te0 95.0
#define BM -0.00007
#define Tpro 20

/*****Step sizes*****/
int numt; /* numt-timesteps in Te cal. */
int outstep; /* inum=numt/outstep= # of steps output */
int inum;
int num0; /* the index corresponding to t=0 for tft,w,g,etc */
int numll;
int discs; /* number of discs used (for avg. fluence) */
int datanum;
int setnum;
int lolim,uplim;
float t_min, t_max,dt,t_ll,Tp;
float gaunorm,lornorm;
float oldchi=1000.0;

```

```

/*****parameters for CO absorption *****/
float dlmax; /*constraints on delta temp factor */
float alpha;
float w0; /*frequency at 95 K */
float dw; /* temperature dependence of      freq  cm-1/K */
float g0; /* HWHM at 0 K */
float dg; /* temperature^2 dependence of width cm-1/K^2 */
float hom, A1;

/*****file names*****/
char *dataname[]={"f80","f8n4"};

/***** input data and calculated temperatures *****/
int  match_data[DMAX];
float stordata[2][DMAX*SETMAX];
float data[2][DMAX];
float conv[DMAX];
float Tl[DISCMAX][IMAX],tal;
float Te[DISCMAX][IMAX],tae;

/***** Functions in tetl main loop *****/

void  sorter();
void  var();
void  globpar();
void  fit();
float chi();
void  mode();
void  adsorbate();
void  freqevol();
void  infreq();
float inlio();
void  match_times();
float setunpump();
void  settq();

```

```

void main(){
globpar(); /* generate a list of global parameters */
fit(); /* calculte fit and chi^2 for ^^^^^^^^^ */
sorter(); /* sort results from smallest chi^2 to highest */
var(); /* check the variance for f,wl,ge,gl using sorted */
}

void fit()
{
    int dwn,dtn;
    int i,j,k,l,m,n,reuse,try1;
    char test[50];
    float t,x,y,Tn,wl;
    float siglat;
    float unpump;
    float rw[SETMAX],rt[SETMAX];
    float par[PMAX],op[PMAX];
    float dwm,dws,dtm,dts;
    float bestx,bestdf,bestdw,bestdt;

    FILE *fsig, *fdat,*fout;

    /**Details of numerically integrating the temperatures Te,Tl,Tq**/

    fdat = fopen("timescan.par","r");
    fscanf(fdat,"%f %f %f %i %i %i",
    &t_min,&t_max,&t_ll,&numt,&outstep,&discs);
    fclose(fdat);

    /**fitting parameters and co absorption parameters */
    hom=0.0;
    Al=0.0;

    fdat = fopen("globgen.par","r");
    fscanf(fdat,"%i %f %i %i\n",&try1,&dlmax,&datanum,&setnum);
    fscanf(fdat,"%f %f %i\n",&x,&x,&i);
    fscanf(fdat,"%f %f %i\n",&dwm,&dws,&dwn);

```

```

fscanf(fdat,"%f %f %i\n",&dtm,&dts,&dtm);
fscanf(fdat,"%f %f %f %f %f",&alpha,&w0,&dw,&g0,&dg);
fscanf(fdat,"%f %f",&hom,&A1);
fclose(fdat);

/*Pulse Duration of the Gate pulse used to convolute the IR response*/

fdat = fopen("pulse.par","r");
fscanf(fdat,"%f %f %f %f %f",&x,&x,&x,&x,&x);
fscanf(fdat,"%f %f %f\n", &x, &x, &Tp);
fclose(fdat);

/**Details of numerically integrating the temperatures Te,Tl,Tq*/

dt = ( t_max - t_min ) / (float)( numt/outstep );
/* step size for time */
inum=numt/outstep;
num0= (int) (0-t_min/dt);
numll= (int) ((t_ll-t_min)/dt);
uplim=5;
lolim=-5;
gaunorm=0.0;
lornorm=setunpump(w0);

for(n=lolim ; n<=uplim ; n++){
t=dt*(float) n;
gaunorm+= exp(-C2*t*t/(Tp*Tp));
}

/*****read in Te, Tlat and data*****/

fdat = fopen("tetl5.dat","r");
/* t1.dat is calculated by xcu5.exe */
for(n=0 ; n<discs ; n++){
for( i = 0 ; i < inum ; i++ ){

```

```

        fscanf(fdat,"%f %f %f\n", &y, &Te[n][i], &Tl[n][i]);
    }
}
fclose( fdat);

    fdat = fopen("tet1-avg.dat","w");
    for(i= 0 ; i < inum ; i++ ){
t=t_min+dt*i;
tae=0;
tal=0;
for(n=0 ; n<discs ; n++){
tae+=Te[n][i];
tal+=Tl[n][i];
}
fprintf(fdat,"%10.5f %10.5f %10.5f\n",t,tae/discs,tal/discs);
}
    fclose(fdat);

    sprintf(test,"%s.dat",dataname[1]);

    printf("%s\n",test);

    for(l=0 ; l< setnum ; l++){

sprintf(test,"/usr/user2/culver/code/data/%s.dat",dataname[1]);
printf("%s\n",test);
    fdat= fopen(test,"r");
    for(i=0 ; i<datanum ; i++){
fscanf(fdat,"%f", &stordata[0][i+datanum*1]);
fscanf(fdat,"%f\n",&stordata[1][i+datanum*1]);
    }
    fclose(fdat);

sprintf(test,"%s.par",dataname[1]);
    printf("%s\n",test);
    fdat= fopen(test,"r");
    fscanf(fdat,"%f %f\n", &rw[1], &rt[1]);
    fclose(fdat);
}

```

```

fdat=fopen("fitpar.par","r");
fsig=fopen("chimesh.dat","w");

while(fscanf(fdat,"%f %f %f %f\n",&par[0],&par[1],&par[2],&wl)!=EOF){
    fprintf(fsig,"%10.5f %10.5f %10.5f", par[0], par[1], par[2]);
    fprintf(fsig,"%15.5f %10.5f ",wl,0.0);

    for(l=0 ;l < setnum; l++){          /* step through each data set*/

for(i=0; i < datanum ; i++){ /* put stored data into data*/
data[0][i]=stordata[0][i+(1*datanum)];
data[1][i]=stordata[1][i+(1*datanum)];
}
bestx=1000;
bestdf=0;
bestdw=0;
bestdt=0;

for(m=0 ; m < dwn ; m++){ /*step through w */
for(n=0 ; n<dtm ; n++){ /*step through t */
par[3]=wl+rw[l]+dwm+dws*m;
par[4]=rt[l]+dtm+dts*n;
x=chi(par); /*get chi for par[] */
if ( x < bestx ){ /*save best values */
sprintf(test,"%s.conv.dat",dataname[l]);
fout=fopen(test,"w");
for(k=0;k<datanum;k++){
fprintf(fout,"%10.5f",data[0][k]);
fprintf(fout,"%10.5f",data[1][k]);
fprintf(fout,"%10.5f\n",conv[k]);
}
fclose(fout);

bestx=x;
bestdf=par[2];
bestdw=par[3];
bestdt=par[4];
}
}
}

```

```

}
/*print best value for set*/
    fprintf(fsig,"%10.5f %15.5f %10.5f", bestx , bestdw, bestdt);
}
    fprintf(fsig,"\n"); /*next line next global par */
}
fclose(fdat);
fclose(fsig);
}

/*****chi.c*****/
/*
*/
/*****/

float chi(par)
    float par[PMAX];
{ int n, m, i,j;
    float xd,x2;
    float gt,t,ta,x,rte0,rtl,fglo,w_L,t_0;
    float chisq,unpump,lamb;
static float Tq[DISCMAX][IMAX],sigdisc[DISCMAX][DMAX];
float Ti[DISCMAX][IMAX];
float sigtot[DMAX];
    float detune[IMAX], width[IMAX];
    float indet[IMAX], inwid[IMAX];

FILE *fsig, *fdat;

        rte0=par[0];
        rtl=par[1];
fglo=par[2];
        w_L=par[3];
t_0=par[4];

lamb=fglo;
match_times(t_0); /* counter values for each data point */
unpump=setunpump(w_L);

```

```

mode(Ti);
adsorbate(rte0,rtl,Tq,Ti);
for(j=0 ; j <3 ; j++){
for(n=0 ; n<discs ; n++){
fregevol(n,w_L,lamb,Tq,detune,width);
infreq(detune,width,indet,inwid);
for( i=0 ; i<datanum ; i++ ){
m=match_data[i]-num0;
sigdisc[n][i]=(inlio(m,indet,inwid)-unpump);
sigdisc[n][i]/=lornorm;
}
}

```

```

for(i=0 ; i< datanum ; i++){
sigtot[i]=0;
for(n=0 ; n < discs ; n++){
m=match_data[i];
sigtot[i]+=BM*(Tl[n][m]-Te0)/discs;
sigtot[i]+=alpha*sigdisc[n][i]/discs;
}
}

```

```

/***** convolution

```

```

*****/

```

```

gt=data[0][1]-data[0][0];
for(i=0 ; i< datanum ; i++){
conv[i]=0;
gaunorm=0;
for(n=lolim; n<=uplim ; n++){
t=(float) (n*gt);
if( (n+i) > 0 & (n+i)<datanum){
gaunorm+=exp(-C2*t*t/(Tp*Tp));
x=sigtot[n+i];
x*=exp(-C2*t*t/(Tp*Tp));
conv[i]+=x;
}
}
conv[i]/=gaunorm;
}

```

```

/*****calculate chisquared*****/
    chisq=0;xd=0;x2=0;
    for(i=0 ; i<datanum ; i++){
xd+=data[1][i]*conv[i];
x2+=conv[i]*conv[i];
chisq+=(data[1][i]-conv[i])*(data[1][i]-conv[i]);
    }
lamb*=xd/x2;
if(lamb<fglo*dlmax){
lamb=fglo*dlmax;
}
if(lamb>(fglo/dlmax)){
lamb=(fglo/dlmax);
}
    chisq/=(datanum);
chisq/=0.0002*0.0002;
}
fdat = fopen("tft-avg.dat","w");
    for(i= 0 ; i < inum ; i++ ){
t=t_min+dt*i;
ta=0;
for(n=0 ; n<discs ; n++){
ta+=Tq[n][i];
}
fprintf(fdat,"%10.5f %10.5f\n",t,ta/discs);
}
    fclose(fdat);
par[4]=lamb;
return chisq;
}

```

```

/***** adsorbate.c *****/
/***** calculates adsorbate temperature from Te and Tl ****/
/*****
void adsorbate(rte0,rt10,Tq,Ti)
    float rte0,rt10,Tq[][IMAX],Ti[][IMAX];
{ int n,i;

```

```

float rte,rtl;
for(n=0 ; n< discs; n++){
Tq[n][0]=Te[n][0];
for(i=0 ; i< inum-1 ; i++){
rte=rte0*(1/(1-exp(-hom/(0.695*Te[n][i]))));
rtl=rtl0;
  Tq[n][i+1]=Tq[n][i]*(1-(dt/2)*((rte)+(rtl)));
Tq[n][i+1]+=0.5*(dt*rte)*(Te[n][i+1] + Te[n][i]);
  Tq[n][i+1]+=0.5*(dt*rtl)*(Tl[n][i+1] + Tl[n][i]);
  Tq[n][i+1]/=(1+ (dt/2)*((rte)+(rtl)));
  }
}
}

/***** mode.c *****/
/**** calculates the temperature of mode i from Te and Tl ****/
/*****/

void mode(Ti)
  float Ti[][IMAX];
{ int n,i;
float Ti0,nin,nire,nirl,ni,rei,rli;
rei=0.5;
rli=0.001;
Ti0=2986.60;
for(n=0 ; n< discs; n++){
Ti[n][0]=Te[n][0];
ni=(1/(exp(Ti0/Ti[n][0])-1));
for(i=0 ; i< inum-1 ; i++){
ni=(1/(exp(Ti0/Ti[n][i])-1));
nire=(1/(exp(Ti0/Te[n][i])-1));
nirl=(1/(exp(Ti0/Tl[n][i])-1));
  nin=ni*(1-(dt/2)*((rei)+(rli)));
nin+=dt*rei*nire;
  nin+=dt*rli*nirl;
  nin/=(1+ (dt/2)*((rei)+(rli)));
Ti[n][i+1]=Ti0/(log(1.0+(1.0/nin)));
  }
}
}

```

```

/*****freqevol*****/
/* returns the detuning & width as a function of time
   in units of inverse picoseconds*/
/*****/

void freqevol(n,w_L,lamb,Tq,detune,width)
  int n;
  float w_L, detune[], width[],Tq[][IMAX],lamb;
{  int i;
   float Teff;
   for (i=0 ; i<inum ; i++){
Teff=Te0+lamb*(Tq[n][i]-Te0);
detune[i] = 0.06*Pi*(w_L - w0 + dw*(Teff-Te0));
width[i]  = 0.06*Pi*(g0 + dg*Teff*Teff);
   }
}

/*****infreq*****/
/*Integrates Freq from tmin untill time tand stores
the integral in      */
/* indet[] and inwid[]. This facilitates integrating
the Liouville equation */
/*****/

void infreq(detune,width,indet,inwid)
  float detune[], width[], indet[], inwid[];
{  int n;
   indet[0]=0; inwid[0]=0;
   for (n=1 ; n<inum ; n++){
indet[n]=indet[n-1] + 0.5*(detune[n]+detune[n-1])*dt;
inwid[n]=inwid[n-1] + 0.5*(width[n]+width[n-1])*dt;
   }
}

```

```

/*****inlio*****/
/* Integrates the Liouville equation from tmin untill time t **/
/*****/

float inlio(k, d, w)
int k ;
float d[], w[];
{ float x,s,t,C3;
  int n;
  s=0;
  C3=-C2/(Tpro*Tpro);
  for(n=num11; n<=num0; n++){
t=dt*(float)(n-num0);
x=exp(C3*t*t);
x*=exp(-(w[num0+k]-w[n+k]))*cos(-(d[num0+k]-d[n+k]));
s += x;
}
  s*=dt;
  return s;
}

/*****match_times*****/
/**compares the times in the data array with times in
the te,tl arrays and
stores the indices of the te, tl times in an array match_data***/
/*****/

void match_times(t_0)
float t_0;
{ int n,i,found;
float t;
for(n=0 ; n<datanum ; n++){
found=0;
for(i=0; i<inum && !found; i++){
t=t_0 + t_min+dt*(float) (i);
if(-dt/2<(data[0][n]-t) && (data[0][n]-t)<dt/2){
found=1;
match_data[n]=i;
}
}
}

```

```

}
}
}

```

```

/*****setunpump*****/
/* Integrates the Liouville equation from tmin untill time t **/
/*****/

```

```

float setunpump(w_L)
  float w_L;
  {      float x, da[IMAX], wa[IMAX], id[IMAX], iw[IMAX], Tq[DISCMAX][IMAX];
        int hih, m;
  settq(Tq);
  m=0;
  freqevol(m,w_L,1.0,Tq,da,wa);
  infreq(da,wa,id,iw);
        x=inlio(m,id,iw);
  return x;
}

```

```

/*****set_array*****/
/* Integrates the Liouville equation from tmin untill time t **/
/*****/

```

```

void settq(Tq)
  float Tq[][IMAX];
  {      int n,m;
  for(m; m<discs; m++){
  for(n; n<inum; n++){
  Tq[m][n]=Te0;
  }
  }
}

```

```

/*****generate a list of parameters*****/

```

```

void globpar()
{

```

```

int i, j, k, l, m;
int wn,gen,gln,fn,an,tn;
int try;
float x;
float w, ge,gl,f,a,t,dt;
float wm,gem,glm,fm,am,tm;
float ws,ges,gls,fs,as,ts;

FILE *fdat,*fgam;

fdat = fopen("globgen.par","r");
fscanf(fdat,"%i %f %i %i\n",&try,&x,&i,&i);
fscanf(fdat,"%f %f %i\n", &gem, &ges,&gen);
fscanf(fdat,"%f %f %i\n", &glm, &gls,&gln);
fscanf(fdat,"%f %f %i\n", &fm, &fs,&fn);
fscanf(fdat,"%f %f %i\n", &wm, &ws,&wn);

fclose(fdat);

fdat = fopen("fitpar.par","w");

for(j=0;j<wn;j++){
w=wm+j*ws;
for(k=0;k<fn;k++){
f=fm+k*fs;
for(l=0;l<gln;l++){
gl=glm+l*gls;
for(m=0;m<gen;m++){
ge=gem+m*ges;
fprintf( fdat, "%10.5f %10.5f %10.5f %15.5f\n ", ge,gl,f,w);
}
}
}
}
fclose(fdat);
}

```

## Chapter 10

### Bibliography

- [1] Y. J. Chabal, Surf. Sci. Rep. **8**, 211 (1988).
- [2] "Vibrations at Surfaces", J. Electron Spectrosc. and Related Phenom. **54/55** (1990).
- [3] *Laser Spectroscopy and Photochemistry on Metal Surfaces*, edited by W. H. H.-L Dai (World Scientific, Singapore, 1995).
- [4] "Surface Reaction Dynamics", Chem. Phys. **205** (1996).
- [5] R. R. Cavanagh, D. S. King, J. C. Stephenson, and T. F. Heinz, J. Phys. Chem. **97**, 786 (1993).
- [6] J. A. Prybyla, T. F. Heinz, J. A. Misewich, M. M. T. Loy, and J. H. Glowina. Phys. Rev. Lett.
- [7] F. Budde, T. F. Heinz, M. M. T. Loy, J. A. Misewich, F. deRougemont and H. Zacharias, Phys. Rev. Lett. **66** 3024 (1991).

- [8] F. Budde, T. F. Heinz, A. Kalamarides, M. M. T. Loy, and J. A. Misewich, *Surf. Sci.* **283** 143 (1993).
- [9] J. Prybyla, H. Tom, and G. Aumiller, *Phys. Rev. Lett.* **68**, 503 (1992).
- [10] F. J. Kao, D. G. Bush, D. G. Dacosta, and W. Ho, *Phys. Rev. Lett.* **70**, 4098 (1993).
- [11] F. J. Kao, D. G. Bush, D. Cohen, D. G. Dacosta, and W. Ho, *Phys. Rev. Lett.* **71** 2094 (1993).
- [12] J. A. Misewich, A. Kalamarides, T. F. Heinz, U. Hofer and M. M. T. Loy, *J. Chem. Phys.* **100**, 736 (1994).
- [13] J. P. Culver, M. Li, L. G. Jahn, R. M. Hochstrasser, and A. G. Yodh, *Chem. Phys. Lett.* **214** 431 (1993); J. P. Culver, M. Li, L. G. Jahn, R. M. Hochstrasser, and A. G. Yodh, in *Laser Spectroscopy and Photochemistry on Metal Surfaces*, eds. H.-L. Dai and W. Ho, (World Scientific, Singapore, in press).
- [14] T. A. Germer, J. C. Stephenson, E. J. Heilweil, and R. R. Cavanagh, *J. Chem. Phys.* **98**, 9986 (1993).
- [15] T. A. Germer, J. C. Stephenson, E. J. Heilweil, and R. R. Cavanagh, *Phys. Rev. Lett.* **71**, 3327 (1993); T. A. Germer, J. C. Stephenson, E. J. Heilweil, and R. R. Cavanagh, *J. Chem. Phys.* **101**, 1704 (1994).

- [16] J. D. Beckerle, M. P. Casassa, R. R. Cavanaugh, E. J. Heilweil, and J. C. Stephenson, *Phys. Rev. Lett.* **64**, 2090 (1990); J. D. Beckerle, M. P. Casassa, E. J. Heilweil, R. R. Cavanaugh, and J. C. Stephenson, *J. Electron. Spectrosc.* **54/55**, 17 (1990);.
- [17] A. L. Harris, N. J. Levinos, L. Rothberg, L. H. Dubois, L. Dhar, S. F. Shane, and M. J. Morin, *J. Electron. Spectrosc.* **54/55** 5 (1990); A. L. Harris, L. Rothberg, L. Dhar, N. J. Levinos, L. H. Dubois, *J. Chem. Phys.* **94** 2438 (1991); M. Morin, N.J. Levinos, and A. L. Harris, *J. Chem. Phys.* **96** 3950 (1992).
- [18] J. D. Beckerle, R. R. Cavanaugh, M. P. Casassa, E. J. Heilweil, and J.C. Stephenson, *J. Chem. Phys.* **95**, 5403 (1991); R. R. Cavanagh, J. D. Beckerle, M. P. Casassa, E. J. Heilweil, and J. C. Stephenson, *Surf. Sci.* **269/270** 113 (1992).
- [19] P. Guyot-Sionnest, *Phys. Rev. Lett.* **66** 1489 (1991); P. Guyot-Sionnest, *J. of Electron. Spectrosc.* **64/65** 1 (1993).
- [20] A. L. Harris, L. Rothberg, L. H. Dubois, and L. Dhar, *Phys. Rev. Lett.* **64**, 2086 (1990).
- [21] J. P. Culver, M. Li, L. G. Jahn, R. M. Hochstrasser, and A. G. Yodh, *Chem. Phys. Lett.* **214** 431 (1993).
- [22] T. A. Germer, J. C. Stephenson, E. J. Heilweil, and R. R. Cavanagh, *Phys. Rev. Lett.* **71**, 3327 (1993).

- [23] B. N. J. Persson and M. Persson, *Solid State Commun.* **36**, 175 (1980).
- [24] M. Head-Gordon and J. C. Tully, *J. Chem. Phys.* **96**, 3939 (1992).
- [25] P. Guyot-Sionnest, P. Dumas, Y. J. Chabal, and G. S. Higashi, *Phys. Rev. Lett.* **64**, 2156 (1990).
- [26] J. C. Tully, M. Gomez, and M. Head-Gordon, *J. Vac. Sci. Technol.* **A11**, 1914 (1993).
- [27] S. Lewis, A. Rappe, to be published.
- [28] P. Hamm, M Zurek, W. Mantele, M. Meyer, H. Scheer and W. Zinth, *Proc. Natl. Acad. Sci.* **92** 1826 (1995).
- [29] S. I. Anisimov, B. L. Kapeliovich, and T. L. Perel'man, *Zh. Eksp. Teor. Fiz.* **66**, 776 (1974).
- [30] P. S. Bagus, K. Hermann and C. W. Baushlicher, *J. Chem. Phys.* **81** 1967 (1984); K. Hermann, P S. Bagus and C. J. Nelin, *Phys. Rev. B*, **35** 9467 (1987); P. S. Bagus and G. Pacchioni, *Surf. Sci.* **278** 427 (1992).
- [31] G. Bylholder, *J. Phys. Chem.* **68**, 2772 (1964).
- [32] R. P. Messmer, in *The Nature of the Surface Chemical Bond*, eds. T Rhodin and G. Ertl, pp 51-112, North-Holland.

- [33] T. Hertel, E.Knoesel, E. Hasselbrink, M. Wolf, and G.Ertl, Surf. Sci. Letters **317**, 11147 (1994); E. Knoesel, T. Hertel, M. Wolf and G. Ertl, Chem. Phys. Lett. **240**, 409 (1995).
- [34] B. Gumhalter, K. Wandelt, and P. Avouris, Phys. Rev. B. **37**, 8048 (1988).
- [35] P. Hollins and J. Pritchard, Surf. Sci. **89**, 486 (1979).
- [36] R. Raval *et al.*, Surf. Sci. **230**, 353 (1988).
- [37] C. J. Hirschmugl, G. P. Williams, F. M. Hoffmann, and Y. J. Chabal, Phys. Rev. Lett. **65**, 480 (1990).
- [38] J. Ellis, J. P. Toennies, and G. Witte, J. Chem. Phys. **102**, 5059 (1995).
- [39] B. N. J. Persson and A. Liebsch, Surf. Sci. **110**, 356 (1981).
- [40] M. Brandbyge, P. Hedegard, T. F. Heinz, J. A. Misewich, and D. M. Newns, To be published.
- [41] T. T. Rantala and A. Rosen, Phys. Rev. B. **34**, 837 (1986).
- [42] M. Persson and B. Hellsing, Phys. Rev. Lett. **49**, 662 (1981).
- [43] D. R. Dykaar and S. L. Chuang, J. Opt. Soc. Am. B **11**, 2454 (1994).
- [44] I. Brener *et al.*, J. Opt. Soc. Am. B **11**, 2457 (1994).

- [45] C. B. Harris, R. M. Shelby, and P. A. Cornelius, *Phys. Rev. Lett.* **38** 1415 (1977);  
R. M. Shelby, C. B. Harris, and P. Cornelius, *J. Chem. Phys.* **70** 34 (1974); S.  
Marks, P. A. Cornelius, and C. B. Harris, *J. Chem. Phys.* **73** 3069 (1980).
- [46] N. G. van Kampen, *Stochastic Processes in Physics and Chemistry* (North-  
Holland, New York, 1981).
- [47] B. N. J. Perrson and R. Ryberg, *Phys. Rev. B.* **32**, 3586 (1985).
- [48] B. N. J. Perrson, F. M. Hoffman, and R. Ryberg, *Phys. Rev. B.* **34**, 2266 (1986).
- [49] G. L. Eesley, *Phys. Rev. B.* **33**, 2144 (1986).
- [50] H. E. Elsayed-Ali, T. Norris, M. A. Pessot, and G. Mourou, *Phys. Rev. Lett.* **58**,  
1212 (1987).
- [51] P. B. Corkum, F. Brunel, N. K. Sherman, and T. Srinivasan-Rao, *Phys. Rev.*  
*Lett.* **61**, 2886 (1988).
- [52] R. W. Schoenlein, W. Z. Lin, J. G. Fujimoto, and G. L. Eesley, *Phys. Rev. Lett.*  
**58**, 1680 (1987).
- [53] P. B. Allen, *Phys. Rev. Lett.* **59**, 1460 (1987).
- [54] S. D. Broson *et al.*, *Phys. Rev. Lett.* **64**, 2172 (1990).
- [55] H. E. Elsayed-Ali, T. Juhasz, G. O. Smith, and W. E. Bron, *Phys. Rev. B.* **43**,  
4488 (1991).

- [56] W. W. Fann, R. Storz, H. W. K. Tom, and J. Bokor, *Phys. Rev. Lett.* **68**, 2834 (1992).
- [57] *American Institute of Physics Handbook*, 3rd ed., edited by D. E. Gray (Mcgraw-Hill, New York, 1972).
- [58] W. H. Press, S. A. Teukolsky, W. T. Vetterling, and B. P. Flannery, *Numerical Recipes in C; The Art of Scientific Computing* (Cambridge Univ. Press, New York, 1992).
- [59] J. C. Owrutsky, J. P. Culver, M. Li, Y.R. Kim, M. J. Sarisky, M. S. Yeganeh, A. G. Yodh, and R. M. Hochstrasser, *J. Chem. Phys.* **97** 4421 (1992).
- [60] J. N. Moore, P. A. Hansen, and R. M. Hochstrasser, *Chem. Phys. Lett.* **138**, 110 (1987).
- [61] M. Li, J. C. Owrutsky, M. Sarisky, J. P. Culver, A. Yodh, and R. M. Hochstrasser. *J. Chem. Phys.* **98** 5499 (1993).
- [62] P. A. Anfinrud, C. Han, and R. M. Hocstrasser, *Prc. Natl. Acad. Sci. USA* **86**, 8387 (1989).
- [63] M. D. Dawson, T. F. Bogges, D. W. Garvey, and A. Smith, *Opt. Commun.* **60**, 79 (1986).
- [64] M. Dawson, D. Maxson, T. F. Boggess, and A. L. Smirl, *Opt. Lett.* **13**, 126 (1988).

- [65] A. M. Lahee, J. P. Toennies, and C. Woll, *Surf. Sci.* **177**, 371 (1986).
- [66] E. Schweizer, B. N. J. Persson, M. Tushaus, and A. M. Bradshaw, *Surf. Sci.* **213**, 49 (1989).
- [67] *Handbook of Optical Constants of Solids II*, edited by E. D. Palik (Academic Press, Boston, 1991).
- [68] K. Wynne and R. M. Hochstrasser, *Chem. Phys.* **193**, 211 (1995).
- [69] The following physical constants were used: electron phonon coupling  $G = 0.7 \times 10^{17} \text{ W/m}^3 \text{ K}$ , phonon heat capacity  $C_l = 2.26 \times 10^6 \text{ J/m}^3 \text{ K}$ , electron heat capacity  $C_e = 96.6 T_e \text{ J/m}^3 \text{ K}^2$ , electron diffusion constant  $\kappa = 435 \frac{T_e}{T_l} \text{ W/mK}$ .
- [70] R. W. Hellwarth, *Prog. Quan. Elec.* **5**, 1 (1977).
- [71] J. C. Owrutsky *et al.*, *J. Chem. Phys.* **97**, 4421 (1992).
- [72] (PUBLISHER, ADDRESS, YEAR), p. 1.
- [73] A. Graham, F. Hoffman, and J. P. Toennies, *J. Phys. Chem.* **104**, 5311 (1996).
- [74] C. J. Hirschmugl and G. P. Williams, *Phys. Rev. B.* **52**, 14177 (1995).
- [75] R. G. Greenler, *J. Chem. Phys.* **44**, 310 (1966).
- [76] T. F. Heinz, Ph.D. dissertation, University of California at Berkeley, 1982.
- [77] A. G. Yodh and H. W. K. Tom, *Phys. Rev. B.* **45**, 14302 (1992).